Changes and modifications in the "TrackedChanges"-version are highlighted in yellow, blue, green, and red according to Referee #1, #2, both and our own revisions, respectively.

Chemical composition and source attribution of submicron aerosol particles in the summertime Arctic lower troposphere

Franziska Köllner[1,a], Johannes Schneider[1], Megan D. Willis[2,b], Hannes Schulz[3], Daniel Kunkel[4],
Heiko Bozem[4], Peter Hoor[4], Thomas Klimach[1], Frank Helleis[1], Julia Burkart[2,c], W. Richard Leaitch[5],
Amir A. Aliabadi[5,d], Jonathan P. D. Abbatt[2], Andreas B. Herber[3], and Stephan Borrmann[4,1]

[1]Max Planck Institute for Chemistry, Mainz, Germany
[2]Department of Chemistry, University of Toronto, Canada
[3]Alfred Wegener Institute for Polar and Marine Research, Bremerhaven, Germany
[4]Institute for Atmospheric Physics, Johannes Gutenberg University Mainz, Germany
[5]Environment and Climate Change Canada, Toronto, Canada
[a]now at: Institute for Atmospheric Physics, Johannes Gutenberg University Mainz, Germany
[b]now at: Department of Chemistry, Colorado State University, Fort Collins, CO, USA
[c]now at: Aerosol Physics and Environmental Physics, University of Vienna, Austria
[d]now at: Environmental Engineering Program, University of Guelph, Guelph, Canada
Correspondence: Franziska Köllner (f.koellner@mpic.de)

Abstract. Aerosol particles impact the Arctic climate system, both directly and indirectly by modifying cloud properties, yet our understanding of their vertical distribution, chemical composition, mixing state, and sources in the summertime Arctic is incomplete. In-situ vertical observations of particle properties in the high Arctic, combined with modeling analysis on source attribution are in short supply, particularly during summer. We thus use airborne measurements of aerosol particle composition to demonstrate the strong contrast between particle sources and composition within and above the summertime Arctic boundary layer. In-situ measurements from two complementary aerosol mass spectrometers, the ALABAMA and the HR-ToF-AMS, with black carbon measurements from an SP2 are presented. Particle composition analysis was complemented by trace gas measurements, satellite data, and air mass history modeling to attribute particle properties to particle origin and air mass source regions. Particle composition above the summertime Arctic boundary layer was dominated by chemically aged particles, containing elemental carbon, nitrate, ammonium, sulfate, and organic matter. From our analysis, we conclude that the presence of these particles was driven by transport of aerosol and precursor gases from mid-latitudes to Arctic regions. Particularly, elevated concentrations of nitrate, ammonium, and organic matter coincided with time spent over vegetation fires in northern Canada. In parallel, those particles were largely present in high CO environments ($>90\,\mathrm{ppb_v}$). Additionally, we observed that the organic-to-sulfate ratio was enhanced with increasing influence from these fires. Besides vegetation fires, particle sources in mid-latitudes further include anthropogenic emissions in Europe, North America, and East Asia. The presence of particles in the Arctic lower free troposphere, particularly sulfate, correlated with time spent over populated and industrial areas in these regions. Further, the size distribution of free tropospheric particles containing elemental carbon and nitrate was shifted to larger diameters compared to particles present within the boundary layer. Moreover, our analysis suggests that organic matter, when present in the Arctic free troposphere, can partly be identified as low-molecular weight dicarboxylic

acids (oxalic, malonic, and succinic acid). Particles containing dicarboxylic acids were largely present when the residence time of air masses outside Arctic regions was high. In contrast, particle composition within the marine boundary layer was largely driven by Arctic regional processes. Air mass history modeling demonstrated that alongside primary sea spray particles, marine-biogenic sources contributed to secondary aerosol formation by trimethylamine, methanesulfonic acid, sulfate, and other organic species. Our findings improve our knowledge of mid-latitude and Arctic regional sources that influence the vertical distribution of particle chemical composition and mixing state in the Arctic summer.

Copyright statement. TEXT

1 Introduction

In the face of rapid climate changes in the Arctic (IPCC, 2014, 2018), polar research has intensified to understand the key processes driving these changes and their effects on the Arctic environment (e.g., Serreze and Francis, 2006; Serreze et al., 2009; Flanner et al., 2011; Stroeve et al., 2012; Pithan and Mauritsen, 2014). Observed amplified Arctic warming in recent decades and coupled rapid sea ice retreat are attributed to various causes, including increases in greenhouse gases and local feedback mechanisms, such as the snow/ice-albedo feedback (e.g., Curry et al., 1995; Holland and Bitz, 2003; Serreze and Barry, 2011; Flanner et al., 2011; Stroeve et al., 2012; Pithan and Mauritsen, 2014; Law et al., 2014; Arnold et al., 2016). However, one important aspect concerning the Arctic climate system pertains to the coupling between aerosol, clouds, and radiation. Aerosol particles, as short-lived climate forcers, perturb the Arctic radiative balance by reflecting and absorbing shortwave radiation (aerosol-radiation interaction) and modifying cloud formation and properties (aerosol-cloud interaction). The coupling between aerosol particles, clouds, and radiation strongly depends on particle chemical composition and mixing state (e.g., Haywood and Boucher, 2000; Boucher et al., 2013). Light-absorbing aerosol, such as black carbon (BC) and mineral dust, can impact the regional Arctic climate by a combination of different aerosol-radiation processes. First, light-absorbing particles when deposited on snow and ice can lead to increased sea ice melt by reducing the snow/ice albedo (e.g., Hansen and Nazarenko, 2004; Flanner, 2013; Jiao et al., 2014; Schacht et al., 2019). Second, the presence of aerosol in Arctic tropospheric layers leads to cooling of the surface beneath by absorbing incoming solar radiation and by reflecting radiation back to space. The result is an increase in tropospheric stability (e.g., Flanner, 2013; Schacht et al., 2019). Third, increased radiative forcing by black carbon in mid-latitudes leads to increasing meridional temperature gradient and subsequent increased northward heat transport (e.g., Sand et al., 2013a, b). However, recent studies show that the magnitude of aerosol-radiation interactions of BC is largely dependent on the particle mixing state (Bond et al., 2006; Kodros et al., 2018). In contrast to light-absorbing aerosol, scattering aerosol species, such as sulfate, of both anthropogenic and biogenic origin, exert a net negative shortwave radiative forcing on the Arctic surface (Quinn et al., 2008; Yang et al., 2018). Overall, modeling studies focusing on aerosol-radiation interactions demonstrate that reductions in Arctic anthropogenic aerosol (mainly BC and sulfate) likely contributed to the observed Arctic surface warming in recent decades (e.g., Shindell and Faluvegi, 2009; Najafi et al., 2015; Acosta Navarro

et al., 2016; Breider et al., 2017).

Aerosol particles, serving as nuclei for water condensation or nucleation of the ice phase, are fundamental to cloud formation. The effects of these particles on clouds are important drivers of the Arctic surface energy budget. It is known that the net radiative effect of Arctic low-level clouds varies significantly with season. Arctic low-level clouds warm the Arctic surface through most of the year. However, for a short period in summer when the incoming solar radiation is maximum over regions with a low albedo, clouds exert a negative radiative forcing on the Arctic surface (Intrieri et al., 2002; Shupe and Intrieri, 2004). Particularly, in the summertime pristine Arctic environment with low aerosol concentrations, cloud formation and properties are sensitive to the available cloud nuclei concentration (Mauritsen et al., 2011; Moore et al., 2013; Leaitch et al., 2016). Particle sources, formation, and atmospheric processing control particle composition, mixing state, and size distribution, which in turn significantly impact the ability of particles to act as cloud nuclei (e.g., Junge and McLaren, 1971; Haywood and Boucher, 2000; Dusek et al., 2006; McFiggans et al., 2006; Moore et al., 2011; Martin et al., 2011; Boucher et al., 2013). In the summertime pristine Arctic boundary layer (BL), marine emissions can contribute significantly to low-level cloud nuclei concentrations (Orellana et al., 2011; Leaitch et al., 2013; Willis et al., 2016; Burkart et al., 2017; Dall'Osto et al., 2017; Baccarini et al., 2020), whereas the episodic transport of anthropogenic and biomass burning aerosol from southern latitudes can have a crucial impact on cloud formation and cloud properties (e.g., Moore et al., 2011; Zamora et al., 2016; Coopman et al., 2018; Norgren et al., 2018). Along with long range transport and aerosol aging processes, oxygenation of the organic aerosol enhances aerosol's hygroscopicity and thus the ability of the particles to form cloud droplets (e.g., Furutani et al., 2008; Jimenez et al., 2009; Chang et al., 2010; Moore et al., 2011). Together, it is important to know the particle composition, mixing state, and size distribution as well as related sources and formation processes to accurately predict the impact of aerosol on the Arctic climate system.

In Arctic summer, organic matter significantly contributes to submicron aerosol mass (e.g., Schmale et al., 2011; Chang et al., 2011; Lathem et al., 2013; Breider et al., 2014; Willis et al., 2017; Leaitch et al., 2018; Lange et al., 2018; Tremblay et al., 2019). Organic aerosol encompasses a large variety of chemical compounds that vary significantly across Arctic sites, owing to differences in sources and chemical processing (e.g., Shaw et al., 2010; Fu et al., 2013; Hansen et al., 2014; Leaitch et al., 2018). Boreal fires and to a lesser extent anthropogenic activities in North America and northern Eurasia can strongly influence the organic aerosol burden in the summer Arctic free troposphere (FT) (Hirdman et al., 2010; Schmale et al., 2011; Matsui et al., 2011a; Lathem et al., 2013; Breider et al., 2014). Whereas in the summertime Arctic BL, organic matter can also be influenced by both primary emissions and secondary chemical processes from Arctic marine and terrestrial sources (e.g., Willis et al., 2016, 2017; Köllner et al., 2017; Croft et al., 2019). Sources and identities of secondary organic aerosol (SOA) are poorly characterized (Willis et al., 2018). However, tracers of SOA, including a oxygenated species such as dicarboxylic acids (DCA) (e.g., oxalic, malonic, and succinic acid) have been detected at Arctic sites (e.g., Kawamura et al., 1996; Kerminen et al., 1999; Fu et al., 2009; Kawamura et al., 2012; Fu et al., 2013; Hansen et al., 2014). Several studies demonstrated that particulate DCA are less abundant in summer than in spring, driven by diminished long range transport of precursors and efficient aerosol wet removal. In parallel, natural regional sources of DCA become more important as sea ice melts and biological productivity increases (e.g., Kawamura et al., 1996; Kerminen et al., 1999; Kawamura et al., 2010, 2012). DCA are highly water-soluble,

3

thus, the presence of particulate DCA can result in a more hygroscopic aerosol population, which can affect cloud formation and cloud properties (e.g., Giebl et al., 2002; Ervens et al., 2004; Abbatt et al., 2005; Chang et al., 2007). Besides the importance for aerosol-cloud interactions, little is known on the vertical distribution of DCA in Arctic aerosol and the related sources.

Sulfate concentrations in the summertime Arctic FT are largely influenced by anthropogenic sources in northern Eurasia, North America, and East Asia (Shindell et al., 2008; Hirdman et al., 2010; Kuhn et al., 2010; Bourgeois and Bey, 2011; Schmale et al., 2011; Matsui et al., 2011a; Breider et al., 2014; Yang et al., 2018; Sobhani et al., 2018). Whereas in the summertime Arctic BL, sulfate concentrations are dominated by emissions of dimethylsulfide from Arctic marine sources (e.g., Breider et al., 2014; Yang et al., 2018). Sulfur emissions from volcanoes or Smoking Hills in northern Canada may episodically impact Arctic surface concentrations (e.g., Radke and Hobbs, 1989; Breider et al., 2014; Leaitch et al., 2018).

The summertime Arctic BC burden is mainly controlled by vegetation fires, whereas anthropogenic sources contribute less to the overall transport of BC to Arctic regions in summer (Bourgeois and Bey, 2011; Stohl et al., 2013; Breider et al., 2014; Xu et al., 2017; Winiger et al., 2019; Zhu et al., 2020). Nevertheless, anthropogenic BC sources in northern Eurasia can have important contributions to Arctic near surface concentrations, whereas South Asian BC layers are present in the Arctic middle and upper troposphere (Singh et al., 2010; Huang et al., 2010; Bourgeois and Bey, 2011; Sobhani et al., 2018). Regarding high-latitude anthropogenic sources, recent studies demonstrated oil/gas extraction activity and shipping to significantly impact the lower tropospheric BC, organic, and sulfate aerosol burdens (e.g., AMAP, 2010; Eckhardt et al., 2013; Breider et al., 2014; Ferrero et al., 2016; Gunsch et al., 2017; Creamean et al., 2018; Kirpes et al., 2018). The contribution of high-latitude flaring emissions to Arctic BC concentration is controversially discussed. While some studies suggest gas flaring to be an important source of BC, particularly in winter and spring (Stohl et al., 2013; Xu et al., 2017; Leaitch et al., 2018; Zhu et al., 2020), others provide evidence that flaring plays a minor role (Winiger et al., 2017, 2019).

Although considerable advances have been achieved in recent years, the majority of our current understanding of aerosol properties in the summertime Arctic is obtained from ground-based and shipborne measurements. In particular, airborne studies that attribute aerosol physical and chemical properties to sources are sparse, especially in summer (Radke and Hobbs, 1989; Brock et al., 1989; Paris et al., 2009; Schmale et al., 2011; Quennehen et al., 2011; Matsui et al., 2011a, b; Kupiszewski et al., 2013; Creamean et al., 2018). However, detailed knowledge on the vertical structure of aerosol composition and mixing state as well as the related particle sources, formation, and aging processes are necessary to have a predictive understanding of our Arctic climate system; yet, the vertical distribution of summertime Arctic aerosol is not well represented in Arctic models (e.g., Quinn et al., 2008; Moore et al., 2011; Eckhardt et al., 2015; Sato et al., 2016; Sand et al., 2017; Willis et al., 2018; Abbatt et al., 2019). Our study thus focuses on processes and sources controlling summer Arctic aerosol, using vertically resolved measurements of aerosol properties and trace gases, together with Lagrangian air mass history analysis. To our knowledge, this is the first comprehensive source attribution study of summertime Arctic aerosol composition, combining airborne single particle and bulk chemical composition methods, with focus on the vertical structure.
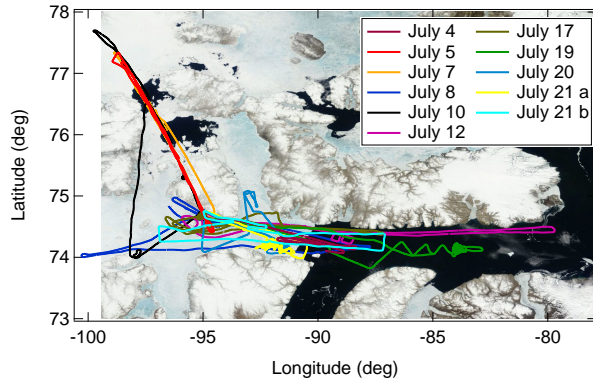
Figure 1. Satellite image (visible range from MODIS) from 4 July 2014 with a compilation of flight tracks conducted during 4 - 21 July 2014 (indicated with different colors). On 21 July 2014, two flights were performed indicated by a and b in the legend.

2 Experimental and Modeling Methods

2.1 Airborne Arctic field experiment NETCARE 2014

120 Motivated by limited knowledge of summertime Arctic aerosol processes, the aircraft campaign NETCARE 2014 took place from Resolute Bay, Nunavut (Canada) from 4 - 21 July 2014 (Fig. 1). This was part of the NETCARE project (Network on Climate and Aerosols: Addressing Key Uncertainties in Remote Canadian Environments; Abbatt et al., 2019). Resolute Bay faces the Northwest Passage with Lancaster Sound near Baffin Bay and Nares Strait (see Fig. 1 in Köllner et al., 2017). Airborne measurements of aerosol physical and chemical properties, trace gases as well as meteorological parameters were performed

125 onboard the AWI Polar 6 aircraft, a DC-3 aircraft modified to a Basler BT-67 for operation in cold and harsh environments (Herber et al., 2008). Eleven flights were conducted from Resolute Bay (Fig. 1). The total sampling time was about 44 hours, of which roughly half of the time has been spent each in the BL and the FT. Flight tracks covered altitudes typically up to 3.5 km, while the flight on 8 July reached altitudes up to 6 km.

The measurements took place largely over remote areas characterized by open water (Lancaster Sound and polynyas north of

130 Resolute Bay), sea ice, and Arctic vegetation (Fig. 1). The sharp transition between open water and sea ice was situated approximately 150 km south-east of Resolute Bay (Fig. 1). Local anthropogenic pollution might have affected the measurements, but is primarily related to the sparse Arctic settlements with domestic activities, traffic, landfill and waste burning as well as local airports, and electric power generators (Aliabadi et al., 2015). The nearest neighboring communities are Arctic Bay and Grise Fjord approximately 360 km from Resolute Bay. In summary, the remoteness of the Resolute Bay region provided a

135 well-suited location for studying the pristine summertime Arctic atmosphere with access to open water regions.

2.2 Aerosol particle composition measurements

2.2.1 Single particle mass spectrometer - ALABAMA

The Aircraft-based Laser ABlation Aerosol MAss spectrometer (ALABAMA) was deployed on the Polar 6 aircraft during the Arctic field experiment, to provide on-line measurements of single particle chemical composition and size. The instrument has been described before in detail (Brands et al., 2011; Roth et al., 2016; Schmidt et al., 2017; Köllner et al., 2017) and is only briefly reviewed here. Particles enter the system through a critical orifice (for details see Molleker et al., 2020). The following Liu-type aerodynamic lens focuses particles into a narrow beam (Liu et al., 1995a, b, 2007). Further, particles are optically detected by scattering light when passing through two orthogonal detection laser beams ($\lambda = 405$ nm). The scattered light is focused by elliptical mirrors and further detected by photomultiplier tubes. This setup provides the particle's time of flight and thus its velocity. The vacuum aerodynamic diameter (d_{va}) can be derived from the velocity, using a calibration with particles of known size, density, and shape (here, monodisperse PSL particles in a size range between 190 nm and 800 nm). During NETCARE 2014, the ALABAMA analyzed particles in a size range between 320 nm and 870 nm (d_{va}). The lower and upper size cut-offs are defined by the size range that include 98 % of all particles analyzed during NETCARE 2014. The successfully detected and sized particles are ablated and ionized in the high-vacuum region by a single triggered laser shot ($\lambda = 266$ nm). The generated ions are guided into a Z-shaped Time-of-Flight mass spectrometer that provides bipolar mass spectra of individual particles. Details on the data analysis can be found in Sect. 2.4

2.2.2 Aerodyne High-Resolution Time-of-Flight aerosol mass spectrometer - HR-ToF-AMS

Sub-micron ensemble aerosol composition in a size range between 75 and 900 nm was measured by an Aerodyne High-Resolution Time-of-Flight aerosol mass spectrometer (HR-ToF-AMS), complementary to the ALABAMA single particle analysis. The HR-ToF-AMS is based on particle thermal vaporization by contact with a heated surface ($\sim 650\,°C$) followed by electron impact ionization (e.g., DeCarlo et al., 2006), in contrast to the ALABAMA laser-induced ablation/ionization process. The HR-ToF-AMS allows quantitative mass concentration measurements of non-refractory aerosol particle components. In practice, organic matter, nitrate, sulfate, ammonium, and methanesulfonic acid (MSA) are detected. To note, we further present the ratio of organic-to-sulfate mass concentrations measured by the HR-ToF-AMS. For further details see Willis et al. (2016, 2017) and Table S3. Both aerosol mass spectrometers, the ALABAMA and the HR-ToF-AMS, were not operated at altitudes above 3.5 km to avoid damages under low pressure conditions in the cabin.

2.2.3 Single Particle Soot Photometer - SP2

Concentration of particles containing refractory black carbon (rBC) was acquired with a Single Particle Soot Photometer (SP2) manufactured by DMT (Schwarz et al., 2006; Gao et al., 2007). The instrument includes a continuous intra-cavity Nd:YAG laser ($\lambda = 1064$ nm) to classify individual particles as incandescent. The peak incandescence signal is linearly related to rBC

mass. The instrument detects particles in a size range between 85 and 700 nm. For further details see Schulz et al. (2019) and Table S3.

2.3 Complementary experimental methods

Meteorological and state parameters were measured by the AIMMS-20 by Aventech Research Inc., integrated on the Polar 6 aircraft. The module Air-Data Probe provides temperature, pressure, relative humidity, wind direction, wind speed, and the three-dimensional aircraft-relative flow vector (true air speed, angle of attack, and side slip). The second module, a GPS, processes satellite navigation signals and determines aircraft three-dimensional position and altitude (Aventech, 2018).

Carbon monoxide (CO) mixing ratios were measured by an Aero-Laser ultra-fast CO monitor (model AL 5002), based on the fluorescence of CO in the vacuum ultraviolet (VUV) at 150 nm (Scharffe et al., 2012; Aero-Laser GmbH, 2013; Wandel, 2015; Bozem et al., 2019). Here, CO is used as an indicator of air masses influenced by combustion sources, including fossil fuel, and biomass burning combustion (Andreae and Merlet, 2001). Further details can be found in Bozem et al. (2019) and Table S3.

Number concentrations of particles between 85 nm and 1000 nm were measured with the Ultra-High Sensitivity Aerosol Spectrometer (UHSAS), manufactured by DMT. The instrument is based on particle light scattering technique. Particles that cross the beam of a laser ($\lambda = 1054$ nm) are counted and sized by their scattering signals. The intensity of the scattered light provides information on the optical diameter (d_{opt}) (e.g., Cai et al., 2008; Schulz et al., 2019). For further details see Schulz et al. (2019) and Table S3. For the conversion of the ALABAMA fraction into number concentration (see Sect. 2.4), UHSAS number concentrations in a size range between 320 nm and 870 nm ($N_{>320}$) are used (see Sect. 2.2.1). Sampling strategy and inlet setups are discussed in detail by the following related publications: Leaitch et al. (2016); Willis et al. (2016, 2017); Aliabadi et al. (2016b); Burkart et al. (2017); Köllner et al. (2017); Bozem et al. (2019); Schulz et al. (2019).

2.4 Analysis of the ALABAMA single particle mass spectrometer data

The marker ion method is used to classify particles measured by the ALABAMA (see Köllner et al., 2017). The ion marker method classifies particles based on the presence of pre-selected species that are of interest. This approach is not dependent on the absolute value of the ion peak areas within one spectrum, but only on the presence of a certain ion peak area above a defined threshold value. In principle, four analysis steps are required. First, a pre-selection of chemical compounds that are of interest for the study is necessary. Second, ion markers of laboratory-generated particles with known composition are compared to ions from ambient particles detected during the field experiment. Third, a threshold for the ion peak area is determined to distinguish the ion signal from background noise (for details see Köllner et al., 2017). Finally, internal and external mixtures of chemical compounds are distinguished by checking if the respective ions occur in the same particle mass spectrum or in separate particle mass spectra. Both types of mixtures can be presented in a decision tree. The decision tree is structured as follows: upper/lower branches refer to positive/negative response for whether ion markers of the respective substance are above/below the ion peak threshold. This study focuses on six particle types based on the presence of the following substances (see Table 1): sodium and/or chloride and/or nitrate (Na/Cl/Nitrate), elemental carbon (EC), nitrate (NO$_3$), trimethylamine (TMA), dicar-

Table 1. Particle classification by marker species and associated ion markers applied in this study. References from laboratory and field studies using single particle mass spectrometry are indicated by numbers that are defined below. This table is partly adapted from Köllner et al. (2017).

Marker species (abbreviation)	Ion markers	References (lab/field)	Comments
Trimethylamine (TMA)	m/z +59 $((CH_3)_3N^+)$ and +58 $(C_3H_8N^+)$	1,2/3,4,5	
Sodium and/or chloride and/or nitrate (Na / Cl / Nitrate)	m/z +23 (Na^+) and (at least two of the following ions) +46 (Na_2^+), +62 (Na_2O^+), +63 (Na_2OH^+); (at least one of the following isotopic patterns/ions) +81/83 (Na_2Cl^+), -35/37 (Cl^-), -93/95 $(NaCl_2^-)$, -46 (NO_2^-), -62 (NO_3^-)	6,7,8/9,3	Isobaric interference with MSA at m/z -95
Elemental carbon (EC)	(at least six of the following ions) m/z +36, +48, ..., +144 (C_{3-12}^+) and/or (at least six of the following ions) m/z -36, -48, ..., -144 (C_{3-12}^-)	7,8/3,10	Except m/z -96 due to isobaric interference with SO_4^-
Low-molecular weight dicarboxylic acids (DCA)	(at least one of the following ions) m/z -89 $(C_2HO_4^-)$, m/z -103 $(C_3H_3O_4^-)$, m/z -117 $(C_4H_5O_4^-)$	11/12,13,14	representative: oxalic acid malonic acid succinic acid
Nitrate (NO₃)	(at least one of the following ions) m/z -46 (NO_2^-), -62 (NO_3^-)	10,11/3,7	
Potassium (K)	m/z +39/41 (K^+)	7, Fig. S5 (this study)/3,15,16	

Given reference numbers are defined as follows: [1]Angelino et al. (2001),[2]Köllner et al. (2017),[3]Roth et al. (2016),[4]Healy et al. (2015),[5]Rehbein et al. (2011),[6]Prather et al. (2013),[7]Schmidt et al. (2017),[8]Brands (2009),[9]Sierau et al. (2014),[10]Brands et al. (2011),[11]Silva and Prather (2000),[12]Lee et al. (2003),[13]Sullivan and Prather (2007),[14]Yang et al. (2009),[15]Hudson et al. (2004),[16]Pratt et al. (2011).

boxylic acids (DCA), and potassium (K). We choose these substances because they are well suited to study aerosol sources as well as aerosol processing along transport that are subjects of this work, such as marine, vegetation fires, and anthropogenic sources. We further analyzed ion peaks that might correspond to levoglucosan, but the marker ions are ambiguous (see Sup-
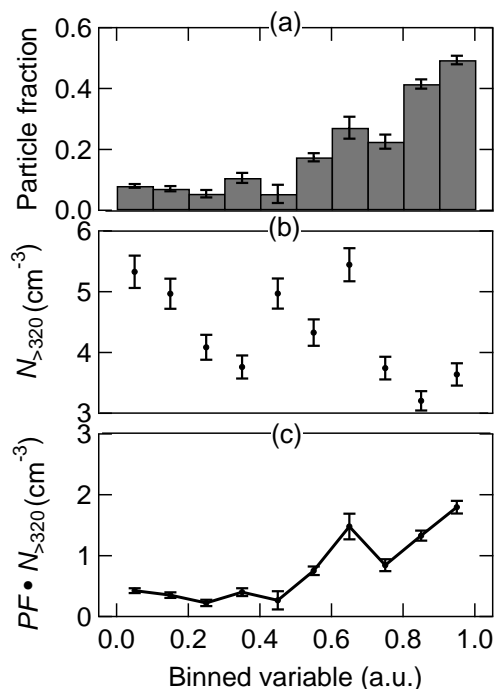
Figure 2. Example for the three-step scaling procedure. (a) The ALABAMA number fraction of the specific particle type (PF), (b) the averaged UHSAS number concentration in a size range between 320 nm and 870 nm ($N_{>320}$), (c) and the scaled ALABAMA number concentration ($PF \cdot N_{>320}$) are compared with variables that are simultaneously measured. In this study, we used the following variables: FLEXPART PES fractions, altitude, H/C ratio, O/C ratio, and CO mixing ratio.

plement Sect. 4). As a result, we will not discuss levoglucosan in this analysis.

In the following, we present the conversion of unscaled ALABAMA measurements into quantitative particle number concentrations. Several studies using single particle mass spectrometry applied a similar scaling procedure (e.g., Qin et al., 2006;

205 Healy et al., 2013; Gunsch et al., 2018; Froyd et al., 2019). Based on particle classification, the fraction of the ALABAMA particle types is calculated (Fig. 2a). To determine particle fractions, total analyzed (i.e., detected+ablated/ionized) particles and specific particle types that are of interest are categorized into bins of a simultaneously measured variable (see horizontal axis in Fig. 2). For each bin, the particle fraction is defined as the number of particles of the specific type divided by the number of all analyzed particles (PF; see Fig. 2a). To note, the following use of the word *fraction* always refers to the number frac-

210 tion measured by the ALABAMA. Bin widths are chosen to guarantee an acceptable level of both statistical significance and resolution. Bins containing less than 20 spectra in total were excluded from the analysis. Further, the particle fraction is scaled to number concentrations, using measurements of a co-located quantitative reference instrument, here the UHSAS onboard the Polar 6 (see Sect. 2.3). The UHSAS number concentration in a size range between 320 nm and 870 nm ($N_{>320}$; Fig. 2b) is used. The selected UHSAS lower and upper size cut offs refer to the ALABAMA size range measured during NETCARE 2014 (see

Sect. 2.2). Conceptually, scaled number concentrations of the ALABAMA particle types are determined by multiplying the particle fraction with the averaged UHSAS number concentration in each bin ($PF \cdot N_{>320}$; Fig. 2c).

By using this scaling method, it is assumed that the d_{opt} measured by the UHSAS and the d_{va} measured by the ALABAMA are equal. It is further assumed that the ALABAMA transmits, detects, and ablates/ionizes all particles with the same efficiency. These assumptions introduce uncertainties in the scaled number concentrations, as the detection efficiency (DE) and the hit rate are observed to be dependent on several factors. The DE is size-dependent, mainly caused by the transmission efficiency of the aerodynamic lens and the optical detection (Zhang et al., 2004; Liu et al., 2007; Brands et al., 2011). However, a size-dependent scaling factor was not deployed in this study, owing to the low particle counting statistics per bin. As a result, the scaling method may lead to uncertainties when determining the concentration of particles smaller than approximately 400 nm. Likewise, the hit rate in laser ablation/ionization technique is dependent on various particle characteristics, such as size, composition, and shape (Thomson et al., 1997; Kane et al., 2001; Moffet and Prather, 2009; Brands et al., 2011). The hit rate can thus vary during ambient measurements, which may cause a problem when interpreting the fraction of particle types. Further details on the hit rate variability during NETCARE 2014 are given in the Supplement Sect. 1.

Given that the scaled number concentration is estimated under several assumptions, we solely discuss trends in number concentrations in comparison with other parameters to identify sources of different particle types, rather than discussing the absolute number concentration. In addition, we will only discuss trends that are clearly visible in both the number fraction and scaled concentration. For clarity, we focus on the scaled number concentration ($PF \cdot N_{>320}$) in the following sections. Additional figures showing particle fraction and averaged UHSAS number concentration are in given in the Supplement Sect. 6.

2.5 Air mass history modeling

2.5.1 FLEXPART

Air mass history analysis is crucial for understanding aerosol sources and transport processes, both of which control aerosol properties in Arctic regions. In this study, we use the Lagrangian FLEXible PARTicle dispersion model (FLEXPART, version 10.0). FLEXPART is a comprehensive tool for modeling atmospheric transport (e.g., Stohl, 1998; Stohl et al., 2003, 2005) and is widely used in Arctic studies (e.g., Stohl, 2006; Paris et al., 2009; Schmale et al., 2011; Evangeliou et al., 2019; Zhu et al., 2020). In this study, FLEXPART was operated backward in time with operational data from the ECMWF with 0.25° horizontal and 3 hours temporal resolution as well as with 137 vertical hybrid sigma-pressure levels. Tracer air parcels (usually called tracer particles) are released from a certain receptor location and followed for 15 days backward in time (Stohl et al., 2003; Seibert and Frank, 2004; Stohl et al., 2005). The receptor location depends on airborne sampling location. In detail, 20000 tracer particles were initialized each 10-min sampling interval along the flight track. By this approach, between 16 and 29 releases were created for each flight, depending on flight duration. The release volume of the tracer particles for each 10-min interval was set by the maximum and minimum geographic locations during this time segment. The main variable calculated by FLEXPART is the so-called Potential Emission Sensitivity (PES) that describes the sensitivity of air sampled at the receptor to source emission locations (Seibert and Frank, 2004; Stohl et al., 2005; Hirdman et al., 2010). The PES value has the dimension
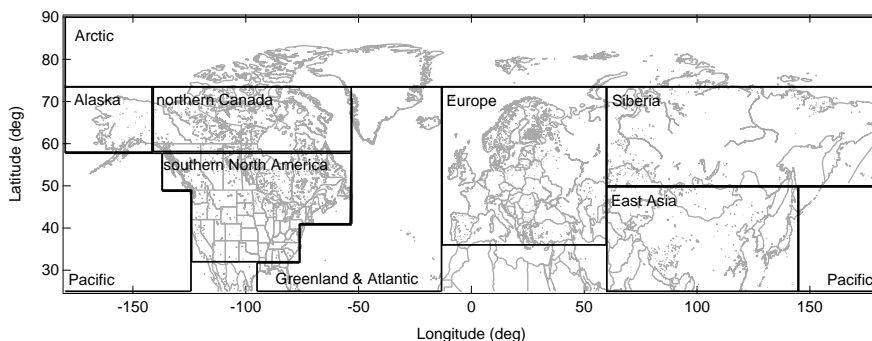
Figure 3. Map showing selected source regions: Arctic, Alaska, northern Canada, southern North America, Pacific, Greenland & Atlantic, Europe, Siberia, and East Asia.

of seconds and essentially is proportional to the parcel's residence time in a particular output grid cell (Seibert and Frank, 2004; Hirdman et al., 2010). It is assumed that each source contributes with unit strength in the respective cell. Further, the transported

250 tracer is inert, which means no impact of precipitation and no chemical reactions are considered in FLEXPART (Stohl et al., 2003; Hirdman et al., 2010). The PES function is provided every six hours (i.e., 60 values for a 15 day backtrajectory), with uniform horizontal grid spacing of $0.25°$, and with five vertical levels (400, 1000, 2000, 5000, and 15000 m).

FLEXPART output combined with geographical locations of emission sources may provide a more detailed analysis of the relationship between Arctic aerosol composition and sources. This analysis requires the following data processing steps: First,

255 the total residence time of air masses in each grid cell is obtained by integrating PES data in time for a given vertical layer. It is assumed that surface emissions into this vertical layer, the so-called footprint layer, are mixed instantaneously by turbulence in the BL. Therefore, the lowest vertical level (0 - 400 m) is applied for most ground sources (e.g., Stohl et al., 2013), except for vegetation fires related to buoyant effects (see details in the Supplement Sect. 2.1). Second, we show maps that specify geolocations of source sectors and source regions (see Sect. 2.5.2). Third, the prior obtained two-dimensional (latitude and

260 longitude) PES map is folded with the two-dimensional map of source regions and sectors. Finally, each grid cell is summed to obtain the total residence time of sampled air mass spent over a specific source within the 15 days prior to sampling and within the vertical footprint layer. In general for this study, the PES fraction is defined as the ratio of the PES of sampled air above source regions/sectors within the footprint layer of the model domain over a 15-days integrated backward simulation compared to the PES of sampled air in the total vertical column of the model domain over a 15-days integrated backward simulation.

265 **2.5.2 Source regions and sectors**

Geolocations of selected source regions (e.g., Europe) and sectors (e.g., vegetation fires) are visualized using two-dimensional maps with horizontal grid spacing of $0.25°$. Geographical regions that likely contribute to Arctic aerosol in summer comprise primarily northern Eurasia, North America, East Asia, and the Arctic itself (e.g., Stohl, 2006; Shindell et al., 2008; Bourgeois and Bey, 2011; Liu et al., 2015; Yang et al., 2018). However, we consider Europe and Siberia as well as Alaska, northern

11

Table 2. Geographical extent of chosen source regions

Region	Latitude (deg)	Longitude (deg)	Latitude (deg)	Longitude (deg)	Latitude (deg)	Longitude (deg)
Arctic (July 2014*)	+73.5 - +90	−180 - +180				
Europe	+25 - +73.5	+13 - +60				
Siberia	+50 - +73.5	+60 - +180				
East Asia	+25 - +50	+60 - +145				
Alaska	+58 - +73.5	−141 - −180				
northern Canada	+58 - +73.5	−60 - −145				
southern N. America	+32 - +58	−76 - −124	+49 - +58	−124 - −137	+41 - +58	−53 - −76
Pacific	+25 - +50	+145 - +180	+25 - +49	−124 - −180	+49 - +58	+137 - +180
Greenland & Atlantic	+25 - +73.5	−13 - −53	+32 - +41	−53 - −76	+25 - +32	−76 - −95

*according to Bozem et al. (2019)

Canada (nCa), and southern North America (sNA) separately due to differences in vegetation fire occurrence, industrial sources, flaring spots, population density (Figs. 4a-d, respectively), and meteorological conditions. Large marine areas of the Pacific and Atlantic Oceans are also included due to their vicinity to Arctic regions. Definitions of the source regions were chosen according to prior Arctic studies (Stohl, 2006; Shindell et al., 2008; Liu et al., 2015; Yang et al., 2018), except for the Arctic. For our July 2014 study, Arctic regions are specified as located north of 73.5° N, based on the July 2014 polar dome location determined by Bozem et al. (2019). Table 2 and Figure 3 provide the geographical extent of the chosen source regions.

Details on creating maps (Fig. 4) that specify the geolocation of the following source sectors: vegetation fires, industry, flaring, population, and Arctic open water, are given in the Supplement Sect. 2. Briefly, for identifying vegetation fire spots, we used data from the Visible Infrared Imaging Radiometer Suite (VIIRS) onboard the Suomi National Polar-Orbiting Partnership spacecraft. These measurements provide sub-pixel thermal anomalies by signals in mid- and thermal infrared spectral range (Schroeder et al., 2014; Schroeder and Giglio, 2018). However, thermal anomalies typically include both active vegetation fires and industrial heat sources by fossil-fuel combustion etc. Therefore, anthropogenic heat sources, such as industry, flaring, and densely populated regions, are separately mapped (as explained below) and subsequently excluded from the thermal anomaly map. Residual heat sources in Fig. 4a thus present vegetation fires. Industrial areas, including flaring, are obtained by using quantitative estimates of infrared source emission temperatures from the Nightfire product from VIIRS (Figs. 4b and c). This method is taking advantage of absent solar reflectance in short-wave infrared spectral range during night (Elvidge et al., 2013, 2016). Emission temperatures typically exhibit bimodal distributions by a combination of gas flares dominating the upper mode (peaking in the 1600 - 2000 K range) and other industrial heat sources as well as vegetation fires dominating the lower mode (peaking in the 800 - 1200 K range; Elvidge et al., 2016; Liu et al., 2018). Geolocation data on population are provided online (MaxMind, 2018). The criteria for the map grid cell to be classified as populated is given by more than 1000 people living in a 0.25° x 0.25° area (Fig. 4d). Finally, we used measurements from the Special Sensor Microwave Imager/Sounder (SSMIS)
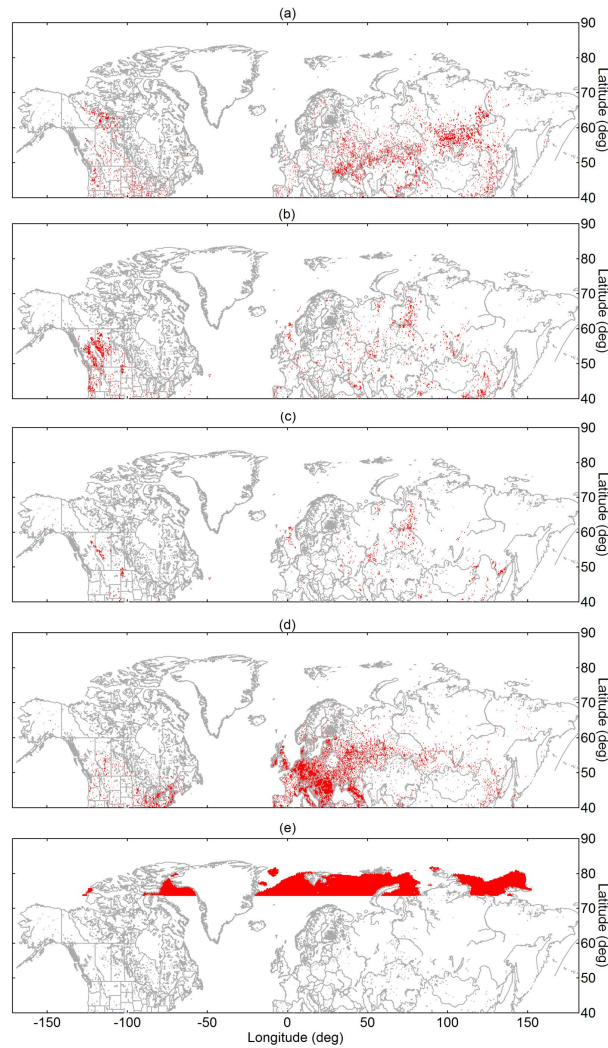
Figure 4. Map showing the geolocation of selected source sectors: (a) vegetation fires, (b) industry (including flaring), (c) flaring, (d) population, and (e) Arctic open water. Panel (a) shows accumulated fires from 19 June to 21 July 2014. Red pixels indicate the presence of the respective source sector irrespective of the particular emission strength.

onboard the Defense Meteorological Satellite Program (DMSP) to assess Arctic sea ice coverage and open water areas in July 2014 (Fig. 4e). Data on sea ice coverage are based on detected brightness temperature (Cavalieri et al., 1996, updated yearly). In general, these approaches classify whether the source sector is present or absent in the grid cell irrespective from source strengths, rather than providing quantitative source-specified emission data.

295 Different source sectors can contribute to air mass history within the 15 days prior to sampling. The Supplement Sect. 9 shows comparisons of PES fractions between different source sectors. It was found that air masses with high Arctic open water PES fraction were largely isolated from other sources; whereas anthropogenic sources (industrial and populated areas)

13
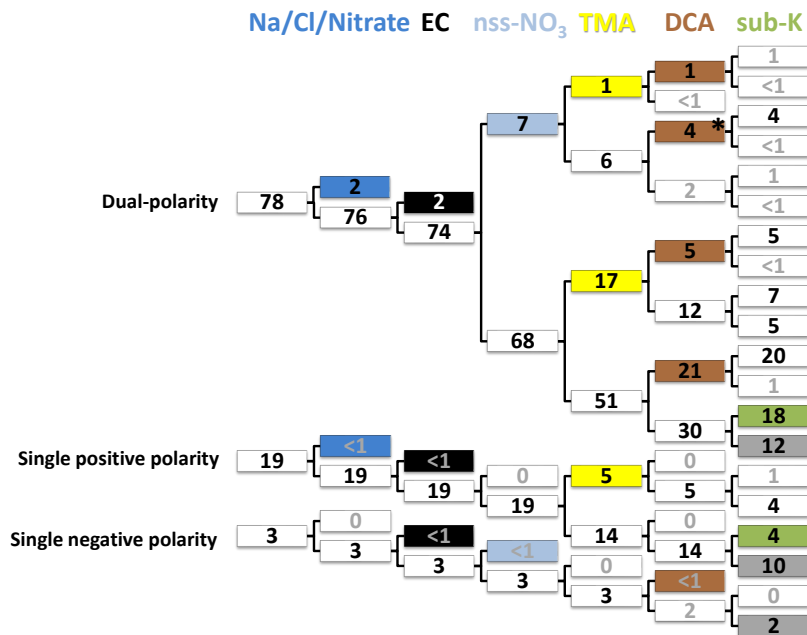
Figure 5. Classification of 10137 single particle spectra based on the ion marker method and illustrated with the decision tree (see Sect. 2.4). Upper/lower branches refer to the presence/absence of substances in the particle mass spectra. Numbers are given as relative abundances in % normalized to 10137 particles. The initial classification provides three groups of particle mass spectra with dual-, single positive, and single negative polarity. Particle types, indicated by colors, contain: Na/Cl/Nitrate (dark blue), EC (black), non-sea-spray-(nss)-NO$_3$ (light blue), trimethylamine (TMA) (yellow), dicarboxylic acids (DCA) (brown), potassium (sub-K) (green), and "Remaining" (gray filling). As an example, 4 % of 10137 particles (indicated by the asterisk) contain DCA and nss-nitrate (from right to left). The remaining particles are further sub-classified in the Supplement Fig. S8

can contribute on either side to air mass history by their close proximity. However, a pre-processing of the PES fractions was applied, if possible, in order to differentiate different source sector contributions from each other. For example, we could separate contributions of vegetation fires from anthropogenic sources. Further details can be found in the Supplement Sect. 9.

3 Results and discussions

3.1 Single particle chemical composition

By means of the ALABAMA, 10137 particles were analyzed during the NETCARE 2014 study when sampling outside clouds; 94 % of the spectra include size information; 78 % of the spectra have dual polarity (Fig. 5). Potential reasons for the lack of negative ions are discussed in Köllner et al. (2017). It might be that single-polarity spectra are preferably produced in high relative humidity environments (Neubauer et al., 1998; Spencer et al., 2008), in particular in marine environments (Guasco et al., 2014). Particle classification by the ion marker method introduced in Sect. 2.4 is illustrated here by means of a decision
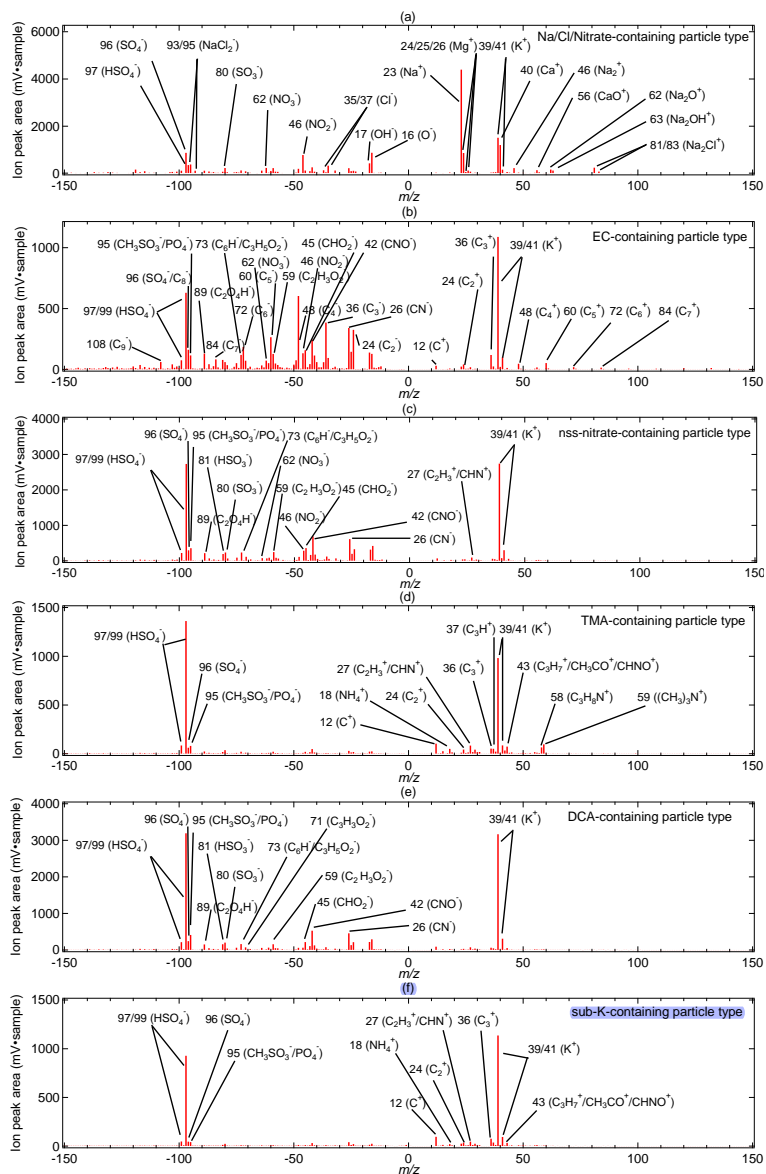
Figure 6. Bipolar mean spectra of the ALABAMA particle types: (a) Na/Cl/Nitrate-containing (195 particles out of 10137 $\widehat{=}$ 2 %), (b) EC-containing (188 particles out of 10137 $\widehat{=}$ 2 %), (c) nss-nitrate-containing (688 particles out of 10137 $\widehat{=}$ 7 %), (d) TMA-containing (2325 particles out of 10137 $\widehat{=}$ 23 %), (e) DCA-containing (3150 particles out of 10137 $\widehat{=}$ 31 %), and (f) sub-K-containing (2210 particles out of 10137 $\widehat{=}$ 22 %).

tree in Fig. 5. Particle groups that include less than 300 particles (~3 %) are not further sub-classified due to the low counting statistics. This means EC- and Na/Cl/Nitrate-containing particles are excluded from other types due to their low number. In

310   contrast, particles that contain substances such as nitrate, TMA, and/or DCA and that are not internally mixed with EC and

Na/Cl can be assigned to several types. TMA-, DCA-, and sub-K-containing particles are the most prominent types with relative contributions of 23 %, 31 %, and 22 % to the total number of analyzed particles, respectively (indicated by yellow, brown and green filling in Fig. 5). In contrast, particles containing Na/Cl/Nitrate, EC, and nitrate (externally mixed with Na and Cl) account for 2 %, 2 %, and 7 %, respectively. 24 % of all mass spectra are not considered for further analysis (gray filling in Fig. 5), however, those remaining mass spectra are further sub-classified with marker species sulfate, ammonium, MSA etc. (see Figs. S8 and S9). In the following, mean spectra of the main particle types (Fig. 6) combined with additional ion signals (Table S2) provide an overview of the averaged chemical composition. To note, percentages given in this study always refer to number percentages measured by the ALABAMA.

The term particulate DCA implies the presence of oxalic, malonic, and/or succinic acid (see Table 1), with oxalic acid as most abundant (in 86 % of DCA particles), followed by succinic acid with 41 % of DCA particles and malonic acid with 38 % of all DCA particles (not shown). It should be noted that the ALABAMA detects oxalate-, malonate-, and succinate ions that most likely originate from oxalic, malonic, and succinic acid, respectively (Silva and Prather, 2000). The majority of the DCA spectra show the concurrent presence of oxidized organics at m/z -45, -59, -71, and -73 (Fig. 6e and Table S2). From our ALABAMA analysis, we can infer that particulate DCA was partly internally mixed with particles containing sodium, chloride, and/or nitrate (Na/Cl/Nitrate), which are interpreted as sea spray particles (Table S2 and Fig. S7). In detail, the presence of DCA was found in 60 % of those sea spray particles. The presence of DCA together with sea spray had been observed earlier during measurement campaigns with a focus on marine air (Sullivan and Prather, 2007), also in Arctic regions (Kerminen et al., 1999). However, the majority of DCA were not internally mixed with sea spray (Figs. 5 and 6e). Moreover, 14 % of those DCA-containing particles (without sea spray) were internally mixed with TMA and MSA (Figs. 5 and 6e). In our prior study, we concluded that particulate TMA in the Arctic summer results from secondary formation, owing to the external mixture of TMA and primary components, such as sodium (Köllner et al., 2017). Thus, together with the secondary nature of TMA and MSA (Hoffmann et al., 2016), the internal mixture of DCA with TMA and MSA suggests that DCA results from the secondary (potentially aqueous) conversion of precursor gases (e.g., Kawamura and Bikkina, 2016).

Nitrate was also externally mixed with sea spray particles, hereafter referred to as non-sea-spray (nss)-nitrate. The averaged chemical composition of EC- and nss-nitrate-containing types provide evidence for internal mixing with secondary substances such as sulfate, MSA, and oxygen-containing organic matter (OM; Figs. 6b-c and Table S2). In addition, 20 % of the EC particles were internally mixed with nitrate (Fig. 6b and Table S2). More than 50 % of the nss-nitrate- and EC-containing particle spectra include ion signals of DCA (Fig. 5), particularly oxalic acid at m/z -89 (Fig. 6b-c). The majority of the nss-nitrate particles (85 %) were internally mixed with potassium (Figs. 5 and 6c). In contrast to that, the sub-K-containing particle type presents a sub-group that includes potassium-containing particles that are externally mixed with sea spray, EC, nitrate, TMA, and DCA (Figs. 5 and 6f). The mean spectrum is dominated by the presence of potassium and sulfate as well as some small organic peaks in the cation spectrum (Fig. 6f and Table S2). First conclusions on aging and formation of the different particle types were drawn based on the averaged chemical composition and mixing. The following sections provide a detailed discussion on aerosol sources and formation processes during two distinct meteorological periods.
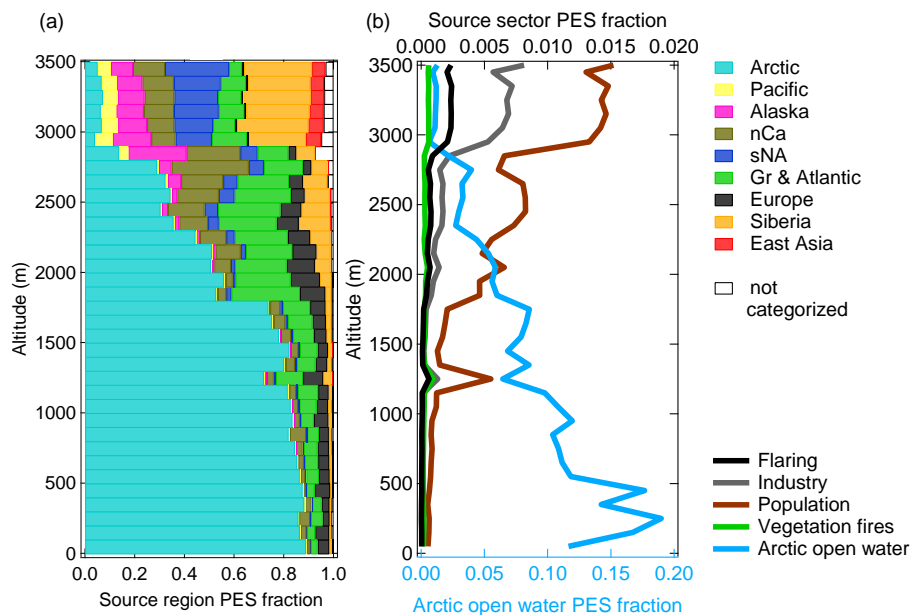
Figure 7. Vertically resolved cumulative contribution of (a) source regions and (b) source sectors to sampling altitude during the Arctic air mass period (July 4-12). For details on flight tracks see Fig. 1. The FLEXPART derived contribution is expressed as a fraction of the potential emission sensitivity (PES) in the model domain lowest vertical level (0 - 400 m, except for vegetation fires) over a 15-days backward simulation. A vertical injection layer between 1 and 5 km is applied for vegetation fires (see details in Sect. 2.5.1). Acronyms in (a) are defined as follows: nCa = northern Canada; sNA = southern North America; Gr = Greenland. The white parts depict areas that are not categorized in the selected geographical regions. Bottom and top axes in (b) represent PES fractions of Arctic open water and other source sectors, respectively.

3.2 Arctic air mass period

Meteorological conditions combined with air mass history play a major role for understanding Arctic aerosol composition influenced by local as well as distant sources and transport. The synoptic situations during NETCARE 2014 have been discussed in previous publications (see Bozem et al., 2019; Burkart et al., 2017; Köllner et al., 2017; Leaitch et al., 2016). Air mass history derived by FLEXPART is summarized in Figs. 7 and 14 as a function of sampling altitude. The synoptic conditions changed over the course of NETCARE 2014 from an initial Arctic air mass period (July 4-12, ∼ 26 measurement hours) to a southern air mass period (July 17-21, ∼ 19 measurement hours) with a transition in between (Burkart et al., 2017; Bozem et al., 2019). Since the different synoptic conditions have a significant impact on the distributions of the observed quantities, we analyze the measurements for each period individually.

17

3.2.1 Meteorological overview and air mass history

355 During the Arctic air mass period, the measurement region was under the influence of a prevailing high-pressure system generally clear skies, some low-level stratocumulus clouds (Leaitch et al., 2016), low wind speeds, and a stable stratified shallow BL (Bozem et al., 2019). Inferred from the vertical profile of pseudoequivalent potential temperature, the local upper BL height was on average between 250 m and 450 m, including a surface-based temperature inversion (Köllner et al., 2017). The representativeness of the Arctic air mass period in July 2014 with respect to climatological conditions is discussed in the

360 Supplement Sect. 3. Briefly, synoptic situations were generally consistent with the climatology.

Air mass history during the first period reflects the concept of isentropic transport to Arctic regions during summer. Klonecki et al. (2003) and Stohl (2006) provide comprehensive analyses on the role of transport pathways into the Arctic troposphere across seasons. Both prior studies show that the Arctic summertime lower troposphere is quite isolated from southern latitude sources as diabatic low-level transport into the polar dome are largely absent. This is in line with our results. We found that the

365 near-surface regions were largely isolated from the rest of the atmosphere, whereas regions aloft were episodically influenced by air originating from southern latitudes (Fig. 7a). The distinct change in air mass history at around 3 km altitude depicts the transition to measurement regions located outside of the polar dome (Fig. 7a; Bozem et al., 2019). The period is referred to as Arctic air mass period since air mass history 15 days prior to sampling shows a dominant influence of air masses from the high Arctic. Inside the BL, we predominantly sampled air masses that had resided in the Arctic regions (up to 90 % in Fig. 7a).

370 Particularly, a significant fraction of the high Arctic air masses has resided over open water (up to 20 % in Fig. 7b). Thus, air masses inside the BL originated to a large degree from pristine Arctic regions with mainly natural aerosol sources affecting composition. Above the BL, influences of Arctic air masses were still pronounced (Fig. 7a). However, contributions from southern latitude regions, i.e. Europe, Siberia, northern Canada, Greenland, and the Atlantic Ocean, increased with altitude due to enhanced quasi-isentropic transport from these regions into the high Arctic (Fig. 7a). The abovementioned studies by Stohl

375 (2006) and Klonecki et al. (2003) demonstrate that emissions in Siberia, Europa, and Asia can influence Arctic summertime composition in altitudes above the BL, which is consistent with our results.

An example of a transport from Europe towards the Arctic is shown in Figure S35. Air masses at low levels over Europe ascended along the upward sloping isentropes when they were transported poleward. Thus, the impact of the emissions from these source regions on our measurements becomes apparent at higher altitudes (Fig. 7a). Air mass history above 3 km altitude,

380 above the polar dome (Bozem et al., 2019), indicates a sharp transition to a dominating influence of mid-latitude air masses (Fig. 7a). The contribution of Siberian regions to air mass history was highest in altitudes above 3 km. Consistent with several modeling studies, contributions of regions south of $50\text{-}60°\,N$ (i.e., East Asia, Pacific, and southern North America) became significantly important only above 3 km, whereas sources in Europe and northern Canada frequently affected measurements in lower altitudes (e.g., Bourgeois and Bey, 2011; Sobhani et al., 2018; Yang et al., 2018). Thus, anthropogenic pollution in

385 altitudes above 3 km can be attributed to sources in East Asia and southern North America (Fig. 7). In general during the Arctic air mass period, the contribution of vegetation fires was negligible (Fig. 7b). This finding is in line with low CO mixing ratios ($< 90\,\text{ppb}_\text{v}$) measured during the first period (Bozem et al., 2019).
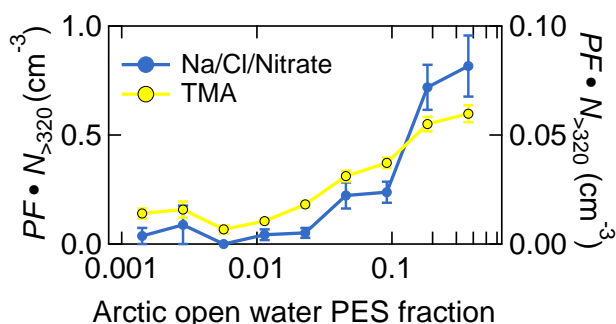
Figure 8. Aerosol composition measured by the ALABAMA as a function of FLEXPART derived PES fraction over Arctic open water areas during the Arctic air mass period. The panel represents the ALABAMA scaled number concentration ($PF \cdot N_{>320}$) with right axis referring to Na/Cl/Nitrate-containing (blue) and left axis referring to TMA-containing (yellow) particles. Uncertainty analyses are given in the Supplement Sect. 7.

3.2.2 Arctic marine influences on particle composition

The clean and pristine Arctic background conditions during the first period provide the unique opportunity to study the influence of Arctic marine sources on particle composition. This section complements the results presented in Köllner et al. (2017) and Willis et al. (2017), both analyzing particle chemical composition during the first period. It was shown that marine processes dominated the presence of organic matter and MSA in low sulfate environments in the summertime Arctic BL (Willis et al., 2017; Köllner et al., 2017). The organic-to-sulfate and MSA-to-sulfate ratios peaked when the residence time over Arctic open water region was highest (Willis et al., 2017). As a new analysis compared to our prior studies, we present the aerosol composition measured by the ALABAMA as a function of FLEXPART derived PES fraction (see Sect. 2.5.1) over Arctic open water areas in Fig. 8 and the vertically resolved aerosol composition in Fig. 9. Particulate TMA was predominantly abundant when the air resided for more than 50 % of the 15 days (PES fraction) prior to sampling over Arctic open water areas (Fig. 8). Along with the marine influence, Na/Cl/Nitrate-containing particles were largely abundant when the residence time over Arctic open water regions was high (Fig. 8), linking those particles to locally emitted sea spray. In addition, both particle types are predominantly present in the Arctic marine BL (Fig. 9). Taken together, air mass history demonstrates that Arctic marine sources contributed to the abundance of particulate TMA internally mixed with MSA, sulfate, and/or other organics as well as sea spray particles in the summertime marine Arctic BL.

3.2.3 Long range transport influences on particle composition

In a next step, we will focus on the particle composition measured in the summertime Arctic lower FT. In contrast to particle composition in the Arctic marine BL, our analysis suggests that particle composition in the Arctic FT was influenced by long range transport (see Sect. 3.2.1). To illustrate this, we show the vertically resolved aerosol composition in Fig. 10 and the aerosol composition as a function of FLEXPART derived PES fraction over different geographical regions in Fig. 13.
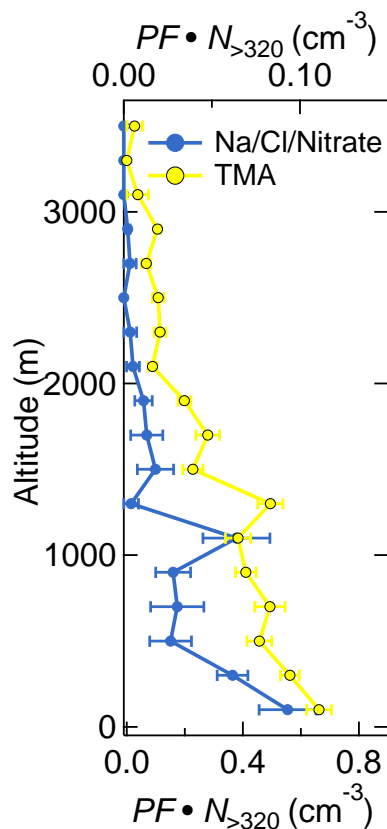
Figure 9. Vertically resolved aerosol composition measured by the ALABAMA during the Arctic air mass period. The panel represents the ALABAMA scaled number concentration ($PF \cdot N_{>320}$) with top axis referring to Na/Cl/Nitrate-containing (blue) and bottom axis referring to TMA-containing (yellow) particles. Uncertainty analyses are given in the Supplement Sect. 7.

During the Arctic air mass period, the ALABAMA analysis suggests that organic matter in the FT was partly composed of particulate DCA. The number concentration of DCA-containing particles was increasing with increasing altitude (Fig.
410   10). Further, Figs. 11 and 12 show the number concentrations of DCA-containing particles in comparison with the HR-ToF-AMS estimated oxygen-to-carbon (O/C) and hydrogen-to-carbon (H/C) ratios as well as with the FLEXPART derived PES fraction over Arctic regions, respectively. The abundance of DCA-containing particles coincided with air masses with more oxidized organic matter (Fig. 11). Consistent with this result, the size distribution of DCA particles is shifted towards larger diameters compared to other particle types (Fig. S11). Finally, air mass history shows that the abundance of DCA-containing
415   particles correlated with time spent outside Arctic regions (Fig. 12). However, no significant trend with a distinct source region outside the Arctic was found (not shown), as expected from the variety of biogenic and anthropogenic precursor gases as well as primary emissions. These results are in line with findings of an Arctic airborne study by Schmale et al. (2011), who demonstrated the presence of low-volatility highly oxygenated organic aerosol in the summertime Arctic FT that was
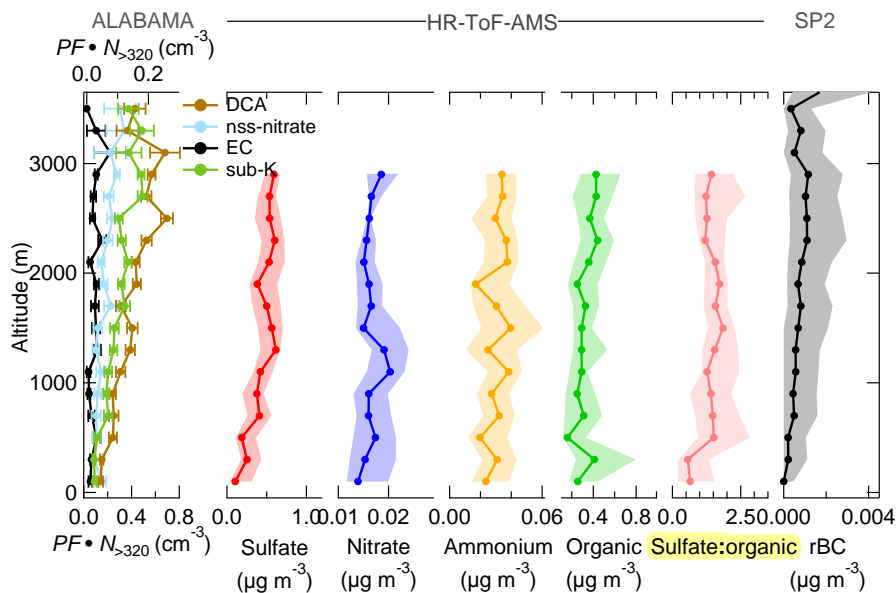
Figure 10. Vertically resolved aerosol composition measured by the ALABAMA, by the HR-ToF-AMS, and by the SP2 (indicated on the top side) during the Arctic air mass period. Note the different scales. Left panel represents the ALABAMA scaled number concentration ($PF \cdot N_{>320}$) with top axis referring to EC-containing (black)- and nss-nitrate (light blue)-containing particles and bottom axis referring to DCA (brown)- and sub-K (green)-containing particles. Right panels represent each median (solid line with marker) and interquartile ranges (shaded area) of the HR-ToF-AMS mass concentrations of sulfate (red), nitrate (blue), ammonium (orange), organic matter (light green), the sulfate-to-organic ratio (pink) as well as the SP2 mass concentration of refractory black carbon (rBC) (black). Uncertainty analyses are given in the Supplement Sect. 7.

transported over long distances from lower latitudes, irrespective of the source sector and regions. The molecular identity

420   of the observed organic aerosol in Schmale et al. (2011) is not known. Direct observations of DCA in Arctic regions exist, however, up to now confined to measurements in the BL (e.g., Shaw et al., 2010; Kawamura et al., 2012; Leaitch et al., 2018). These earlier studies suggest summer minimum concentrations of carboxylic acids, due to a combination of diminished transport of precursors and more efficient aerosol wet removal compared to other seasons. We provide new data on the vertical profile of DCA. It is demonstrated that a significant fraction of DCA was present in the summertime Arctic FT, influenced by

425   long range transport from sources outside Arctic regions. Besides the presence in the FT, DCA-containing particles internally mixed with TMA and MSA (see Sect. 3.1) were largely present in the stable stratified BL (Fig. S12). Further, these particles were detected when the residence time within the Arctic was high (Fig. S13), indicating sources of particulate DCA in the Arctic. This finding is consistent with previous ground-based and shipborne studies (e.g., Kawamura et al., 1996; Kerminen et al., 1999; Kawamura et al., 2010, 2012), partly linking the abundance of DCA in the summertime Arctic to regional sources.

430   Aerosol transport from lower latitudes further influenced Arctic composition by particles that contained nss-nitrate, EC, and potassium. Those particles were more pronounced in the FT compared to the BL (Fig. 10). Air mass history shows contributions
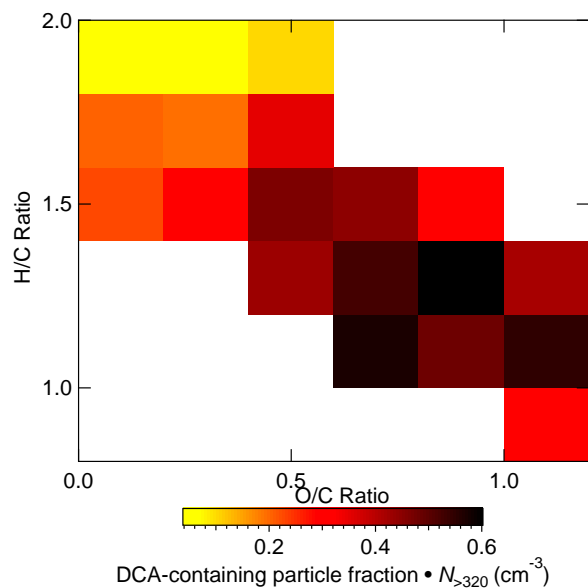
Figure 11. Scaled number concentration ($PF \cdot N_{>320}$) of DCA-containing particles measured by the ALABAMA (colored) as a function of the HR-ToF-AMS estimated oxygen-to-carbon (O/C) and hydrogen-to-carbon (H/C) during the Arctic air mass period. Uncertainty analysis is given in Supplement Sect. 7.
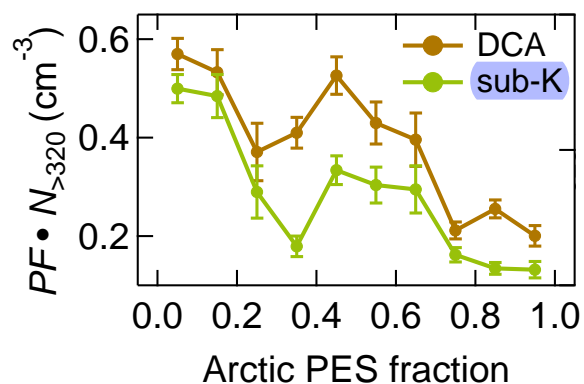

Figure 12. Scaled number concentration ($PF \cdot N_{>320}$) of DCA- and sub-K-containing particles measured by the ALABAMA as a function of FLEXPART derived PES fraction over Arctic regions during the Arctic air mass period. Uncertainty analysis is given in the Supplement Sect. 7.

from East Asia and Europe to aerosol composition (Fig. 13). Figure S33 presents an example of the FLEXPART derived transport pathway from East Asia (particularly Japan) to the Arctic. The advection of those air masses to Arctic regions took
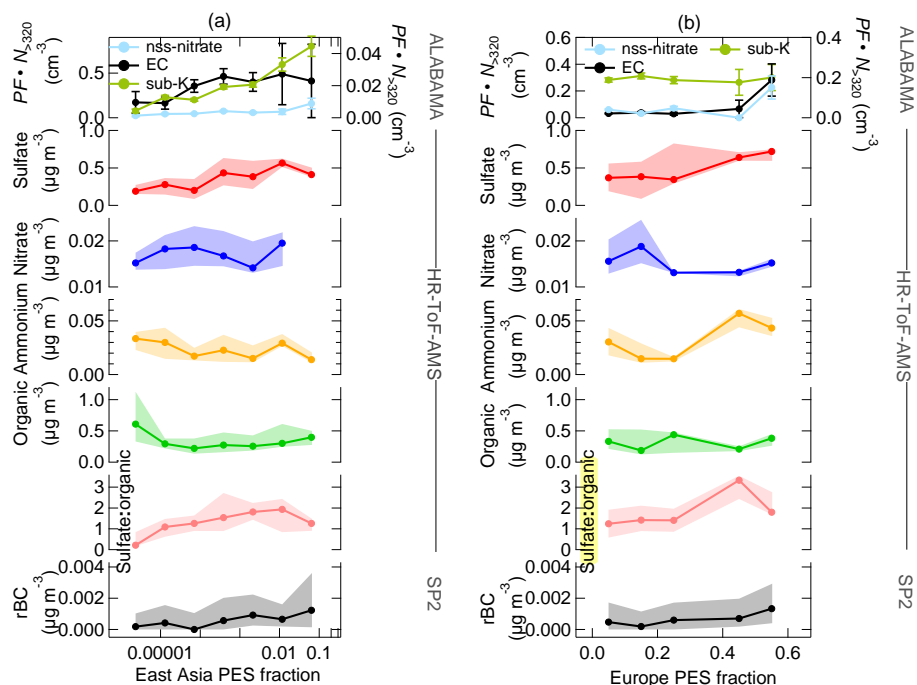
Figure 13. Aerosol composition measured by the ALABAMA, by the HR-ToF-AMS, and by the SP2 (indicated on the right side) as a function of FLEXPART derived PES fraction over East Asia (a) and Europe (b) during the Arctic air mass period. Top panel represents each the ALABAMA scaled number concentration ($PF \cdot N_{>320}$) with right axis referring to EC-containing (black) and with left axis referring to nss-nitrate (light blue)- and sub-K (green)-containing particles. Lower panels represent each median (solid line with marker) and interquartile ranges (shaded area) of the HR-ToF-AMS mass concentrations of sulfate (red), nitrate (blue), ammonium (orange), organic matter (light green), and the sulfate-to-organic ratio (pink) as well as the SP2 mass concentration of refractory black carbon (rBC) (black). Uncertainty analyses are given in the Supplement Sect. 7.

place mainly at altitudes above 1 km. EC and nss-nitrate measured by the ALABAMA and rBC from the SP2 have their sources in Europe and East Asia (Fig. 13). Air mass history further illustrates that elevated concentrations of EC- and nss-nitrate-containing particles occurred when the residence time over populated and/or industrial areas in Europe and East Asia was high (compare Fig. 13 with Fig. S14). Consistent with this analysis, the quantitative analysis of rBC by the SP2 shows qualitatively similar trends (Fig. S14). However, rBC mass concentrations were generally low during the NETCARE 2014 study (Schulz et al., 2019), reflecting the largely isolated nature of the summertime Arctic from the rest of the atmosphere. This is in agreement with previous Arctic measurements of BC (or EC) across seasons (e.g., Matsui et al., 2011b; Winiger et al., 2019), demonstrating particularly low concentrations during summer compared to the rest of the year. Matsui et al. (2011b) could show the influence of Asian anthropogenic emissions on the BC concentration in Arctic summer, in line with our results during the Arctic air mass period. Along with Asian anthropogenic emissions, our results further suggest that anthropogenic sources in East Asia contributed to the abundance of sub-K particles. This particle type correlated with time spent outside Arctic

23

445 regions (Fig. 12), particularly, with time spent over populated and industrial regions in East Asia (Fig. 13a and Fig. S14). Given that the nss-nitrate, EC, and sub-K particle types were predominantly mixed with secondary substances (sulfate, nitrate, and oxygen-containing organic matter; Fig. 6c, b, and f, respectively) and that these particle types were larger in diameter compared to BL particles, such as TMA-containing particles (Fig. S11), we conclude a pronounced influence of particle aging processes while particles were transported to Arctic regions.

450 Measurements by the HR-ToF-AMS combined with air mass history analysis suggest that long range transport from sources outside the Arctic contributed to the abundance of particles containing sulfate and ammonium. Both species show slightly higher mass concentrations in the Arctic FT (Fig. 10). Air mass history suggests that sources in Europe contribute to the presence of particles containing ammonium (Fig. 13b). Sulfate was predominantly abundant when the residence time prior to sampling was high in East Asia and Europe (Fig. 13). In parallel, the sulfate-to-organic ratio was enhanced in the FT (Fig.

455 10) and coincided with time spent over anthropogenic sources in East Asia and Europe (Fig. 13). It has previously been demonstrated that anthropogenic emissions in northern Eurasia and East Asia contribute to enhanced sulfate concentrations in the summertime Arctic FT (e.g., Matsui et al., 2011a; Breider et al., 2014; Yang et al., 2018). In line with this, Schmale et al. (2011) observed an increasing sulfate fraction and decreasing organic fraction along with increasing anthropogenic influence from southern latitudes.

460 ## 3.3 Southern air mass period

3.3.1 Meteorological overview and air mass history

Meteorological conditions changed after 12 July due to a low-pressure system that was initially centered to the west above the Beaufort Sea and finally passed through Resolute Bay on 15 July. Until 17 July, flying was impeded by the local weather situation with low visibility, fog, and precipitation along with the low-pressure system (Burkart et al., 2017). However, the

465 measurement region was increasingly impacted by an intense low-pressure system located south of Resolute Bay that led to a different meteorological situation during the period from 17 - 21 July (Bozem et al., 2019). Meteorological conditions were characterized by overcast sky, occasional precipitation, moist air throughout the lower troposphere, higher wind speeds, and warmer temperatures compared to the Arctic air mass period (Burkart et al., 2017; Bozem et al., 2019). The BL was more difficult to identify compared to the prior period due to a less well defined temperature inversion. According to the detailed BL

470 study by Aliabadi et al. (2016a), the BL height reached altitudes between approximately 200 m and 400 m. However, vertical mixing between the BL and FT was likely promoted caused by a combination of less intense temperature inversions, higher wind speeds, warmer temperatures, and a higher abundance of clouds compared to the first period (e.g., Stull, 1997; Fuelberg et al., 2010; Tjernström et al., 2012).

This period is referred to as southern air mass period, since air mass history shows the prevalence of air masses originating

475 from southern latitudes. Lagrangian air mass history analysis suggests a pronounced impact of southern latitude sources on Arctic composition (Fig. 14). The cumulative contribution of all regions outside the Arctic dominated air mass history within the lower troposphere (Fig. 14a). By comparing the synoptic situation during the southern air mass period with climatological
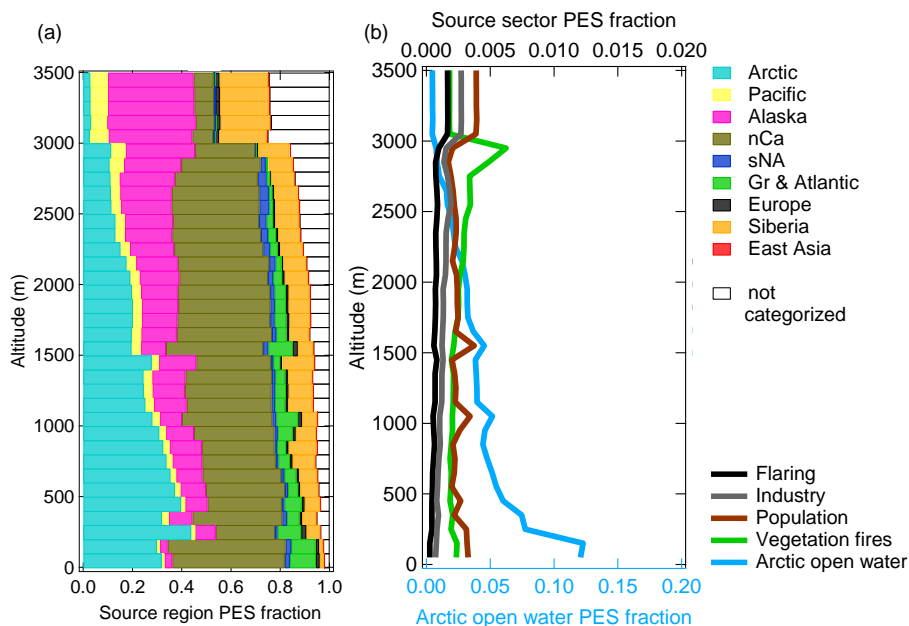
Figure 14. Vertically resolved cumulative contribution of (a) source regions and (b) source sectors to sampling altitude during the southern air mass period (July 17-21). For details on flight tracks see Fig. 1. The FLEXPART derived contribution is expressed as a fraction of the potential emission sensitivity (PES) in the model domain lowest vertical level (0 - 400 m, except for vegetation fires) over a 15-days backward simulation. A vertical injection layer between 1 and 5 km is applied for vegetation fires (see details in Sect. 2.5.1). Acronyms in (a) are defined as follows: nCa = northern Canada; sNA = southern North America; Gr = Greenland. The white parts depict areas that are not categorized in the selected geographical regions. Bottom and top axes in (b) represent PES fractions of Arctic open water and other source sectors, respectively.

mean (see Supplement Sect. 3), we found that the presence of the low-pressure system led to a significantly anomalous synoptic situation. This finding explains the discrepancy between our results on air mass history during the second period and results on Arctic transport climatology by Stohl (2006), revealing a largely unperturbed Arctic lower troposphere during summer.

480 Our results suggest that northern Canada and Alaska exerted the largest influences and the European influence was smaller than during the first period, consistent with the prevailing cyclonic activity south of Resolute Bay. Transport of air masses from northern Canada was accompanied by emissions from vegetation fires in the Great Slave Lake region (compare Figs. 4a and S36). Contributions from industrial and flaring activities were likely accompanied by transport of air masses from Alaska, 485 Siberia, southern North America, and Europe (Fig. 14). Also, the contribution of air masses in the lower FT that had resided above Arctic open water was significantly lower during the southern air mass period compared to the Arctic air mass period (compare Figs. 7b and 14b). Regions that were not categorized (Mexico and northern Africa both north of 25° N, see Fig. 3) contribute significantly to air mass history at altitudes above 3 km (Fig. 14a). However, our data on aerosol composition at altitudes above 3 km are sparse, with the result that our further data analysis is limited to altitudes below 3 km.

25
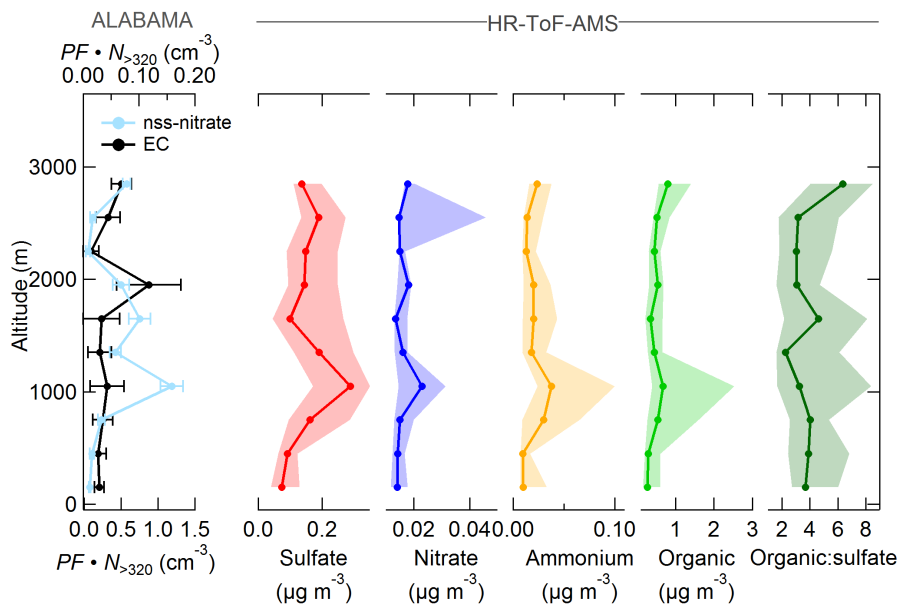
Figure 15. Vertically resolved aerosol composition measured by the ALABAMA and by the HR-ToF-AMS (indicated on the top side) during the southern air mass period. Note the different scales. Left panel represents the ALABAMA scaled number concentration ($PF \cdot N_{>320}$) with top axis referring to EC-containing (black) and bottom axis referring to nss-nitrate (light blue)-containing particles. Right panels represent each median (solid line with marker) and interquartile ranges (shaded area) of the HR-ToF-AMS mass concentrations of sulfate (red), nitrate (blue), ammonium (orange), organic matter (light green), and the organic-to-sulfate ratio (dark green). Uncertainty analyses are given in the Supplement Sect. 7.

3.3.2 Vegetation fire and anthropogenic influences on particle composition

Our measurements combined with air mass history analysis suggest that long range transport of vegetation fire emissions contributed to the abundance of particles containing nss-nitrate, ammonium, organics, and sulfate in the summertime Arctic lower FT. Figure 15 illustrates the vertically resolved aerosol composition during the southern air mass period. We can show that those species were more pronounced in the FT compared to the BL, suggesting the influence of long range transport on aerosol composition. Comparing both periods, the nitrate, ammonium, and organic concentrations measured by the ALABAMA and HR-ToF-AMS were higher during the southern air mass period (compare Figs. 10 and 15), reflecting the pronounced influence of vegetation fires during this time. We used the CO mixing ratio to demonstrate the contribution of combustion sources on aerosol composition (Fig. 16). Additionally, Figs. 17 and 18 provide the aerosol composition as a function of FLEXPART derived PES fraction over different source sectors (including vegetation fires) and over different source regions, respectively. The number concentration of nss-nitrate particles measured by the ALABAMA increased with elevated CO mixing ratios (Fig. 16). In parallel, air mass history shows that nss-nitrate particles were largely abundant when time spent over vegetation fires was high (Fig. 17a). Given that the majority of nss-nitrate-containing particles were internally mixed with potassium (see Sect.
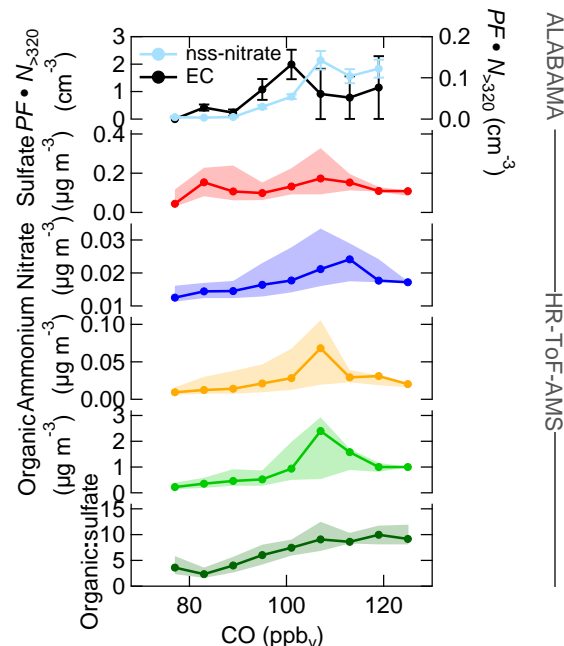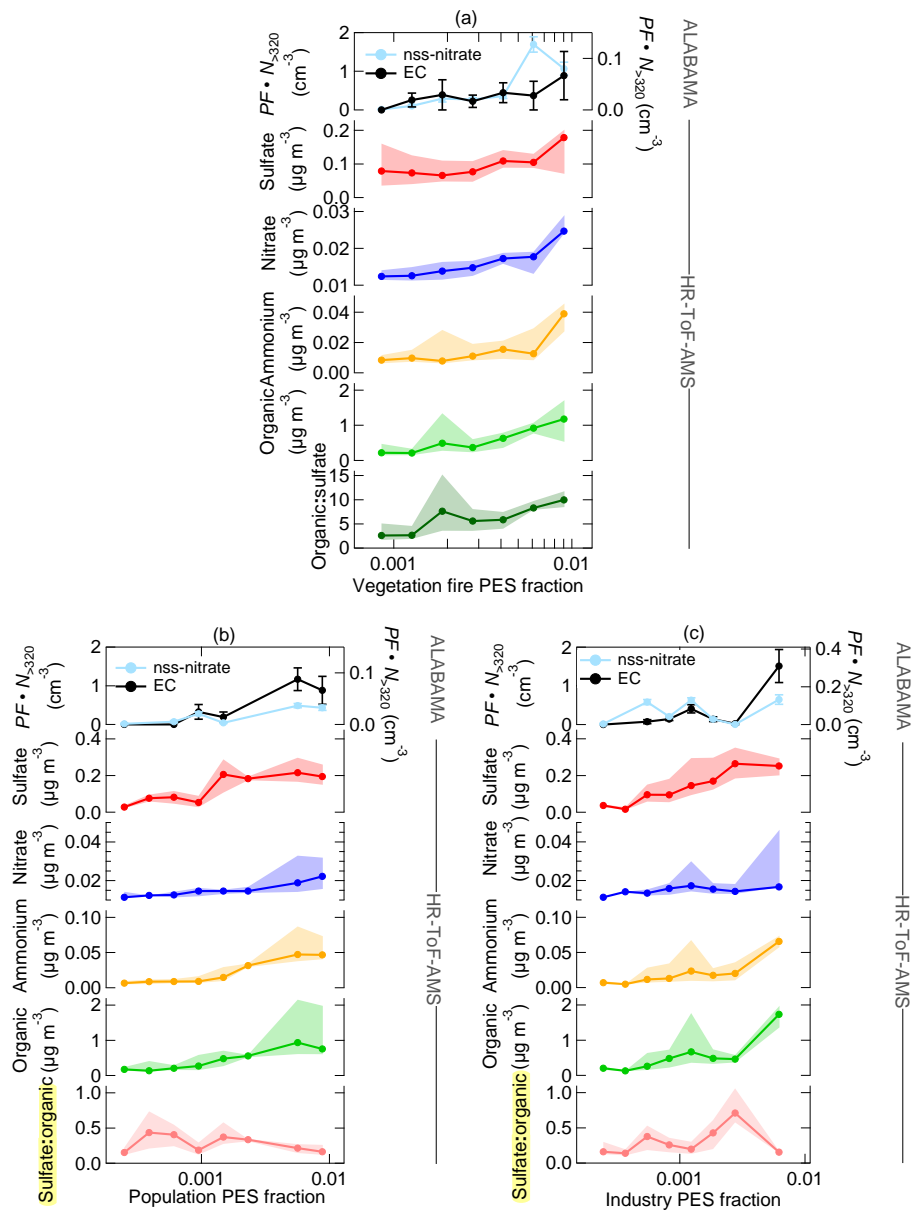
Figure 16. Aerosol composition measured by the ALABAMA and by the HR-ToF-AMS (indicated on the right side) as a function of CO mixing ratios during the southern air mass period. Top panel represents the ALABAMA scaled number concentration ($PF \cdot N_{>320}$) with right axis referring to EC-containing (black) and left axis referring to nss-nitrate-containing (light blue) particles. Lower panels represent each median (solid line with marker) and interquartile ranges (shaded area) of the HR-ToF-AMS mass concentrations of sulfate (red), nitrate (blue), ammonium (orange), organic matter (light green), and the organic-to-sulfate ratio (dark green). Uncertainty analyses are given in the Supplement Sect. 7.

3.1), we have additional indications for their biomass burning origin (Silva et al., 1999; Hudson et al., 2004; Pratt and Prather, 2009; Pratt et al., 2011; Quinn et al., 2002). However, the enhanced abundance of the sub-K particle type (externally mixed

505   with nitrate) with anthropogenic influence shows that potassium does need not necessarily be linked to a biomass burning source (see Sect. 3.2.3). It is thus important to state that the inclusion of nitrate and sulfate with potassium is indicative for atmospheric processing of biomass burning particles while transported into the Arctic.

Consistent with these results, nitrate mass concentrations measured by the HR-ToF-AMS increased with increasing influence from vegetation fires (Fig. 17a). Similar to nitrate, enhanced sulfate and ammonium concentrations measured by the HR-ToF-

510   AMS coincided with both high CO mixing ratios and with time spent over vegetation fires (Figs. 16 and 17a). Along with vegetation fires and high CO mixing ratios, the organic-to-sulfate ratio was increasing, indicating the pronounced influence of vegetation fire emissions on the presence of organic matter in the summertime Arctic FT. Finally, particles containing nss-nitrate, sulfate, ammonium, and organics were present when the residence time over northern Canada was high (Fig. 18a), suggesting that vegetation fires in northern Canada together with the low-pressure system south of Resolute Bay contributed to

515   aerosol composition in the summertime Arctic FT. However, Figure 16 further demonstrates that sulfate, nitrate, ammonium,
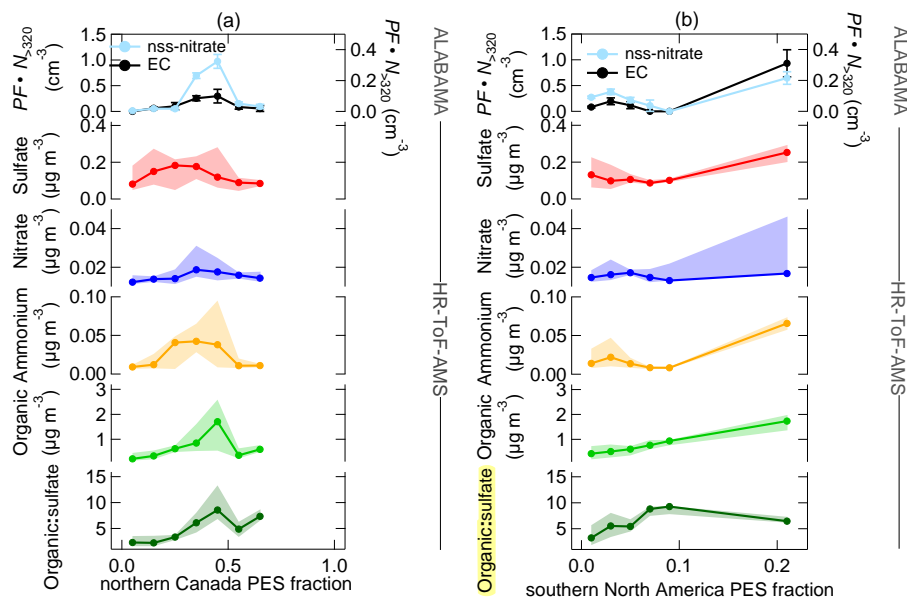
27

Figure 17. Aerosol composition measured by the ALABAMA and by the HR-ToF-AMS (indicated on the right side) as a function of FLEXPART derived PES fraction over (a) vegetation fires, (b) populated areas, and (c) industrial areas during the southern air mass period. Top panel represents the ALABAMA scaled number concentration ($PF \cdot N_{>320}$) with right axis referring to EC-containing (black) and left axis referring to nss-nitrate-containing (light blue) particles. Lower panels represent each median (solid line with marker) and interquartile ranges (shaded area) of the HR-ToF-AMS mass concentrations of sulfate (red), nitrate (blue), ammonium (orange), and organic matter (light green) as well as the organic-to-sulfate ratio (dark green) and the sulfate-to-organic ratio (pink). Uncertainty analyses are given in the Supplement Sect. 7.

and organic matter measured by the HR-ToF-AMS show decreasing concentrations with highest CO mixing ratios. Whereas the number fraction of nss-nitrate-containing particles and the organic-to-sulfate ratio (Fig. S22 and Fig. 16, respectively) were

28

Figure 18. Aerosol composition measured by the ALABAMA and by the HR-ToF-AMS (indicated on the right side) as a function of FLEXPART derived PES fraction over northern Canada (a) and southern North America (b) during the southern air mass period. Top panel represents each the ALABAMA scaled number concentration ($PF \cdot N_{>320}$) with right axis referring to EC-containing (black) and left axis referring to nss-nitrate-containing (light blue) particles. Lower panels represent each median (solid line with marker) and interquartile ranges (shaded area) of the HR-ToF-AMS mass concentrations of sulfate (red), nitrate (blue), ammonium (orange), organic matter (light green), and the organic-to-sulfate ratio (dark green). Uncertainty analyses are given in the Supplement Sect. 7.

increasing with high CO mixing ratios. Along with the low-pressure system, the transport of air masses that were characterized by high CO mixing ratios was accompanied with precipitation events, as can be seen in GFS archive data (Wetter3, 2020). It

520   is therefore conceivable that this transport pathway was linked to intensive particle wash-out events (Garrett et al., 2010, 2011; Matsui et al., 2011a; Browse et al., 2012; Sato et al., 2016).

Earlier measurements show that background concentrations of ammonium and nitrate are generally low in Arctic summer (Quinn et al., 2002; Kuhn et al., 2010; Chang et al., 2011; Schmale et al., 2011; Quennehen et al., 2011; Hamacher-Barth et al., 2016; Lange et al., 2018), which we can confirm under the pristine conditions during the Arctic air mass period (Fig. 10). How-

525   ever, our vertical profile measurements during the southern air mass period (Fig. 15) show that episodic and localized transport of vegetation fire emissions can perturb background concentrations of nitrate, ammonium, and organic matter. This finding is in line with modeling and observational studies (Hecobian et al., 2011; Brock et al., 2011; Lathem et al., 2013; Kondo et al., 2011; Matsui et al., 2011a; Breider et al., 2014), reporting on the response of nitrate, ammonium, and organic concentrations in the Arctic on the transport of large fire emissions from sub-Arctic regions. Also gas-phase measurements demonstrate the

530   large input of ammonia (precursor gas of particulate ammonium) by vegetation fire emissions to the summertime Arctic lower troposphere (Lutsch et al., 2016).

The mass concentration of rBC measured by the SP2 (during three out of five flights) provides evidence that those vegetation fires contributed also to the presence of rBC in the summertime Arctic FT (see Fig. S15). This result is in line with earlier studies, analyzing the source attribution of BC (or EC) in the summertime Arctic and suggesting a dominant influence of biomass

535   burning on the BC (or EC) burden in summer (e.g., Hirdman et al., 2010; Bourgeois and Bey, 2011; Stohl et al., 2013; Breider et al., 2014; Xu et al., 2017; Sobhani et al., 2018; Winiger et al., 2019; Zhu et al., 2020). In contrast, the ALABAMA analysis shows no significant evidence of influences from vegetation fires on the abundance of EC particles, which might be explained by the following reasons. It is known from previous field studies that chemically aged BC particles from vegetation fires are thickly coated with organics and inorganics (e.g., Paris et al., 2009; Singh et al., 2010; Kondo et al., 2011; Brock et al., 2011).

540   In addition, a laboratory study by Silva et al. (1999) reported the majority of biomass burning particles to include potassium. Given that potassium is known to produce matrix effects, owing to its low ionization potential (e.g., Silva and Prather, 2000), positive ion signals, other than K^+, in biomass burning particle spectra are likely suppressed by the presence of potassium. Further, Moffet and Prather (2009) reported negative ion mass spectra of aged soot to be dominated by nitrate and sulfate signals. Together, it is likely that signals of carbon cluster ions, indicative for the presence of EC/soot, are suppressed by other

545   substances that are abundant in biomass burning particles. This hypothesis is consistent with previous SPMS measurements during field experiments at southern latitudes, characterizing biomass burning aerosol (e.g., Pratt et al., 2011; Zauscher et al., 2013; Gunsch et al., 2018). These earlier studies show that mean mass spectra of aged biomass burning particles are generally characterized by the concurrent presence of potassium, sulfate, nitrate, organic acids, and nitrogen-containing organics, confirming findings in our study (see nss-nitrate in Figs. 6c and 17a).

550   Besides the influence of vegetation fires, the presence of sulfate, ammonium, nitrate, EC, and organic matter in the summertime Arctic FT can further be linked to anthropogenic emissions from southern latitudes. Air mass history illustrates the coincidence of enhanced sulfate, ammonium, nitrate, and organic concentrations with time spent over populated and/or industrial areas (Fig. 17b-c). In addition, those species were predominantly abundant when the residence time prior to sampling was high in southern North America (Fig. 18b). Along with this, highest sulfate concentrations were observed at maximum PES fraction over

555   anthropogenic sources compared to over vegetation fires (Fig. 17). Consistently, it has previously been shown that the sulfate burden in the summertime Arctic FT is dominated by transport of a wide variety of anthropogenic emissions in northern Eurasia, North America, and East Asia (e.g., Shindell et al., 2008; Hirdman et al., 2010; Kuhn et al., 2010; Bourgeois and Bey, 2011; Schmale et al., 2011; Matsui et al., 2011a; Breider et al., 2014; Yang et al., 2018; Sobhani et al., 2018). Interestingly, we could not observe a significant trend for the sulfate-to-organic ratio as a function of anthropogenic sources (Fig. 17b-c),

560   indicating the importance of anthropogenic emissions on the organic fraction in the Arctic FT.

The ALABAMA data further show that the presence of EC particles in the Arctic FT can partly be associated with industrial emissions in southern North America (compare Figs. 17c and 18b), likely including flaring emissions (compare Fig. S34 with Fig. 4b-c). Figure S34 illustrates that long range transport from southern North America to Arctic regions might be accompanied by emissions from oil production industry in Alberta, Canada (compare with Fig. 4c). This result is consistent with

565   recent modeling studies, demonstrating the importance of anthropogenic BC sources in northern Eurasia and North America (e.g., Huang et al., 2010; Bourgeois and Bey, 2011; Sobhani et al., 2018). Particularly, studies by Stohl et al. (2013) and

Evangeliou et al. (2018) demonstrated the importance of distant sources in southern North America to affect the abundance of EC-containing particles in the Arctic summer. The authors showed that regions in western Canada (Alberta), operating numerous oil producing facilities, influenced aerosol particle composition in the Arctic summer. However, contributions from sources in South Asia cannot be confirmed by our measurements, which might be related to maximum sampling altitude up to 3.5 km that is less sensitive to Asian pollution sources (e.g., Bourgeois and Bey, 2011; Sharma et al., 2013; Sobhani et al., 2018). Finally, nss-nitrate- and EC-containing particles were larger in diameter compared to BL particles, such as TMA-containing particles (Fig. S11), consistent with pronounced influences of aerosol processing during long range transport. Taken together, summertime Arctic FT aerosol particle composition under the influence of a prevailing low-pressure system was driven by the transport of emissions from vegetation fires and anthropogenic sources in northern Canada and southern North America.

4 Conclusions

Motivated by the limited knowledge of summertime Arctic aerosol, our study aimed to improve our understanding of sources impacting the vertical structure of aerosol particle chemical composition and mixing state. Aircraft-based measurements were performed using two complementary aerosol mass spectrometers, the ALABAMA and HR-ToF-AMS, and an SP2 in the summertime Canadian Arctic lower troposphere.

Our measurements and air mass trajectory analysis show that the vertical structure of aerosol particle composition in the summertime Arctic lower troposphere was driven by a combination of aerosol processes occurring along northward transport pathways and within Arctic regions. In our prior studies, we could show that particle composition in the isolated and stable stratified boundary layer was characterized by the abundance of MSA, sodium, chloride, and organic matter that is partly associated with particulate TMA (Willis et al., 2016, 2017; Köllner et al., 2017). Further, we observed that TMA and sea spray particles were externally mixed and smaller in diameter, suggesting a role of marine-derived secondary organic aerosol formation occurring alongside with primary sea-to-air emissions. Here, the presented results confirm the marine source of TMA by our FLEXPART air mass history analysis. The presence of TMA-containing particles correlated, similar to sea spray particles, with time spent over Arctic open water regions. Overall, this study together with findings from earlier work on the NETCARE 2014 measurements emphasize the importance of marine SOA formation on the vertical structure of particle composition in the summertime Arctic (Willis et al., 2016, 2017; Köllner et al., 2017; Croft et al., 2019).

As new results compared to our prior studies, we discussed particle composition and mixing state measured during two distinctive synoptic situations in the summertime Arctic lower FT, namely the Arctic and the southern air mass periods. In contrast to the isolated Arctic BL, particle composition aloft was characterized by the presence of nss-nitrate, EC, ammonium, sulfate, and oxidized organics that can partly be attributed to DCA transported over long distances from mid-latitude sources. However, particle composition in the FT varied with the synoptic situations, owing to different particle sources and transport pathways. Comparing both periods, the organic, ammonium, and nitrate concentrations measured by HR-ToF-AMS as well as the nitrate fraction by the ALABAMA were higher during the southern air mass period, reflecting the pronounced influence of vegetation fires in northern Canada during this time and of transport associated with the prevailing low-pressure system. Our air mass his-

tory analysis showed that elevated concentrations of nitrate, ammonium, rBC, and organic matter occurred when the residence time over vegetation fires in northern Canada was high. Further, those particles were largely present in air masses with high CO mixing ratios. Also the organic-to-sulfate ratio coincided with time the air mass spent over these fires.

Besides the influence of vegetation fires, anthropogenic sources in Europe, North America, and East Asia contributed to the presence of particles containing sulfate, nitrate, EC, organic matter, and ammonium in the summertime Arctic FT. The presence of those particles correlated with time spent over populated and industrial areas in Europe, East Asia, and southern North America. Measurements of enhanced EC concentrations can be traced back to oil production industry, including flaring, in Alberta (Canada), by means of the FLEXPART analysis. We further have evidence that EC and nss-nitrate particles present in the Arctic FT were exposed to chemical aging processes during northward transport. First, the size distributions of these particle types are shifted towards larger diameters compared to BL particles, such as TMA-containing particles. Second, these particles types were largely internally mixed with secondary substances, such as sulfate, nitrate, and oxygen-containing organic matter.

Particularly during the first period, our analysis showed that the majority of DCA-containing particles were observed in the Arctic FT and in air masses that spent significant time outside Arctic regions. Long range transport of aerosol and precursors from distant sources thus influenced the abundance of DCA particles in the summertime Arctic FT. These findings add to our understanding of organic acids in summer Arctic aerosol, because previous studies were confined to ground-based and shipborne datasets. Combined with the stable stratified nature of the Arctic lower troposphere, previous BL datasets were therefore less sensitive to organic acids from long range transport and related processes.

Together, these results indicate the important role of mid-latitude aerosol sources on summertime Arctic particle composition in the lower FT. Particularly, contributions from biomass burning emissions on summertime Arctic aerosol are likely to increase under scenarios for the future climate (e.g., Randerson et al., 2006; de Groot et al., 2013; Marelle et al., 2018; Evangeliou et al., 2019). To our knowledge, this is the first study providing vertically resolved particle chemical composition analysis in the summertime Arctic FT, by using two complementary aerosol mass spectrometers with black carbon measurements from an SP2. However, open questions remain, partly owing to limitations of the current study. Being limited by the spatial and temporal range of the NETCARE 2014 measurements, it is difficult to assess the representativeness of the findings for the whole Arctic. Future widespread and long-term measurements would help to extend the results to other Arctic regions and seasons. Lagrangian flight experiments would help to better constrain the relative role of aerosol processing, including wet removal and photochemical aging, on summertime Arctic particle composition. Based on limitations in sampling altitude, future Arctic airborne measurements in the mid to upper troposphere are necessary to further characterize the impact of mid-latitude pollution sources on summertime Arctic aerosol properties. Finally, it is of relevance to further characterize organic compounds in Arctic aerosol along with their sources, formation processes, and impact on clouds.

Author contributions. JA, RL, and AH designed the research project. FK, JS, HB, RL, MW, and JB carried out the measurements. AA
635   processed the AIMMS-20 data. TK, FH, and JS re-designed and further developed the ALABAMA for aircraft-based measurements. DK provided the FLEXPART output. MW provided the HR-ToF-AMS data. HS provided the SP2 and UHSAS data. HB provided the CO data. FK performed the data analyses with critical feedback from JS, PH, MW, TK, DK, and JA. FK wrote the manuscript. The manuscript was critically reviewed by JS, PH, SB, JA, MW, RL, DK, and HS.

Competing interests. The authors declare that they have no conflict of interest.

References

Abbatt, J., Broekhuizen, K., and Pradeep Kumar, P.: Cloud condensation nucleus activity of internally mixed ammonium sulfate/organic acid aerosol particles, Atmospheric Environment, 39, 4767 – 4778, https://doi.org/https://doi.org/10.1016/j.atmosenv.2005.04.029, http://www.sciencedirect.com/science/article/pii/S1352231005004115, 2005.

Abbatt, J. P. D., Leaitch, W. R., Aliabadi, A. A., Bertram, A. K., Blanchet, J.-P., Boivin-Rioux, A., Bozem, H., Burkart, J., Chang, R. Y. W., Charette, J., Chaubey, J. P., Christensen, R. J., Cirisan, A., Collins, D. B., Croft, B., Dionne, J., Evans, G. J., Fletcher, C. G., Galí, M., Ghahremaninezhad, R., Girard, E., Gong, W., Gosselin, M., Gourdal, M., Hanna, S. J., Hayashida, H., Herber, A. B., Hesaraki, S., Hoor, P., Huang, L., Hussherr, R., Irish, V. E., Keita, S. A., Kodros, J. K., Köllner, F., Kolonjari, F., Kunkel, D., Ladino, L. A., Law, K., Levasseur, M., Libois, Q., Liggio, J., Lizotte, M., Macdonald, K. M., Mahmood, R., Martin, R. V., Mason, R. H., Miller, L. A., Moravek, A., Mortenson, E., Mungall, E. L., Murphy, J. G., Namazi, M., Norman, A.-L., O'Neill, N. T., Pierce, J. R., Russell, L. M., Schneider, J., Schulz, H., Sharma, S., Si, M., Staebler, R. M., Steiner, N. S., Thomas, J. L., von Salzen, K., Wentzell, J. J. B., Willis, M. D., Wentworth, G. R., Xu, J.-W., and Yakobi-Hancock, J. D.: Overview paper: New insights into aerosol and climate in the Arctic, Atmos. Chem. Phys., 19, 2527–2560, https://doi.org/10.5194/acp-19-2527-2019, 2019.

Acosta Navarro, J. C., Varma, V., Riipinen, I., Seland, Ø., Kirkevåg, A., Struthers, H., Iversen, T., Hansson, H.-C., and Ekman, A. M. L.: Amplification of Arctic warming by past air pollution reductions in Europe, Nature Geoscience, 9, 277–281, http://dx.doi.org/10.1038/ngeo2673, 2016.

Aero-Laser GmbH: Ultra-Fast Carbon-Monoxide Analyser AL5002-Manual-Version 1.24, Aero-Laser GmbH, 2013.

Aliabadi, A. A., Staebler, R. M., and Sharma, S.: Air quality monitoring in communities of the Canadian Arctic during the high shipping season with a focus on local and marine pollution, Atmos. Chem. Phys., 15, 2651–2673, https://doi.org/10.5194/acp-15-2651-2015, 2015.

Aliabadi, A. A., Staebler, R., Liu, M., and Herber, A.: Characterization and Parametrization of Reynolds Stress and Turbulent Heat Flux in the Stably-Stratified Lower Arctic Troposphere Using Aircraft Measurements, Bound.-Lay. Meteorol., pp. 1–28, https://doi.org/10.1007/s10546-016-0164-7, 2016a.

Aliabadi, A. A., Thomas, J. L., Herber, A. B., Staebler, R. M., Leaitch, W. R., Schulz, H., Law, K. S., Marelle, L., Burkart, J., Willis, M. D., Bozem, H., Hoor, P. M., Köllner, F., Schneider, J., Levasseur, M., and Abbatt, J. P. D.: Ship emissions measurement in the Arctic by plume intercepts of the Canadian Coast Guard icebreaker *Amundsen* from the *Polar 6* aircraft platform, Atmos. Chem. Phys., 16, 7899–7916, https://doi.org/10.5194/acp-16-7899-2016, 2016b.

AMAP: Assessment 2007: Oil and Gas Activities in the Arctic - Effects and Potential Effects, Arctic Monitoring and Assessment Programme (AMAP), Oslo, Norway, 2, vii + 277, 2010.

Andreae, M. O. and Merlet, P.: Emission of trace gases and aerosols from biomass burning, Global Biogeochem. Cy., 15, 955–966, https://doi.org/10.1029/2000GB001382, 2001.

Angelino, S., Suess, D. T., and Prather, K. A.: Formation of Aerosol Particles from Reactions of Secondary and Tertiary Alkylamines: Characterization by Aerosol Time-of-Flight Mass Spectrometry, Environ. Sci. Technol., 35(15), 3130–3138, https://doi.org/10.1021/es0015444, 2001.

Arnold, S., Law, K., Brock, C., Thomas, J., Starkweather, S., Von Salzen, K., Stohl, A., Sharma, S., Lund, M., Flanner, M., Petäjä, T., Tanimoto, H., Gamble, J., Dibb, J., Melamed, M., Johnson, N., Fidel, M., Tynkkynen, V., Baklanov, A., Eckhardt, S., Monks, S., Browse, J., and Bozem, H.: Arctic air pollution: Challenges and opportunities for the next decade, Elementa, 2016, https://doi.org/10.12952/journal.elementa.000104, 2016.

695 Aventech: www.aventech.com/products/aimms20.html, last access: 25.05.2018, 2018.

Baccarini, A., Karlsson, L., Dommen, J., Duplessis, P., Vüllers, J., Brooks, I. M., Saiz-Lopez, A., Salter, M., Tjernström, M., Baltensperger, U., Zieger, P., and Schmale, J.: Frequent new particle formation over the high Arctic pack ice by enhanced iodine emissions, Nature Communications, 11, 4924, https://doi.org/10.1038/s41467-020-18551-0, https://doi.org/10.1038/s41467-020-18551-0, 2020.

Bond, T. C., Habib, G., and Bergstrom, R. W.: Limitations in the enhancement of visible light absorption due to mixing state, Journal
700 of Geophysical Research: Atmospheres, 111, https://doi.org/https://doi.org/10.1029/2006JD007315, https://agupubs.onlinelibrary.wiley. com/doi/abs/10.1029/2006JD007315, 2006.

Boucher, O., Randall, D., Artaxo, P., Bretherton, C., Feingold, G., Forster, P., Kerminen, V.-M., Kondo, Y., Liao, H., Lohmann, U., Rasch, P., Satheesh, S., Sherwood, S., Stevens, B., and Zhang, X.: Climate Change 2013: The Physical Science Basis. Contribution of Working Group I to the Fifth Assessment Report of the Intergovernmental Panel on Climate Change, chap. Clouds and Aerosols, pp. 571–658,
705 Cambridge University Press, https://doi.org/DOI: 10.1017/CBO9781107415324.016, 2013.

Bourgeois, Q. and Bey, I.: Pollution transport efficiency toward the Arctic: Sensitivity to aerosol scavenging and source regions, J. Geophys. Res.-Atmos., 116, https://doi.org/10.1029/2010JD015096, 2011.

Bozem, H., Hoor, P., Kunkel, D., Köllner, F., Schneider, J., Herber, A., Schulz, H., Leaitch, W. R., Aliabadi, A. A., Willis, M. D., Burkart, J., and Abbatt, J. P. D.: Characterization of Transport Regimes and the Polar Dome during Arctic Spring and Summer using in-situ Aircraft
710 Measurements, Atmos. Chem. Phys. Discuss., 2019, 1–36, https://doi.org/10.5194/acp-2019-70, 2019.

Brands, M.: Aufbau und Charakterisierung eines fugzeuggetragenen Einzel-partikel-Massenspektrometers, Ph.D. thesis, Johannes-Gutenberg Universität Mainz, 2009.

Brands, M., Kamphus, M., Böttger, T., Schneider, J., Drewnick, F., Roth, A., Curtius, J., Voigt, C., Borbon, A., Beekmann, M., Bourdon, A., Perrin, T., and Borrmann, S.: Characterization of a Newly Developed Aircraft-Based Laser Ablation Aerosol Mass Spectrometer
715 (ALABAMA) and First Field Deployment in Urban Pollution Plumes over Paris During MEGAPOLI 2009, Aerosol Sci. Technol., 45, 46–64, https://doi.org/10.1080/02786826.2010.517813, 2011.

Breider, T. J., Mickley, L. J., Jacob, D. J., Wang, Q., Fisher, J. A., Chang, R. Y.-W., and Alexander, B.: Annual distributions and sources of Arctic aerosol components, aerosol optical depth, and aerosol absorption, J. Geophys. Res.-Atmos., 119, 4107–4124, https://doi.org/10.1002/2013JD020996, 2014.

720 Breider, T. J., Mickley, L. J., Jacob, D. J., Ge, C., Wang, J., Payer Sulprizio, M., Croft, B., Ridley, D. A., McConnell, J. R., Sharma, S., Husain, L., Dutkiewicz, V. A., Eleftheriadis, K., Skov, H., and Hopke, P. K.: Multidecadal trends in aerosol radiative forcing over the Arctic: Contribution of changes in anthropogenic aerosol to Arctic warming since 1980, J. Geophys. Res.-Atmos., 122, 3573–3594, https://doi.org/10.1002/2016JD025321, 2017.

Brock, C. A., Radke, L. F., Lyons, J. H., and Hobbs, P. V.: Arctic hazes in summer over Greenland and the North American Arctic. I: Incidence
725 and origins, Journal of Atmospheric Chemistry, 9, 129–148, https://doi.org/10.1007/BF00052828, https://doi.org/10.1007/BF00052828, 1989.

Brock, C. A., Cozic, J., Bahreini, R., Froyd, K. D., Middlebrook, A. M., McComiskey, A., Brioude, J., Cooper, O. R., Stohl, A., Aikin, K. C., de Gouw, J. A., Fahey, D. W., Ferrare, R. A., Gao, R.-S., Gore, W., Holloway, J. S., Hübler, G., Jefferson, A., Lack, D. A., Lance, S., Moore, R. H., Murphy, D. M., Nenes, A., Novelli, P. C., Nowak, J. B., Ogren, J. A., Peischl, J., Pierce, R. B., Pilewskie, P.,
730 Quinn, P. K., Ryerson, T. B., Schmidt, K. S., Schwarz, J. P., Sodemann, H., Spackman, J. R., Stark, H., Thomson, D. S., Thornberry, T., Veres, P., Watts, L. A., Warneke, C., and Wollny, A. G.: Characteristics, sources, and transport of aerosols measured in spring 2008

35

during the aerosol, radiation, and cloud processes affecting Arctic Climate (ARCPAC) Project, Atmos. Chem. Phys., 11, 2423–2453, https://doi.org/10.5194/acp-11-2423-2011, 2011.

Browse, J., Carslaw, K. S., Arnold, S. R., Pringle, K., and Boucher, O.: The scavenging processes controlling the seasonal cycle in Arctic sulphate and black carbon aerosol, Atmos. Chem. Phys., 12, 6775–6798, https://doi.org/10.5194/acp-12-6775-2012, 2012.

Burkart, J., Willis, M. D., Bozem, H., Thomas, J. L., Law, K., Hoor, P., Aliabadi, A. A., Köllner, F., Schneider, J., Herber, A., Abbatt, J. P. D., and Leaitch, W. R.: Summertime observations of elevated levels of ultrafine particles in the high Arctic marine boundary layer, Atmos. Chem. Phys., 17, 5515–5535, https://doi.org/10.5194/acp-17-5515-2017, 2017.

Cai, Y., Montague, D. C., Mooiweer-Bryan, W., and Deshler, T.: Performance characteristics of the ultra high sensitivity aerosol spectrometer for particles between 55 and 800 nm: Laboratory and field studies, J. Aerosol Sci., 39, 759 – 769, https://doi.org/10.1016/j.jaerosci.2008.04.007, 2008.

Cavalieri, D. J., Parkinson, C. L., Gloersen, P., and Zwally, H. J.: Sea Ice Concentrations from Nimbus-7 SMMR and DMSP SSM/I-SSMIS Passive Microwave Data, Version 1, NSIDC-0051, Boulder, Colorado USA. NASA National Snow and Ice Data Center Distributed Active Archive Center, https://doi.org/https://doi.org/10.5067/8GQ8LZQVL0VL, last access: 08.06.2018, 1996, updated yearly.

Chang, R.-W., Liu, P., Leaitch, W., and Abbatt, J.: Comparison between measured and predicted CCN concentrations at Egbert, Ontario: Focus on the organic aerosol fraction at a semi-rural site, Atmospheric Environment, 41, 8172 – 8182, https://doi.org/https://doi.org/10.1016/j.atmosenv.2007.06.039, http://www.sciencedirect.com/science/article/pii/S1352231007005948, 2007.

Chang, R. Y.-W., Slowik, J. G., Shantz, N. C., Vlasenko, A., Liggio, J., Sjostedt, S. J., Leaitch, W. R., and Abbatt, J. P. D.: The hygroscopicity parameter (κ) of ambient organic aerosol at a field site subject to biogenic and anthropogenic influences: relationship to degree of aerosol oxidation, Atmospheric Chemistry and Physics, 10, 5047–5064, https://doi.org/10.5194/acp-10-5047-2010, https://acp.copernicus.org/articles/10/5047/2010/, 2010.

Chang, R. Y.-W., Leck, C., Graus, M., Müller, M., Paatero, J., Burkhart, J. F., Stohl, A., Orr, L. H., Hayden, K., Li, S.-M., Hansel, A., Tjernström, M., Leaitch, W. R., and Abbatt, J. P. D.: Aerosol composition and sources in the central Arctic Ocean during ASCOS, Atmos. Chem. Phys., 11, 10 619–10 636, https://doi.org/10.5194/acp-11-10619-2011, 2011.

Coopman, Q., Garrett, T. J., Finch, D. P., and Riedi, J.: High Sensitivity of Arctic Liquid Clouds to Long-Range Anthropogenic Aerosol Transport, Geophysical Research Letters, 45, 372–381, https://doi.org/https://doi.org/10.1002/2017GL075795, https://agupubs.onlinelibrary.wiley.com/doi/abs/10.1002/2017GL075795, 2018.

Creamean, J. M., Maahn, M., de Boer, G., McComiskey, A., Sedlacek, A. J., and Feng, Y.: The influence of local oil exploration and regional wildfires on summer 2015 aerosol over the North Slope of Alaska, Atmos. Chem. Phys., 18, 555–570, https://doi.org/10.5194/acp-18-555-2018, 2018.

Croft, B., Martin, R. V., Leaitch, W. R., Burkart, J., Chang, R. Y.-W., Collins, D. B., Hayes, P. L., Hodshire, A. L., Huang, L., Kodros, J. K., Moravek, A., Mungall, E. L., Murphy, J. G., Sharma, S., Tremblay, S., Wentworth, G. R., Willis, M. D., Abbatt, J. P. D., and Pierce, J. R.: Arctic marine secondary organic aerosol contributes significantly to summertime particle size distributions in the Canadian Arctic Archipela-go, Atmos. Chem. Phys., 2019, 2787–2812, https://doi.org/10.5194/acp-19-2787-2019, 2019.

Curry, J. A., Schramm, J. L., and Ebert, E. E.: Sea Ice-Albedo Climate Feedback Mechanism, J. Climate, 8, 240–247, https://doi.org/10.1175/1520-0442(1995)008<0240:SIACFM>2.0.CO;2, 1995.

Dall'Osto, M., Beddows, D. C. S., Tunved, P., Krejci, R., Ström, J., Hansson, H.-C., Yoon, Y. J., Park, K.-T., Becagli, S., Udisti, R., Onasch, T., O'Dowd, C. D., Simó, R., and Harrison, R. M.: Arctic sea ice melt leads to atmospheric new particle formation, Scientific Reports, 7, https://doi.org/10.1038/s41598-017-03328-1, 2017.

de Groot, W. J., Flannigan, M. D., and Cantin, A. S.: Climate change impacts on future boreal fire regimes, Forest Ecology and Management, 294, 35–44, https://doi.org/10.1016/j.foreco.2012.09.027, 2013.

DeCarlo, P. F., Kimmel, J. R., Trimborn, A., Northway, M. J., Jayne, J. T., Aiken, A. C., Gonin, M., Fuhrer, K., Horvath, T., Docherty, K. S., Worsnop, D. R., and Jimenez, J. L.: Field-Deployable, High-Resolution, Time-of-Flight Aerosol Mass Spectrometer, Anal. Chem., 78, 8281–8289, https://doi.org/10.1021/ac061249n, 2006.

Dusek, U., Frank, G. P., Hildebrandt, L., Curtius, J., Schneider, J., Walter, S., Chand, D., Drewnick, F., Hings, S., Jung, D., Borrmann, S., and Andreae, M. O.: Size Matters More Than Chemistry for Cloud-Nucleating Ability of Aerosol Particles, Science, 312, 1375–1378, https://doi.org/10.1126/science.1125261, https://science.sciencemag.org/content/312/5778/1375, 2006.

Eckhardt, S., Hermansen, O., Grythe, H., Fiebig, M., Stebel, K., Cassiani, M., Baecklund, A., and Stohl, A.: The influence of cruise ship emissions on air pollution in Svalbard - a harbinger of a more polluted Arctic?, Atmos. Chem. Phys., 13, 8401–8409, https://doi.org/10.5194/acp-13-8401-2013, 2013.

Eckhardt, S., Quennehen, B., Olivié, D. J. L., Berntsen, T. K., Cherian, R., Christensen, J. H., Collins, W., Crepinsek, S., Daskalakis, N., Flanner, M., Herber, A., Heyes, C., Hodnebrog, Ø., Huang, L., Kanakidou, M., Klimont, Z., Langner, J., Law, K. S., Lund, M. T., Mahmood, R., Massling, A., Myriokefalitakis, S., Nielsen, I. E., Nøjgaard, J. K., Quaas, J., Quinn, P. K., Raut, J.-C., Rumbold, S. T., Schulz, M., Sharma, S., Skeie, R. B., Skov, H., Uttal, T., von Salzen, K., and Stohl, A.: Current model capabilities for simulating black carbon and sulfate concentrations in the Arctic atmosphere: a multi-model evaluation using a comprehensive measurement data set, Atmospheric Chemistry and Physics, 15, 9413–9433, https://doi.org/10.5194/acp-15-9413-2015, https://acp.copernicus.org/articles/15/9413/2015/, 2015.

Elvidge, C. D., Zhizhin, M., Hsu, F.-C., and Baugh, K. E.: VIIRS Nightfire: Satellite Pyrometry at Night, Remote Sensing, 5, 4423–4449, https://doi.org/10.3390/rs5094423, 2013.

Elvidge, C. D., Zhizhin, M., Baugh, K., Hsu, F.-C., and Ghosh, T.: Methods for Global Survey of Natural Gas Flaring from Visible Infrared Imaging Radiometer Suite Data, Energies, 9, https://doi.org/10.3390/en9010014, 2016.

Ervens, B., Feingold, G., Clegg, S. L., and Kreidenweis, S. M.: A modeling study of aqueous production of dicarboxylic acids: 2. Implications for cloud microphysics, Journal of Geophysical Research: Atmospheres, 109, https://doi.org/https://doi.org/10.1029/2004JD004575, https://agupubs.onlinelibrary.wiley.com/doi/abs/10.1029/2004JD004575, 2004.

Evangeliou, N., Thompson, R. L., Eckhardt, S., and Stohl, A.: Top-down estimates of black carbon emissions at high latitudes using an atmospheric transport model and a Bayesian inversion framework, Atmos. Chem. Phys., 18, 15 307–15 327, https://doi.org/10.5194/acp-18-15307-2018, 2018.

Evangeliou, N., Kylling, A., Eckhardt, S., Myroniuk, V., Stebel, K., Paugam, R., Zibtsev, S., and Stohl, A.: Open fires in Greenland in summer 2017: transport, deposition and radiative effects of BC, OC and BrC emissions, Atmos. Chem. Phys., 19, 1393–1411, https://doi.org/10.5194/acp-19-1393-2019, 2019.

Ferrero, L., Cappelletti, D., Busetto, M., Mazzola, M., Lupi, A., Lanconelli, C., Becagli, S., Traversi, R., Caiazzo, L., Giardi, F., Moroni, B., Crocchianti, S., Fierz, M., Močnik, G., Sangiorgi, G., Perrone, M. G., Maturilli, M., Vitale, V., Udisti, R., and Bolzacchini, E.: Vertical profiles of aerosol and black carbon in the Arctic: a seasonal phenomenology along 2 years (2011–2012) of field campaigns, Atmos. Chem. Phys., 16, 12 601–12 629, https://doi.org/10.5194/acp-16-12601-2016, 2016.

Flanner, M. G.: Arctic climate sensitivity to local black carbon, J. Geophys. Res.-Atmos., 118, 1840–1851, https://doi.org/10.1002/jgrd.50176, 2013.

Flanner, M. G., Shell, K. M., Barlage, M., Perovich, D. K., and Tschudi, M. A.: Radiative forcing and albedo feedback from the Northern Hemisphere cryosphere between 1979 and 2008, Nature Geoscience, 4, 151–155, https://doi.org/10.1038/ngeo1062, 2011.

810 Froyd, K. D., Murphy, D. M., Brock, C. A., Campuzano-Jost, P., Dibb, J. E., Jimenez, J.-L., Kupc, A., Middlebrook, A. M., Schill, G. P., Thornhill, K. L., Williamson, C. J., Wilson, J. C., and Ziemba, L. D.: A new method to quantify mineral dust and other aerosol species from aircraft platforms using single-particle mass spectrometry, Atmospheric Measurement Techniques, 12, 6209–6239, https://doi.org/10.5194/amt-12-6209-2019, https://www.atmos-meas-tech.net/12/6209/2019/, 2019.

Fu, P., Kawamura, K., Chen, J., and Barrie, L. A.: Isoprene, Monoterpene, and Sesquiterpene Oxidation Products in the High Arctic Aerosols
815 during Late Winter to Early Summer, Environ. Sci. Technol., 43, 4022–4028, https://doi.org/10.1021/es803669a, 2009.

Fu, P., Kawamura, K., Usukura, K., and Miura, K.: Dicarboxylic acids, ketocarboxylic acids and glyoxal in the marine aerosols collected during a round-the-world cruise, Mar. Chem., 148, 22 – 32, https://doi.org/10.1016/j.marchem.2012.11.002, 2013.

Fuelberg, H. E., Harrigan, D. L., and Sessions, W.: A meteorological overview of the ARCTAS 2008 mission, Atmos. Chem. Phys., 10, 817–842, https://doi.org/10.5194/acp-10-817-2010, 2010.

820 Furutani, H., Dall'osto, M., Roberts, G. C., and Prather, K. A.: Assessment of the relative importance of atmospheric aging on CCN activity derived from field observations, Atmospheric Environment, 42, 3130 – 3142, https://doi.org/https://doi.org/10.1016/j.atmosenv.2007.09.024, http://www.sciencedirect.com/science/article/pii/S1352231007008084, 2008.

Gao, R. S., Schwarz, J. P., Kelly, K. K., Fahey, D. W., Watts, L. A., Thompson, T. L., Spackman, J. R., Slowik, J. G., Cross, E. S., Han, J.-H.,
825 Davidovits, P., Onasch, T. B., and Worsnop, D. R.: A Novel Method for Estimating Light-Scattering Properties of Soot Aerosols Using a Modified Single-Particle Soot Photometer, Aerosol Sci. Technol., 41, 125–135, https://doi.org/10.1080/02786820601118398, 2007.

Garrett, T., Zhao, C., and Novelli, P.: Assessing the relative contributions of transport efficiency and scavenging to seasonal variability in Arctic aerosol, Tellus B, 62, 190–196, https://doi.org/10.1111/j.1600-0889.2010.00453.x, 2010.

Garrett, T. J., Brattström, S., Sharma, S., Worthy, D. E. J., and Novelli, P.: The role of scavenging in the seasonal transport of black carbon
830 and sulfate to the Arctic, Geophysical Research Letters, 38, https://doi.org/10.1029/2011GL048221, https://agupubs.onlinelibrary.wiley.com/doi/abs/10.1029/2011GL048221, 2011.

Giebl, H., Berner, A., Reischl, G., Puxbaum, H., Kasper-Giebl, A., and Hitzenberger, R.: CCN activation of oxalic and malonic acid test aerosols with the University of Vienna cloud condensation nuclei counter, Journal of Aerosol Science, 33, 1623 – 1634, https://doi.org/https://doi.org/10.1016/S0021-8502(02)00115-5, http://www.sciencedirect.com/science/article/pii/S0021850202001155, 2002.
835

Guasco, T. L., Cuadra-Rodriguez, L. A., Pedler, B. E., Ault, A. P., Collins, D. B., Zhao, D., Kim, M. J., Ruppel, M. J., Wilson, S. C., Pomeroy, R. S., Grassian, V. H., Azam, F., Bertram, T. H., and Prather, K. A.: Transition Metal Associations with Primary Biological Particles in Sea Spray Aerosol Generated in a Wave Channel, Environ. Sci. Technol., 48, 1324–1333, https://doi.org/10.1021/es403203d, 2014.

Gunsch, M. J., Kirpes, R. M., Kolesar, K. R., Barrett, T. E., China, S., Sheesley, R. J., Laskin, A., Wiedensohler, A., Tuch, T., and Pratt,
840 K. A.: Contributions of transported Prudhoe Bay oil field emissions to the aerosol population in Utqiaġvik, Alaska, Atmos. Chem. Phys., 17, 10 879–10 892, https://doi.org/10.5194/acp-17-10879-2017, 2017.

Gunsch, M. J., May, N. W., Wen, M., Bottenus, C. L. H., Gardner, D. J., VanReken, T. M., Bertman, S. B., Hopke, P. K., Ault, A. P., and Pratt, K. A.: Ubiquitous influence of wildfire emissions and secondary organic aerosol on summertime atmospheric aerosol in the forested Great Lakes region, Atmos. Chem. Phys., 18, 3701–3715, https://doi.org/10.5194/acp-18-3701-2018, 2018.

845 Hamacher-Barth, E., Leck, C., and Jansson, K.: Size-resolved morphological properties of the high Arctic summer aerosol during ASCOS-2008, Atmos. Chem. Phys., 16, 6577–6593, https://doi.org/10.5194/acp-16-6577-2016, 2016.

Hansen, A. M. K., Kristensen, K., Nguyen, Q. T., Zare, A., Cozzi, F., Nøjgaard, J. K., Skov, H., Brandt, J., Christensen, J. H., Ström, J., Tunved, P., Krejci, R., and Glasius, M.: Organosulfates and organic acids in Arctic aerosols: speciation, annual variation and concentration levels, Atmos. Chem. Phys., 14, 7807–7823, https://doi.org/10.5194/acp-14-7807-2014, 2014.

850 Hansen, J. and Nazarenko, L.: Soot climate forcing via snow and ice albedos, Proceedings of the National Academy of Sciences, 101, 423–428, https://doi.org/10.1073/pnas.2237157100, https://www.pnas.org/content/101/2/423, 2004.

Haywood, J. and Boucher, O.: Estimates of the direct and indirect radiative forcing due to tropospheric aerosols: A review, Rev. Geophys., 38, 513–543, https://doi.org/10.1029/1999RG000078, 2000.

Healy, R. M., Sciare, J., Poulain, L., Crippa, M., Wiedensohler, A., Prévôt, A. S. H., Baltensperger, U., Sarda-Estève, R., McGuire, M. L., 855 Jeong, C.-H., McGillicuddy, E., O'Connor, I. P., Sodeau, J. R., Evans, G. J., and Wenger, J. C.: Quantitative determination of carbonaceous particle mixing state in Paris using single-particle mass spectrometer and aerosol mass spectrometer measurements, Atmos. Chem. Phys., 13, 9479–9496, https://doi.org/10.5194/acp-13-9479-2013, 2013.

Healy, R. M., Evans, G. J., Murphy, M., Sierau, B., Arndt, J., McGillicuddy, E., O'Connor, I. P., Sodeau, J. R., and Wenger, J. C.: Single-particle speciation of alkylamines in ambient aerosol at five European sites, Anal. Bioanal. Chem., 407, 5899–5909, 860 https://doi.org/10.1007/s00216-014-8092-1, 2015.

Hecobian, A., Liu, Z., Hennigan, C. J., Huey, L. G., Jimenez, J. L., Cubison, M. J., Vay, S., Diskin, G. S., Sachse, G. W., Wisthaler, A., Mikoviny, T., Weinheimer, A. J., Liao, J., Knapp, D. J., Wennberg, P. O., Kürten, A., Crounse, J. D., Clair, J. S., Wang, Y., and Weber, R. J.: Comparison of chemical characteristics of 495 biomass burning plumes intercepted by the NASA DC-8 aircraft during the ARCTAS/CARB-2008 field campaign, Atmos. Chem. Phys., 11, 13 325–13 337, https://doi.org/10.5194/acp-11-13325-2011, 2011.

865 Herber, A. B., Dethloff, K., Haas, C., Steinhage, D., Strapp, J. W., Bottenheim, J., McElroy, T., and Yamanouchi, T.: POLAR 5 - a new research aircraft for improved access to the Arctic, ISAR-1, Drastic Change under the Global Warming, Extended Abstract, 2008.

Hirdman, D., Sodemann, H., Eckhardt, S., Burkhart, J. F., Jefferson, A., Mefford, T., Quinn, P. K., Sharma, S., Ström, J., and Stohl, A.: Source identification of short-lived air pollutants in the Arctic using statistical analysis of measurement data and particle dispersion model output, Atmos. Chem. Phys., 10, 669–693, https://doi.org/10.5194/acp-10-669-2010, 2010.

870 Hoffmann, E. H., Tilgner, A., Schrödner, R., Bräuer, P., Wolke, R., and Herrmann, H.: An advanced modeling study on the impacts and atmospheric implications of multiphase dimethyl sulfide chemistry, Proceedings of the National Academy of Sciences, 113, 11 776–11 781, https://doi.org/10.1073/pnas.1606320113, https://www.pnas.org/content/113/42/11776, 2016.

Holland, M. M. and Bitz, C. M.: Polar amplification of climate change in coupled models, Climate Dyn., 21, 221–232, https://doi.org/10.1007/s00382-003-0332-6, 2003.

875 Huang, L., Gong, S. L., Jia, C. Q., and Lavoué, D.: Relative contributions of anthropogenic emissions to black carbon aerosol in the Arctic, J. Geophys. Res.-A, 115, https://doi.org/10.1029/2009JD013592, 2010.

Hudson, P. K., Murphy, D. M., Cziczo, D. J., Thomson, D. S., de Gouw, J. A., Warneke, C., Holloway, J., Jost, H.-J., and Hübler, G.: Biomass-burning particle measurements: Characteristic composition and chemical processing, J. Geophys. Res., 109, https://doi.org/10.1029/2003JD004398, 2004.

880 Intrieri, J. M., Fairall, C. W., Shupe, M. D., Persson, P. O. G., Andreas, E. L., Guest, P. S., and Moritz, R. E.: An annual cycle of Arctic surface cloud forcing at SHEBA, Journal of Geophysical Research: Oceans, 107, SHE 13–1–SHE 13–14, https://doi.org/https://doi.org/10.1029/2000JC000439, https://agupubs.onlinelibrary.wiley.com/doi/abs/10.1029/2000JC000439, 2002.

IPCC: Climate Change 2014: Synthesis Report. Contribution of Working Groups I, II and III to the Fifth Assessment Report of the Intergovernmental Panel on Climate Change [Core Writing Team, R.K. Pachauri and L.A. Meyer (eds.)]. IPCC, Geneva, Switzerland, 151 pp.,
885 2014.

IPCC: Summary for Policymakers. In: Global Warming of 1.5°C. An IPCC Special Report on the impacts of global warming of 1.5°C above pre-industrial levels and related global greenhouse gas emission pathways, in the context of strengthening the global response to the threat of climate change, sustainable development, and efforts to eradicate poverty [Masson-Delmotte, V., P. Zhai, H.-O. Pörtner, D. Roberts, J. Skea, P.R. Shukla, A. Pirani, W. Moufouma-Okia, C. Péan, R. Pidcock, S. Connors, J.B.R. Matthews, Y. Chen, X. Zhou, M.I. Gomis, E.
890 Lonnoy, T. Maycock, M. Tignor, and T. Waterfield (eds.)]. World Meteorological Organization, Geneva, Switzerland, 32 pp., 2018.

Jiao, C., Flanner, M. G., Balkanski, Y., Bauer, S. E., Bellouin, N., Berntsen, T. K., Bian, H., Carslaw, K. S., Chin, M., De Luca, N., Diehl, T., Ghan, S. J., Iversen, T., Kirkevåg, A., Koch, D., Liu, X., Mann, G. W., Penner, J. E., Pitari, G., Schulz, M., Seland, Ø., Skeie, R. B., Steenrod, S. D., Stier, P., Takemura, T., Tsigaridis, K., van Noije, T., Yun, Y., and Zhang, K.: An AeroCom assessment of black carbon in Arctic snow and sea ice, Atmospheric Chemistry and Physics, 14, 2399–2417, https://doi.org/10.5194/acp-14-2399-2014, https:
895 //acp.copernicus.org/articles/14/2399/2014/, 2014.

Jimenez, J. L., Canagaratna, M. R., Donahue, N. M., Prevot, A. S. H., Zhang, Q., Kroll, J. H., DeCarlo, P. F., Allan, J. D., Coe, H., Ng, N. L., Aiken, A. C., Docherty, K. S., Ulbrich, I. M., Grieshop, A. P., Robinson, A. L., Duplissy, J., Smith, J. D., Wilson, K. R., Lanz, V. A., Hueglin, C., Sun, Y. L., Tian, J., Laaksonen, A., Raatikainen, T., Rautiainen, J., Vaattovaara, P., Ehn, M., Kulmala, M., Tomlinson, J. M., Collins, D. R., Cubison, M. J., , Dunlea, J., Huffman, J. A., Onasch, T. B., Alfarra, M. R., Williams, P. I., Bower, K., Kondo,
900 Y., Schneider, J., Drewnick, F., Borrmann, S., Weimer, S., Demerjian, K., Salcedo, D., Cottrell, L., Griffin, R., Takami, A., Miyoshi, T., Hatakeyama, S., Shimono, A., Sun, J. Y., Zhang, Y. M., Dzepina, K., Kimmel, J. R., Sueper, D., Jayne, J. T., Herndon, S. C., Trimborn, A. M., Williams, L. R., Wood, E. C., Middlebrook, A. M., Kolb, C. E., Baltensperger, U., and Worsnop, D. R.: Evolution of Organic Aerosols in the Atmosphere, Science, 326, 1525–1529, https://doi.org/10.1126/science.1180353, 2009.

Junge, C. and McLaren, E.: Relationship of Cloud Nuclei Spectra to Aerosol Size Distribution and Composition, Journal of Atmospheric Sci-
905 ences, 28, 382 – 390, https://doi.org/10.1175/1520-0469(1971)028<0382:ROCNST>2.0.CO;2, https://journals.ametsoc.org/view/journals/atsc/28/3/1520-0469_1971_028_0382_rocnst_2_0_co_2.xml, 1971.

Kane, D. B., Oktem, B., and Johnston, M. V.: Nanoparticle Detection by Aerosol Mass Spectrometry, Aerosol Sci. Technol., 34, 520–527, https://doi.org/10.1080/02786820117085, 2001.

Kawamura, K. and Bikkina, S.: A review of dicarboxylic acids and related compounds in atmospheric aerosols: Molecular distributions,
910 sources and transformation, Atmos. Res., 170, 140 – 160, https://doi.org/10.1016/j.atmosres.2015.11.018, 2016.

Kawamura, K., Kasukabe, H., and Barrie, L. A.: Source and reaction pathways of dicarboxylic acids, ketoacids and dicarbonyls in arctic aerosols: One year of observations, Atmos. Environ., 30, 1709 – 1722, http://dx.doi.org/10.1016/1352-2310(95)00395-9, 1996.

Kawamura, K., Kasukabe, H., and Barrie, L. A.: Secondary formation of water-soluble organic acids and α-dicarbonyls and their contributions to total carbon and water-soluble organic carbon: Photochemical aging of organic aerosols in the Arctic spring, J. Geophys.
915 Res.-Atmos., 115, https://doi.org/10.1029/2010JD014299, 2010.

Kawamura, K., Ono, K., Tachibana, E., Charriére, B., and Sempéré, R.: Distributions of low molecular weight dicarboxylic acids, ketoacids and α-dicarbonyls in the marine aerosols collected over the Arctic Ocean during late summer, Biogeosciences, 9, 4725–4737, https://doi.org/10.5194/bg-9-4725-2012, 2012.

Kerminen, V.-M., Teinilä, K., Hillamo, R., and Mäkelä, T.: Size-segregated chemistry of particulate dicarboxylic acids in the Arctic atmosphere, Atmos. Environ., 33, 2089 – 2100, https://doi.org/10.1016/S1352-2310(98)00350-1, 1999.

Kirpes, R. M., Bondy, A. L., Bonanno, D., Moffet, R. C., Wang, B., Laskin, A., Ault, A. P., and Pratt, K. A.: Secondary sulfate is internally mixed with sea spray aerosol and organic aerosol in the winter Arctic, Atmos. Chem. Phys., 18, 3937–3949, https://doi.org/10.5194/acp-18-3937-2018, 2018.

Klonecki, A., Hess, P., Emmons, L., Smith, L., Orlando, J., and Blake, D.: Seasonal changes in the transport of pollutants into the Arctic troposphere-model study, J. Geophys. Res.-Atmos., 108, https://doi.org/10.1029/2002JD002199, 8367, 2003.

Kodros, J. K., Hanna, S. J., Bertram, A. K., Leaitch, W. R., Schulz, H., Herber, A. B., Zanatta, M., Burkart, J., Willis, M. D., Abbatt, J. P. D., and Pierce, J. R.: Size-resolved mixing state of black carbon in the Canadian high Arctic and implications for simulated direct radiative effect, Atmospheric Chemistry and Physics, 18, 11 345–11 361, https://doi.org/10.5194/acp-18-11345-2018, https://acp.copernicus.org/articles/18/11345/2018/, 2018.

Köllner, F., Schneider, J., Willis, M. D., Klimach, T., Helleis, F., Bozem, H., Kunkel, D., Hoor, P., Burkart, J., Leaitch, W. R., Aliabadi, A. A., Abbatt, J. P. D., Herber, A. B., and Borrmann, S.: Particulate trimethylamine in the summertime Canadian high Arctic lower troposphere, Atmos. Chem. Phys., 17, 13 747–13 766, https://doi.org/10.5194/acp-17-13747-2017, 2017.

Kondo, Y., Matsui, H., Moteki, N., Sahu, L., Takegawa, N., Kajino, M., Zhao, Y., Cubison, M. J., Jimenez, J. L., Vay, S., Diskin, G. S., Anderson, B., Wisthaler, A., Mikoviny, T., Fuelberg, H. E., Blake, D. R., Huey, G., Weinheimer, A. J., Knapp, D. J., and Brune, W. H.: Emissions of black carbon, organic, and inorganic aerosols from biomass burning in North America and Asia in 2008, J. Geophys. Res.-Atmos., 116, https://doi.org/10.1029/2010JD015152, 2011.

Kuhn, T., Damoah, R., Bacak, A., and Sloan, J. J.: Characterising aerosol transport into the Canadian High Arctic using aerosol mass spectrometry and Lagrangian modelling, Atmos. Chem. Phys., 10, 10 489–10 502, https://doi.org/10.5194/acp-10-10489-2010, 2010.

Kupiszewski, P., Leck, C., Tjernström, M., Sjogren, S., Sedlar, J., Graus, M., Müller, M., Brooks, B., Swietlicki, E., Norris, S., and Hansel, A.: Vertical profiling of aerosol particles and trace gases over the central Arctic Ocean during summer, Atmos. Chem. Phys., 13, 12 405–12 431, https://doi.org/10.5194/acp-13-12405-2013, 2013.

Lange, R., Dall'Osto, M., Skov, H., Nøjgaard, J., Nielsen, I., Beddows, D., Simo, R., Harrison, R., and Massling, A.: Characterization of distinct Arctic aerosol accumulation modes and their sources, Atmos. Environ., 183, 1–10, https://doi.org/10.1016/j.atmosenv.2018.03.060, 2018.

Lathem, T. L., Beyersdorf, A. J., Thornhill, K. L., Winstead, E. L., Cubison, M. J., Hecobian, A., Jimenez, J. L., Weber, R. J., Anderson, B. E., and Nenes, A.: Analysis of CCN activity of Arctic aerosol and Canadian biomass burning during summer 2008, Atmos. Chem. Phys., 13, 2735–2756, https://doi.org/10.5194/acp-13-2735-2013, 2013.

Law, K. S., Stohl, A., Quinn, P. K., Brock, C. A., Burkhart, J. F., Paris, J.-D., Ancellet, G., Singh, H. B., Roiger, A., Schlager, H., Dibb, J., Jacob, D. J., Arnold, S. R., Pelon, J., and Thomas, J. L.: Arctic Air Pollution: New Insights from POLARCAT-IPY, B. Am. Meteorol. Soc., 95, 1873–1895, https://doi.org/10.1175/BAMS-D-13-00017.1, 2014.

Leaitch, W. R., Sharma, S., Huang, L., Toom-Sautry, D., Chivulescu, A., Macdonald, A. M., von Salzen, K., Pierce, J. R., Bertram, A. K., Schroder, J. C., Shantz, N. C., Chang, R. Y.-W., and Norman, A.-L.: Dimethyl sulfide control of the clean summertime Arctic aerosol and cloud, Elem. Sci. Anth., https://doi.org/10.12952/journal.elementa.000017, 2013.

41

Leaitch, W. R., Korolev, A., Aliabadi, A. A., Burkart, J., Willis, M. D., Abbatt, J. P. D., Bozem, H., Hoor, P., Köllner, F., Schneider, J., Herber, A., Konrad, C., and Brauner, R.: Effects of 20–100 nm particles on liquid clouds in the clean summertime Arctic, Atmos. Chem. Phys., 16, 11 107–11 124, https://doi.org/10.5194/acp-16-11107-2016, 2016.

Leaitch, W. R., Russell, L. M., Liu, J., Kolonjari, F., Toom, D., Huang, L., Sharma, S., Chivulescu, A., Veber, D., and Zhang, W.: Organic functional groups in the submicron aerosol at 82.5° N, 62.5° W from 2012 to 2014, Atmos. Chem. Phys., 18, 3269–3287, https://doi.org/10.5194/acp-18-3269-2018, 2018.

Lee, S.-H., Murphy, D. M., Thomson, D. S., and Middlebrook, A. M.: Nitrate and oxidized organic ions in single particle mass spectra during the 1999 Atlanta Supersite Project, J. Geophys. Res.-Atmos., 108, https://doi.org/10.1029/2001JD001455, 8471, 2003.

Liu, D., Quennehen, B., Darbyshire, E., Allan, J. D., Williams, P. I., Taylor, J. W., Bauguitte, S. J.-B., Flynn, M. J., Lowe, D., Gallagher, M. W., Bower, K. N., Choularton, T. W., and Coe, H.: The importance of Asia as a source of black carbon to the European Arctic during springtime 2013, Atmos. Chem. Phys., 15, 11 537–11 555, https://doi.org/10.5194/acp-15-11537-2015, 2015.

Liu, P., Ziemann, P. J., Kittelson, D. B., and McMurry, P. H.: Generating Particle Beams of Controlled Dimensions and Divergence: I. Theory of Particle Motion in Aerodynamic Lenses and Nozzle Expansions, Aerosol Sci. Technol., 22, 293–313, https://doi.org/10.1080/02786829408959748, 1995a.

Liu, P., Ziemann, P. J., Kittelson, D. B., and McMurry, P. H.: Generating Particle Beams of Controlled Dimensions and Divergence: II. Experimental Evaluation of Particle Motion in Aerodynamic Lenses and Nozzle Expansions, Aerosol Sci. Technol., 22, 314–324, https://doi.org/10.1080/02786829408959749, 1995b.

Liu, P. S. K., Deng, R., Smith, K. A., Williams, L. R., Jayne, J. T., Canagaratna, M. R., Moore, K., Onasch, T. B., Worsnop, D. R., and Deshler, T.: Transmission Efficiency of an Aerodynamic Focusing Lens System: Comparison of Model Calculations and Laboratory Measurements for the Aerodyne Aerosol Mass Spectrometer, Aerosol Sci. Technol., 41, 721–733, https://doi.org/10.1080/02786820701422278, 2007.

Liu, Y., Hu, C., Zhan, W., Sun, C., Murch, B., and Ma, L.: Identifying industrial heat sources using time-series of the VIIRS Nightfire product with an object-oriented approach, Remote Sens. Environ., 204, 347 – 365, https://doi.org/10.1016/j.rse.2017.10.019, 2018.

Lutsch, E., Dammers, E., Conway, S., and Strong, K.: Long-range transport of NH_3, CO, HCN, and C_2H_6 from the 2014 Canadian Wildfires, Geophys. Res. Lett., 43, 8286–8297, https://doi.org/10.1002/2016GL070114, 2016GL070114, 2016.

Marelle, L., Raut, J.-C., Law, K. S., and Duclaux, O.: Current and Future Arctic Aerosols and Ozone From Remote Emissions and Emerging Local Sources - Modeled Source Contributions and Radiative Effects, J. Geophys. Res.-Atmos., 123, 12,942–12,963, https://doi.org/10.1029/2018JD028863, 2018.

Martin, M., Chang, R. Y.-W., Sierau, B., Sjogren, S., Swietlicki, E., Abbatt, J. P. D., Leck, C., and Lohmann, U.: Cloud condensation nuclei closure study on summer arctic aerosol, Atmospheric Chemistry and Physics, 11, 11 335–11 350, https://doi.org/10.5194/acp-11-11335-2011, https://acp.copernicus.org/articles/11/11335/2011/, 2011.

Matsui, H., Kondo, Y., Moteki, N., Takegawa, N., Sahu, L. K., Koike, M., Zhao, Y., Fuelberg, H. E., Sessions, W. R., Diskin, G., Anderson, B. E., Blake, D. R., Wisthaler, A., Cubison, M. J., and Jimenez, J. L.: Accumulation-mode aerosol number concentrations in the Arctic during the ARCTAS aircraft campaign: Long-range transport of polluted and clean air from the Asian continent, Journal of Geophysical Research: Atmospheres, 116, https://doi.org/https://doi.org/10.1029/2011JD016189, https://agupubs.onlinelibrary.wiley.com/doi/abs/10.1029/2011JD016189, 2011a.

Matsui, H., Kondo, Y., Moteki, N., Takegawa, N., Sahu, L. K., Zhao, Y., Fuelberg, H. E., Sessions, W. R., Diskin, G., Blake, D. R., Wisthaler, A., and Koike, M.: Seasonal variation of the transport of black carbon aerosol from the Asian continent to the Arctic during the ARCTAS

aircraft campaign, Journal of Geophysical Research: Atmospheres, 116, https://doi.org/https://doi.org/10.1029/2010JD015067, https://agupubs.onlinelibrary.wiley.com/doi/abs/10.1029/2010JD015067, 2011b.

Mauritsen, T., Sedlar, J., Tjernström, M., Leck, C., Martin, M., Shupe, M., Sjogren, S., Sierau, B., Persson, P. O. G., Brooks, I. M., and Swietlicki, E.: An Arctic CCN-limited cloud-aerosol regime, Atmos. Chem. Phys., 11, 165–173, https://doi.org/10.5194/acp-11-165-2011, 2011.

MaxMind: https://www.maxmind.com/en/free-world-cities-database, last access: 10.06.2018, 2018.

McFiggans, G., Artaxo, P., Baltensperger, U., Coe, H., Facchini, M. C., Feingold, G., Fuzzi, S., Gysel, M., Laaksonen, A., Lohmann, U., Mentel, T. F., Murphy, D. M., O'Dowd, C. D., Snider, J. R., and Weingartner, E.: The effect of physical and chemical aerosol properties on warm cloud droplet activation, Atmospheric Chemistry and Physics, 6, 2593–2649, https://doi.org/10.5194/acp-6-2593-2006, https://acp.copernicus.org/articles/6/2593/2006/, 2006.

Moffet, R. C. and Prather, K. A.: In-situ measurements of the mixing state and optical properties of soot with implications for radiative forcing estimates, P. Natl. Acad. Sci., 106, 11 872–11 877, https://doi.org/10.1073/pnas.0900040106, 2009.

Molleker, S., Helleis, F., Klimach, T., Appel, O., Clemen, H.-C., Dragoneas, A., Gurk, C., Hünig, A., Köllner, F., Rubach, F., Schulz, C., Schneider, J., and Borrmann, S.: Application of an O-ring pinch device as a constant-pressure inlet (CPI) for airborne sampling, Atmospheric Measurement Techniques, 13, 3651–3660, https://doi.org/10.5194/amt-13-3651-2020, https://amt.copernicus.org/articles/13/3651/2020/, 2020.

Moore, R. H., Bahreini, R., Brock, C. A., Froyd, K. D., Cozic, J., Holloway, J. S., Middlebrook, A. M., Murphy, D. M., and Nenes, A.: Hygroscopicity and composition of Alaskan Arctic CCN during April 2008, Atmospheric Chemistry and Physics, 11, 11 807–11 825, https://doi.org/10.5194/acp-11-11807-2011, https://acp.copernicus.org/articles/11/11807/2011/, 2011.

Moore, R. H., Karydis, V. A., Capps, S. L., Lathem, T. L., and Nenes, A.: Droplet number uncertainties associated with CCN: an assessment using observations and a global model adjoint, Atmos. Chem. Phys., 13, 4235–4251, https://doi.org/10.5194/acp-13-4235-2013, 2013.

Najafi, M. R., Zwiers, F. W., and Gillett, N. P.: Attribution of Arctic temperature change to greenhouse-gas and aerosol influences, Nat. Clim. Change, 5, 246–249, http://dx.doi.org/10.1038/nclimate2524, 2015.

Neubauer, K. R., Johnston, M. V., and Wexler, A. S.: Humidity effects on the mass spectra of single aerosol particles, Atmos. Environ., 32, 2521–2529, https://doi.org/10.1016/S1352-2310(98)00005-3, 1998.

Norgren, M. S., de Boer, G., and Shupe, M. D.: Observed aerosol suppression of cloud ice in low-level Arctic mixed-phase clouds, Atmospheric Chemistry and Physics, 18, 13 345–13 361, https://doi.org/10.5194/acp-18-13345-2018, https://acp.copernicus.org/articles/18/13345/2018/, 2018.

Orellana, M. V., Matrai, P. A., Leck, C., Rauschenberg, C. D., Lee, A. M., and Coz, E.: Marine microgels as a source of cloud condensation nuclei in the high Arctic, P. Natl. Acad. Sci., 108, 13 612–13 617, https://doi.org/10.1073/pnas.1102457108, 2011.

Paris, J.-D., Stohl, A., Nédélec, P., Arshinov, M. Y., Panchenko, M. V., Shmargunov, V. P., Law, K. S., Belan, B. D., and Ciais, P.: Wildfire smoke in the Siberian Arctic in summer: source characterization and plume evolution from airborne measurements, Atmos. Chem. Phys., 9, 9315–9327, https://doi.org/10.5194/acp-9-9315-2009, 2009.

Pithan, F. and Mauritsen, T.: Arctic amplification dominated by temperature feedbacks in contemporary climate models, Nature Geoscience, 7, 181–184, https://doi.org/10.1038/ngeo2071, https://doi.org/10.1038/ngeo2071, 2014.

Prather, K. A., Bertram, T. H., Grassian, V. H., Deane, G. B., Stokes, M. D., DeMott, P. J., Aluwihare, L. I., Palenik, B. P., Azam, F., Seinfeld, J. H., Moffet, R. C., Molina, M. J., Cappa, C. D., Geiger, F. M., Roberts, G. C., Russell, L. M., Ault, A. P., Baltrusaitis, J., Collins, D. B., Corrigan, C. E., Cuadra-Rodriguez, L. A., Ebben, C. J., Forestieri, S. D., Guasco, T. L., Hersey, S. P., Kim, M. J.,

Lambert, W. F., Modini, R. L., Mui, W., Pedler, B. E., Ruppel, M. J., Ryder, O. S., Schoepp, N. G., Sullivan, R. C., and Zhao, D.: Bringing the ocean into the laboratory to probe the chemical complexity of sea spray aerosol, P. Natl. Acad. Sci., 110, 7550–7555, https://doi.org/10.1073/pnas.1300262110, 2013.

Pratt, K. A. and Prather, K. A.: Real-Time, Single-Particle Volatility, Size, and Chemical Composition Measurements of Aged Urban Aerosols, Environ. Sci. Technol., 43, 8276–8282, https://doi.org/10.1021/es902002t, pMID: 19924956, 2009.

Pratt, K. A., Murphy, S. M., Subramanian, R., DeMott, P. J., Kok, G. L., Campos, T., Rogers, D. C., Prenni, A. J., Heymsfield, A. J., Seinfeld, J. H., and Prather, K. A.: Flight-based chemical characterization of biomass burning aerosols within two prescribed burn smoke plumes, Atmos. Chem. Phys., 11, 12 549–12 565, https://doi.org/10.5194/acp-11-12549-2011, 2011.

Qin, X., Bhave, P. V., and Prather, K. A.: Comparison of Two Methods for Obtaining Quantitative Mass Concentrations from Aerosol Time-of-Flight Mass Spectrometry Measurements, Anal. Chem., 78, 6169–6178, https://doi.org/10.1021/ac060395q, 2006.

Quennehen, B., Schwarzenboeck, A., Schmale, J., Schneider, J., Sodemann, H., Stohl, A., Ancellet, G., Crumeyrolle, S., and Law, K. S.: Physical and chemical properties of pollution aerosol particles transported from North America to Greenland as measured during the POLARCAT summer campaign, Atmos. Chem. Phys., 11, 10 947–10 963, https://doi.org/10.5194/acp-11-10947-2011, 2011.

Quinn, P. K., Miller, T. L., Bates, T. S., Ogren, J. A., Andrews, E., and Shaw, G. E.: A 3-year record of simultaneously measured aerosol chemical and optical properties at Barrow, Alaska, J. Geophys. Res.-Atmos., 107, https://doi.org/10.1029/2001JD001248, 2002.

Quinn, P. K., Bates, T. S., Baum, E., Doubleday, N., Fiore, A. M., Flanner, M., Fridlind, A., Garrett, T. J., Koch, D., Menon, S., Shindell, D., Stohl, A., and Warren, S. G.: Short-lived pollutants in the Arctic: their climate impact and possible mitigation strategies, Atmos. Chem. Phys., 8, 1723–1735, https://doi.org/10.5194/acp-8-1723-2008, 2008.

Radke, L. F. and Hobbs, P. V.: Arctic hazes in summer over Greenland and the North American Arctic. III: A contribution from the natural burning of carbonaceous materials and pyrites, J. Atmos. Chem., 9, 161–167, https://doi.org/10.1007/BF00052830, 1989.

Randerson, J. T., Liu, H., Flanner, M. G., Chambers, S. D., Jin, Y., Hess, P. G., Pfister, G., Mack, M. C., Treseder, K. K., Welp, L. R., Chapin, F. S., Harden, J. W., Goulden, M. L., Lyons, E., Neff, J. C., Schuur, E. A. G., and Zender, C. S.: The Impact of Boreal Forest Fire on Climate Warming, Science, 314, 1130–1132, https://doi.org/10.1126/science.1132075, 2006.

Rehbein, P. J. G., Jeong, C.-H., McGuire, M. L., Yao, X., Corbin, J. C., and Evans, G. J.: Cloud and Fog Processing Enhanced Gas-to-Particle Partitioning of Trimethylamine, Environ. Sci. Technol., 45, 4346–4352, https://doi.org/10.1021/es1042113, 2011.

Roth, A., Schneider, J., Klimach, T., Mertes, S., van Pinxteren, D., Herrmann, H., and Borrmann, S.: Aerosol properties, source identification, and cloud processing in orographic clouds measured by single particle mass spectrometry on a central European mountain site during HCCT-2010, Atmos. Chem. Phys., 16, 505–524, https://doi.org/10.5194/acp-16-505-2016, 2016.

Sand, M., Berntsen, T. K., Kay, J. E., Lamarque, J. F., Seland, Ø., and Kirkevåg, A.: The Arctic response to remote and local forcing of black carbon, Atmospheric Chemistry and Physics, 13, 211–224, https://doi.org/10.5194/acp-13-211-2013, https://acp.copernicus.org/articles/13/211/2013/, 2013a.

Sand, M., Berntsen, T. K., Seland, y., and Kristjánsson, J. E.: Arctic surface temperature change to emissions of black carbon within Arctic or midlatitudes, Journal of Geophysical Research: Atmospheres, 118, 7788–7798, https://doi.org/https://doi.org/10.1002/jgrd.50613, https://agupubs.onlinelibrary.wiley.com/doi/abs/10.1002/jgrd.50613, 2013b.

Sand, M., Samset, B. H., Balkanski, Y., Bauer, S., Bellouin, N., Berntsen, T. K., Bian, H., Chin, M., Diehl, T., Easter, R., Ghan, S. J., Iversen, T., Kirkevåg, A., Lamarque, J.-F., Lin, G., Liu, X., Luo, G., Myhre, G., Noije, T. V., Penner, J. E., Schulz, M., Seland, Ø., Skeie, R. B., Stier, P., Takemura, T., Tsigaridis, K., Yu, F., Zhang, K., and Zhang, H.: Aerosols at the poles: an AeroCom Phase II multi-model

evaluation, Atmospheric Chemistry and Physics, 17, 12 197–12 218, https://doi.org/10.5194/acp-17-12197-2017, https://acp.copernicus.org/articles/17/12197/2017/, 2017.

Sato, Y., Miura, H., Yashiro, H., Goto, D., Takemura, T., Tomita, H., and Nakajima, T.: Unrealistically pristine air in the Arctic produced by current global scale models, Scientific Reports, 6, 26 561, https://doi.org/10.1038/srep26561, https://doi.org/10.1038/srep26561, 2016.

Schacht, J., Heinold, B., Quaas, J., Backman, J., Cherian, R., Ehrlich, A., Herber, A., Huang, W. T. K., Kondo, Y., Massling, A., Sinha, P. R., Weinzierl, B., Zanatta, M., and Tegen, I.: The importance of the representation of air pollution emissions for the modeled distribution and radiative effects of black carbon in the Arctic, Atmospheric Chemistry and Physics, 19, 11 159–11 183, https://doi.org/10.5194/acp-19-11159-2019, https://acp.copernicus.org/articles/19/11159/2019/, 2019.

Scharffe, D., Slemr, F., Brenninkmeijer, C. A. M., and Zahn, A.: Carbon monoxide measurements onboard the CARIBIC passenger aircraft using UV resonance fluorescence, Atmos. Meas. Tech., 5, 1753–1760, https://doi.org/10.5194/amt-5-1753-2012, 2012.

Schmale, J., Schneider, J., Ancellet, G., Quennehen, B., Stohl, A., Sodemann, H., Burkhart, J. F., Hamburger, T., Arnold, S. R., Schwarzenboeck, A., Borrmann, S., and Law, K. S.: Source identification and airborne chemical characterisation of aerosol pollution from long-range transport over Greenland during POLARCAT summer campaign 2008, Atmos. Chem. Phys., 11, 10 097–10 123, https://doi.org/10.5194/acp-11-10097-2011, 2011.

Schmidt, S., Schneider, J., Klimach, T., Mertes, S., Schenk, L. P., Kupiszewski, P., Curtius, J., and Borrmann, S.: Online single particle analysis of ice particle residuals from mountain-top mixed-phase clouds using laboratory derived particle type assignment, Atmos. Chem. Phys., 17, 575–594, https://doi.org/10.5194/acp-17-575-2017, 2017.

Schroeder, W. and Giglio, L.: NASA VIIRS Land Science Investigator Processing System (SIPS) Visible Infrared Imaging Radiometer Suite (VIIRS) 375 m & 750 m Active Fire Products: Product User's Guide Version 1.4, Tech. rep., Department of Geographical Sciences, University of Maryland, 2018.

Schroeder, W., Oliva, P., Giglio, L., and Csiszar, I. A.: The New VIIRS 375m active fire detection data product: Algorithm description and initial assessment, Remote Sens. Environ., 143, 85 – 96, https://doi.org/10.1016/j.rse.2013.12.008, 2014.

Schulz, H., Zanatta, M., Bozem, H., Leaitch, W. R., Herber, A. B., Burkart, J., Willis, M. D., Kunkel, D., Hoor, P. M., Abbatt, J. P. D., and Gerdes, R.: High Arctic aircraft measurements characterising black carbon vertical variability in spring and summer, Atmos. Chem. Phys., 2019, 2361–2384, https://doi.org/10.5194/acp-19-2361-2019, 2019.

Schwarz, J. P., Gao, R. S., Fahey, D. W., Thomson, D. S., Watts, L. A., Wilson, J. C., Reeves, J. M., Darbeheshti, M., Baumgardner, D. G., Kok, G. L., Chung, S. H., Schulz, M., Hendricks, J., Lauer, A., Kärcher, B., Slowik, J. G., Rosenlof, K. H., Thompson, T. L., Langford, A. O., Loewenstein, M., and Aikin, K. C.: Single-particle measurements of midlatitude black carbon and light-scattering aerosols from the boundary layer to the lower stratosphere, J. Geophys. Res.-Atmos., 111, https://doi.org/10.1029/2006JD007076, 2006.

Seibert, P. and Frank, A.: Source-receptor matrix calculation with a Lagrangian particle dispersion model in backward mode, Atmos. Chem. Phys., 4, 51–63, https://doi.org/10.5194/acp-4-51-2004, 2004.

Serreze, M. C. and Barry, R. G.: Processes and impacts of Arctic amplification: A research synthesis, Global Planet. Change, 77, 85 – 96, https://doi.org/https://doi.org/10.1016/j.gloplacha.2011.03.004, 2011.

Serreze, M. C. and Francis, J. A.: The Arctic Amplification Debate, Climatic Change, 76, 241–264, https://doi.org/10.1007/s10584-005-9017-y, 2006.

Serreze, M. C., Barrett, A. P., Stroeve, J. C., Kindig, D. N., and Holland, M. M.: The emergence of surface-based Arctic amplification, The Cryosphere, 3, 11–19, https://doi.org/10.5194/tc-3-11-2009, 2009.

Sharma, S., Ishizawa, M., Chan, D., Lavoué, D., Andrews, E., Eleftheriadis, K., and Maksyutov, S.: 16-year simulation of Arctic black carbon: Transport, source contribution, and sensitivity analysis on deposition, J. Geophys. Res.-Atmos., 118, 943–964, https://doi.org/10.1029/2012JD017774, 2013.

Shaw, P. M., Russell, L. M., Jefferson, A., and Quinn, P. K.: Arctic organic aerosol measurements show particles from mixed combustion in spring haze and from frost flowers in winter, Geophysical Research Letters, 37, https://doi.org/10.1029/2010GL042831, https://agupubs.onlinelibrary.wiley.com/doi/abs/10.1029/2010GL042831, 2010.

Shindell, D. and Faluvegi, G.: Climate response to regional radiative forcing during the twentieth century, Nature Geoscience, 2, 294–300, http://dx.doi.org/10.1038/ngeo473, 2009.

Shindell, D. T., Chin, M., Dentener, F., Doherty, R. M., Faluvegi, G., Fiore, A. M., Hess, P., Koch, D. M., MacKenzie, I. A., Sanderson, M. G., Schultz, M. G., Schulz, M., Stevenson, D. S., Teich, H., Textor, C., Wild, O., Bergmann, D. J., Bey, I., Bian, H., Cuvelier, C., Duncan, B. N., Folberth, G., Horowitz, L. W., Jonson, J., Kaminski, J. W., Marmer, E., Park, R., Pringle, K. J., Schroeder, S., Szopa, S., Takemura, T., Zeng, G., Keating, T. J., and Zuber, A.: A multi-model assessment of pollution transport to the Arctic, Atmos. Chem. Phys., 8, 5353–5372, https://doi.org/10.5194/acp-8-5353-2008, 2008.

Shupe, M. D. and Intrieri, J. M.: Cloud Radiative Forcing of the Arctic Surface: The Influence of Cloud Properties, Surface Albedo, and Solar Zenith Angle, Journal of Climate, 17, 616 – 628, https://doi.org/10.1175/1520-0442(2004)017<0616:CRFOTA>2.0.CO;2, https://journals.ametsoc.org/view/journals/clim/17/3/1520-0442_2004_017_0616_crfota_2.0.co_2.xml, 2004.

Sierau, B., Chang, R. Y.-W., Leck, C., Paatero, J., and Lohmann, U.: Single-particle characterization of the high-Arctic summertime aerosol, Atmos. Chem. Phys., 14, 7409–7430, https://doi.org/10.5194/acp-14-7409-2014, 2014.

Silva, P. J. and Prather, K. A.: Interpretation of Mass Spectra from Organic Compounds in Aerosol Time-of-Flight Mass Spectrometry, Anal. Chem., 72, 3553–3562, https://doi.org/10.1021/ac9910132, 2000.

Silva, P. J., Liu, D.-Y., Noble, C. A., and Prather, K. A.: Size and Chemical Characterization of Individual Particles Resulting from Biomass Burning of Local Southern California Species, Environ. Sci. Technol., 33, 3068–3076, https://doi.org/10.1021/es980544p, 1999.

Singh, H. B., Anderson, B. E., Brune, W. H., Cai, C., Cohen, R. C., Crawford, J. H., Cubison, M. J., Czech, E. P., Emmons, L., Fuelberg, H. E., Huey, G., Jacob, D. J., Jimenez, J. L., Kaduwela, A., Kondo, Y., Mao, J., Olson, J. R., Sachse, G. W., Vay, S. A., Weinheimer, A., Wennberg, P. O., and Wisthaler, A.: Pollution influences on atmospheric composition and chemistry at high northern latitudes: Boreal and California forest fire emissions, Atmos. Environ., 44, 4553–4564, http://www.sciencedirect.com/science/article/pii/S1352231010007004, 2010.

Sobhani, N., Kulkarni, S., and Carmichael, G. R.: Source sector and region contributions to black carbon and $PM_{2.5}$ in the Arctic, Atmos. Chem. Phys., 18, 18 123–18 148, https://doi.org/10.5194/acp-18-18123-2018, 2018.

Spencer, M. T., Holecek, J. C., Corrigan, C. E., Ramanathan, V., and Prather, K. A.: Size-resolved chemical composition of aerosol particles during a monsoonal transition period over the Indian Ocean, J. Geophys. Res.-Atmos., 113, https://doi.org/10.1029/2007JD008657, 2008.

Stohl, A.: Computation, accuracy and applications of trajectories: A review and bibliography, Atmos. Environ., 32, 947 – 966, http://dx.doi.org/10.1016/S1352-2310(97)00457-3, 1998.

Stohl, A.: Characteristics of atmospheric transport into the Arctic troposphere, J. Geophys. Res.-Atmos., 111, https://doi.org/10.1029/2005JD006888, 2006.

Stohl, A., Forster, C., Eckhardt, S., Spichtinger, N., Huntrieser, H., Heland, J., Schlager, H., Wilhelm, S., Arnold, F., and Cooper, O.: A backward modeling study of intercontinental pollution transport using aircraft measurements, J. Geophys. Res.-Atmos., 108, https://doi.org/10.1029/2002JD002862, 2003.

Stohl, A., Forster, C., Frank, A., Seibert, P., and Wotawa, G.: Technical note: The Lagrangian particle dispersion model FLEXPART version 6.2, Atmos. Chem. Phys., 5, 2461–2474, https://doi.org/10.5194/acp-5-2461-2005, 2005.

Stohl, A., Klimont, Z., Eckhardt, S., Kupiainen, K., Shevchenko, V. P., Kopeikin, V. M., and Novigatsky, A. N.: Black carbon in the Arctic: the underestimated role of gas flaring and residential combustion emissions, Atmos. Chem. Phys., 13, 8833–8855, https://doi.org/10.5194/acp-13-8833-2013, 2013.

Stroeve, J. C., Serreze, M. C., Holland, M. M., Kay, J. E., Malanik, J., and Barrett, A. P.: The Arctic's rapidly shrinking sea ice cover: a research synthesis, Climatic Change, 110, 1005–1027, https://doi.org/10.1007/s10584-011-0101-1, 2012.

Stull, R. B.: An Introduction to Boundary Layer Meteorology, Kluwer Academic Publishers, https://doi.org/10.1007/978-94-009-3027-8, 1997.

Sullivan, R. C. and Prather, K. A.: Investigations of the Diurnal Cycle and Mixing State of Oxalic Acid in Individual Particles in Asian Aerosol Outflow, Environ. Sci. Technol., 41, 8062–8069, https://doi.org/10.1021/es071134g, 2007.

Thomson, D. S., Middlebrook, A. M., and Murphy, D. M.: Thresholds for Laser-Induced Ion Formation from Aerosols in a Vacuum Using Ultraviolet and Vacuum-Ultraviolet Laser Wavelengths, Aerosol Sci. Technol., 26, 544–559, https://doi.org/10.1080/02786829708965452, 1997.

Tjernström, M., Birch, C. E., Brooks, I. M., Shupe, M. D., Persson, P. O. G., Sedlar, J., Mauritsen, T., Leck, C., Paatero, J., Szczodrak, M., and Wheeler, C. R.: Meteorological conditions in the central Arctic summer during the Arctic Summer Cloud Ocean Study (ASCOS), Atmos. Chem. Phys., 12, 6863–6889, https://doi.org/10.5194/acp-12-6863-2012, 2012.

Tremblay, S., Picard, J.-C., Bachelder, J. O., Lutsch, E., Strong, K., Fogal, P., Leaitch, W. R., Sharma, S., Kolonjari, F., Cox, C. J., Chang, R. Y.-W., and Hayes, P. L.: Characterization of aerosol growth events over Ellesmere Island during the summers of 2015 and 2016, Atmos. Chem. Phys., 19, 5589–5604, https://doi.org/10.5194/acp-19-5589-2019, 2019.

Wandel, M.: CO-Messung in der Arktis im Rahmen der NETCARE-Kampa-gne, Master's thesis, Johannes Gutenberg-Universität Mainz, 2015.

Wetter3: http://www1.wetter3.de/archiv_gfs_dt.html, last access: July 2020, 2020.

Willis, M. D., Burkart, J., Thomas, J. L., Köllner, F., Schneider, J., Bozem, H., Hoor, P. M., Aliabadi, A. A., Schulz, H., Herber, A. B., Leaitch, W. R., and Abbatt, J. P. D.: Growth of nucleation mode particles in the summertime Arctic: a case study, Atmos. Chem. Phys., 16, 7663–7679, https://doi.org/10.5194/acp-16-7663-2016, 2016.

Willis, M. D., Köllner, F., Burkart, J., Bozem, H., Thomas, J. L., Schneider, J., Aliabadi, A. A., Hoor, P. M., Schulz, H., Herber, A. B., Leaitch, W. R., and Abbatt, J. P. D.: Evidence for marine biogenic influence on summertime Arctic aerosol, Geophys. Res. Lett., 44, 6460–6470, https://doi.org/10.1002/2017GL073359, 2017.

Willis, M. D., Leaitch, W. R., and Abbatt, J. P.: Processes Controlling the Composition and Abundance of Arctic Aerosol, Rev. Geophys., 56, 621–671, https://doi.org/10.1029/2018RG000602, 2018.

Winiger, P., Andersson, A., Eckhardt, S., Stohl, A., Semiletov, I. P., Dudarev, O. V., Charkin, A., Shakhova, N., Klimont, Z., Heyes, C., and Gustafsson, Ö.: Siberian Arctic black carbon sources constrained by model and observation, P. Natl. Acad. Sci., 114, E1054–E1061, https://doi.org/10.1073/pnas.1613401114, 2017.

Winiger, P., Barrett, T. E., Sheesley, R. J., Huang, L., Sharma, S., Barrie, L. A., Yttri, K. E., Evangeliou, N., Eckhardt, S., Stohl, A., Klimont, Z., Heyes, C., Semiletov, I. P., Dudarev, O. V., Charkin, A., Shakhova, N., Holmstrand, H., Andersson, A., and Gustafsson, Ö.: Source apportionment of circum-Arctic atmospheric black carbon from isotopes and modeling, Science Advances, 5, https://doi.org/10.1126/sciadv.aau8052, https://advances.sciencemag.org/content/5/2/eaau8052, 2019.

Xu, J.-W., Martin, R. V., Morrow, A., Sharma, S., Huang, L., Leaitch, W. R., Burkart, J., Schulz, H., Zanatta, M., Willis, M. D., Henze, D. K., Lee, C. J., Herber, A. B., and Abbatt, J. P. D.: Source attribution of Arctic black carbon constrained by aircraft and surface measurements, Atmos. Chem. Phys., 17, 11 971–11 989, https://doi.org/10.5194/acp-17-11971-2017, 2017.

Yang, F., Chen, H., Wang, X., Yang, X., Du, J., and Chen, J.: Single particle mass spectrometry of oxalic acid in ambient aerosols in Shanghai: Mixing state and formation mechanism, Atmos. Environ., 43, 3876 – 3882, https://doi.org/10.1016/j.atmosenv.2009.05.002, 2009.

Yang, Y., Wang, H., Smith, S. J., Easter, R. C., and Rasch, P. J.: Sulfate Aerosol in the Arctic: Source Attribution and Radiative Forcing, J. Geophys. Res.-Atmos., 123, 1899–1918, https://doi.org/10.1002/2017JD027298, 2018.

Zamora, L. M., Kahn, R. A., Cubison, M. J., Diskin, G. S., Jimenez, J. L., Kondo, Y., McFarquhar, G. M., Nenes, A., Thornhill, K. L., Wisthaler, A., Zelenyuk, A., and Ziemba, L. D.: Aircraft-measured indirect cloud effects from biomass burning smoke in the Arctic and subarctic, Atmospheric Chemistry and Physics, 16, 715–738, https://doi.org/10.5194/acp-16-715-2016, https://acp.copernicus.org/articles/16/715/2016/, 2016.

Zauscher, M. D., Wang, Y., Moore, M. J. K., Gaston, C. J., and Prather, K. A.: Air Quality Impact and Physicochemical Aging of Biomass Burning Aerosols during the 2007 San Diego Wildfires, Environ. Sci. Technol., 47, 7633–7643, https://doi.org/10.1021/es4004137, 2013.

Zhang, X., Smith, K. A., Worsnop, D. R., Jimenez, J. L., Jayne, J. T., Kolb, C. E., Morris, J., and Davidovits, P.: Numerical Characterization of Particle Beam Collimation: Part II Integrated Aerodynamic-Lens-Nozzle System, Aerosol Sci. Technol., 38, 619–638, https://doi.org/10.1080/02786820490479833, 2004.

Zhu, C., Kanaya, Y., Takigawa, M., Ikeda, K., Tanimoto, H., Taketani, F., Miyakawa, T., Kobayashi, H., and Pisso, I.: FLEXPART v10.1 simulation of source contributions to Arctic black carbon, Atmospheric Chemistry and Physics, 20, 1641–1656, https://doi.org/10.5194/acp-20-1641-2020, https://www.atmos-chem-phys.net/20/1641/2020/, 2020.

1 Hit rate variability during NETCARE 2014

The following approach estimates the NETCARE 2014 hit rate variability that is controlled by several instrumental issues. The instrument hit rate is defined as the number of particles that are successfully ionized by the ablation laser and that create a mass spectrum relative to the number of laser shots (Clemen et al., 2020). The triggered shot requires that the particle velocity was prior successfully determined and that the laser was ready to shoot (Brands et al., 2011). The maximum shot repetition rate of the Nd:YAG laser was set to 12 Hz. Figure S1 presents the distribution of the averaged hit rate measured
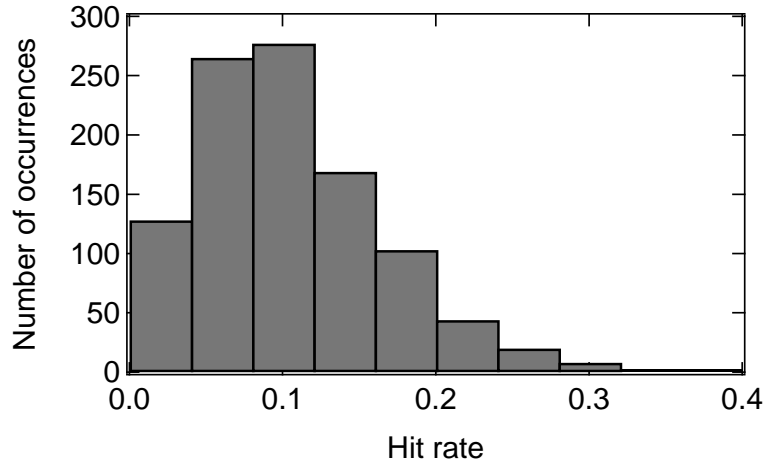
Figure S1. Histogram of hit rate values with each value includes $N = 100$ trials (here, laser shots), measured during the Arctic field experiment (NETCARE 2014) outside clouds. The averaged hit rate value is 0.1 ($p = 0.1$).

during the Arctic field experiment outside clouds. By assuming that the measured distribution cannot solely be explained by binomial distributed numbers, it needs to be described by a combination of both binomial distributed numbers and the variability caused by instrumental issues. Combined with the Gaussian propagation of uncertainties, the relative standard deviation of the measured hit rate distribution ($\sigma_{\mathrm{measured}}$) can thus be estimated as follows:

$$\sigma^2_{\mathrm{measured}} = \sigma^2_{\mathrm{binomial}} + \sigma^2_{\mathrm{others}}, \tag{1}$$

with $\sigma_{\mathrm{measured}} = 0.06$, the relative standard deviation related to instrumental issues (σ_{others}), and the relative standard deviation of the Binomial probability distribution ($\sigma_{\mathrm{binomial}}$), which is calculated as follows:

$$\sigma_{\mathrm{binomial}} = \frac{\sqrt{N \cdot p \cdot q}}{N}, \tag{2}$$

with trials (N) is 100, probability of success (p) is 0.1, and probability of failure (q) is 0.9. The resulting $\sigma_{\mathrm{binomial}}$ is 0.03. Based on $\sigma_{\mathrm{binomial}}$ and Eq. 1, the σ_{others} is 0.05. Together, since the averaged ALABAMA hit rate of 0.1 can vary by 0.05 due to instrumental issues, it is assumed for the analyses in Sections 3.2 and 3.3 that the particle fraction needs to vary by more than a factor of 2 to be significant.

2 Source sectors

2.1 Vegetation fires

The Visible Infrared Imaging Radiometer Suite (VIIRS) onboard the Suomi National Polar-Orbiting Partnership spacecraft can detect sub-pixel thermal anomalies by signals in mid- and thermal infrared spectral range (Schroeder et al., 2014; Schroeder
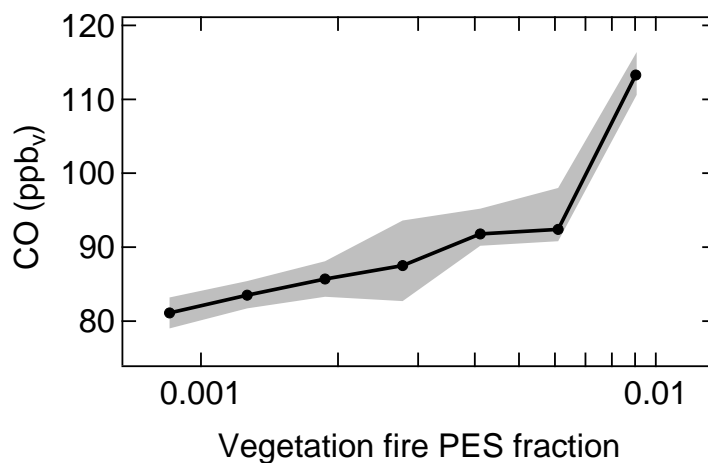
Figure S2. CO mixing ratios as a function of FLEXPART predicted PES fraction over vegetation fires during the southern air mass period. The graph presents the median (solid line with marker) and interquartile ranges (shaded area) of the CO mixing ratios.

and Giglio, 2018). Thermal anomalies typically include both active vegetation fires and industrial heat sources by fossil-fuel combustion etc. Data of the so-called near real-time VIIRS 375 m Active Fire product were downloaded online for 19 June until 21 July 2014 (NASA, 2018) and projected on the gridded maps by adding up observations in each grid cell. Thermal anomalies were identified by one or more observations per grid cell within the respective time.

The presence of vegetation fires can be distinguished from other thermal anomalies by the following approach. Anthropogenic heat sources, such as industry, flaring, and densely populated regions, are separately mapped (see following sections) and subsequently excluded from the thermal anomaly map. Residual heat sources in Fig. 4a thus present vegetation fires, accumulated for 19 June until 21 July 2014. This approach looks reasonable in comparison with Arndt et al. (2015), at least for boreal fires in northern Canada and Siberia. North American and north Asian biomass burning budgets were anomalously high in 2014 compared to 2001 - 2013 (Fig. 2.57 and Table 2.8 in Arndt et al., 2015). Particularly in summer 2014, large fires in the Great Slave Lake region and Siberia were evident (Fig. 2.40 in Arndt et al., 2015), confirming results in Fig. 4a. Consistent with this, Fig. S2 shows a positive correlation between CO mixing ratios and residence time spent over vegetation fires. However, the main weakness of this approach is given by temporal variabilities of the data sets.

Vegetation fire injection heights are highly variable owing to a combination of fire type, fuel consumption, and prevailing meteorological conditions (e.g., Lavoué et al., 2000; Andreae and Merlet, 2001; Leung et al., 2007; Kondo et al., 2011; Val Martin et al., 2018). Several studies show injection heights for boreal fires in North America and Siberia primary between 1 km and 5 km (e.g., Lavoué et al., 2000; Stohl, 2006; Turquety et al., 2007; Leung et al., 2007; Val Martin et al., 2018). In view of having no better information, the footprint layer for vegetation fires is here defined between 1 km and 5 km.

2.2 Industrial sources and flaring

The Nightfire product from VIIRS offers quantitative estimates of infrared source emission temperatures by taking advantage of absent solar reflectance in short-wave infrared spectral range during night (Elvidge et al., 2013, 2016). Emission temperatures typically exhibit bimodal distributions by a combination of gas flares dominating the upper mode (peaking in the 1600 - 2000 K range) and other industrial heat sources as well as vegetation fires dominating the lower mode (peaking in the 800 - 1200 K range; Elvidge et al., 2016; Liu et al., 2018). Thus, temperature distributions of vegetation fires and industrial sources can overlap, depending on the industry sector and the vegetation type. However, vegetation fires at mid- to northern latitudes exhibit a clear seasonality with minimum occurrence between November and January (e.g., Giglio et al., 2013). Consequently, this analysis took advantage of both emission temperatures and seasonality to differentiate between the presence of industrial
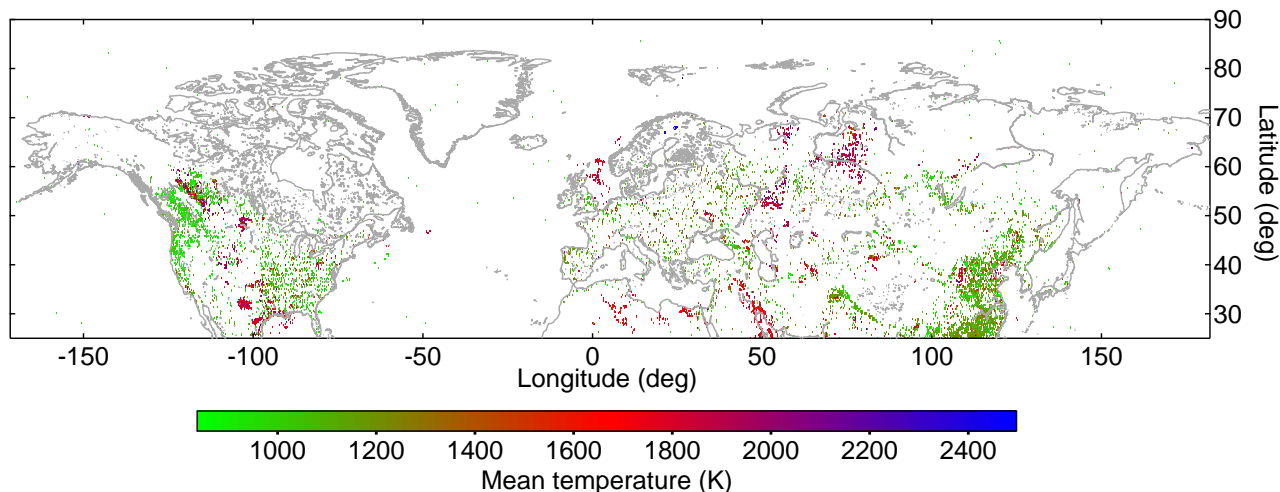
Figure S3. Map showing the mean infrared emission temperatures of industrial heat sources for November 2013 until January 2014.

hot spots and vegetation fires (Elvidge et al., 2013; Liu et al., 2018). VIIRS Nightfire data were thus downloaded for November 2013 until January 2014 and for latitudes north of 25 °N (NOAA, 2018a). Data points were projected on the gridded map by averaging temperatures in each grid cell (Fig. S3). Industrial hot spots were identified by both pixel mean temperature larger than 840 K[1] as well as one or more observations per grid cell within the respective time, owing to source persistence (Fig. 4b). Gas flares can be clearly detected by VIIRS Nightfire emission temperatures between 1600 K and 2000 K (Fig. S3) independent on season (Elvidge et al., 2016). Based on this temperature definition, VIIRS Nightfire provide the so-called *Flares only* product (NOAA, 2018b). Data between 30 March and 13 May 2014[2], were projected on the gridded map by adding up observations in each grid cell. Flares were identified by more than one observation per grid cell within the respective time, owing to source persistence (Fig. 4c).

Both approaches look reasonable by comparing Figs. 4b and c with Fig. 8 in Elvidge et al. (2016) and Fig. 8 in Liu et al. (2018). Oil/gas- and coal-related plants in northwestern Siberia (near Norilsk and Novy Urengoy), northern Europe (North Sea, Norwegian Sea, and Nenets region) and Alaska (Prudhoe Bay) can be clearly identified (Figs. 4b and c). However, uncertainties remain by non-continuously operating industrial sources.

2.3 Population

Populated areas provide anthropogenic emissions from residential heating, transportation, cooking etc. The criteria for the grid cell to be classified as populated is given by more than 1000 people live in a 0.25° x 0.25° area. Geolocational data on population are provided online (MaxMind, 2018). Densely populated regions in central Europe and coastal North American can be clearly identified, whereas Northern Canada, Alaska, and Siberia present sparsely populated regions (Fig. 4d).

2.4 Arctic natural marine sources

Sea ice coverage in July 2014 is assessed to obtain areas of open water in the Arctic. The Special Sensor Microwave Imager/Sounder (SSMIS) onboard the Defense Meteorological Satellite Program (DMSP) provides data on sea ice coverage, based on brightness temperature (Cavalieri et al., 1996, updated yearly). Data represent the fractional amount of sea ice covering a 25 x 25 km grid cell in a polar stereographic projection. Polar stereographic coordinates were converted to geodetic

---

[1]840 K presents the lowest mean temperature for industrial sites, indicative for nonmetal-mineral producing plants (Liu et al., 2018).

[2]Data earlier in 2014 are not available and high latitude data later than May are not valuable due to 24 h solar irradiance.

latitude and longitude for polar regions (Snyder, 1982)[3]. The obtained data grid was synchronized with the gridded map by averaging concentrations in each grid cell. Arctic open water is defined by both sea ice concentrations less than 30 % and latitudes north of 73.5° N (Fig. 4e).

3 Representativeness of the July 2014 measurement periods

It is of relevance to assess the representativeness of both NETCARE 2014 periods with respect to climatological conditions, i.e. mean conditions between 1981 - 2010. Climatic anomalies were obtained by using re-analysis data prepared by NCEP/NCAR (Kalnay et al., 1996). Images in Fig. S4 were provided by the NOAA/ESRL Physical Sciences Division, Boulder Colorado, from their web site at http://www.esrl.noaa.gov/psd/data/composites/day/ (Kalnay et al., 1996).

The synoptic situation with the high pressure influence during the Arctic air mass period was generally consistent with the climatology. First, 850 hPa geopotential heights were within +20 m of the climatology in the measurement region (Fig. S4a). Second, air temperatures at 850 hPa were maximum 1 K lower than normal (Fig. S4c). Third, the precipitation anomaly was negligible small (Fig. S4e). Finally, local meteorological conditions, such as the shallow stable stratified BL and low wind speeds (see Sect. 3.2.1), represented typical features in the summertime Arctic atmosphere (e.g., Fuelberg et al., 2010; Tjern-ström et al., 2012).

In contrast to this, the southern air mass period with influences of the low-pressure system centered south of Resolute Bay were significantly anomalous compared to climatological mean. Geopotential height at 850 hPa shows a climatological departure down to -120 m close to the center of the low-pressure system (Fig. S4b). Further, warmer air than normal was advected into and more precipitation than normal fell in the measurement region (Figs. S4d and f). Air temperatures at 850 hPa deviated up to +6 K from the climatology in the region north-east of the Hudson Bay (Fig. S4d). Additionally, the vegetation fire activity in North America was anomalously high in summer 2014 compared to 2001 - 2013 (Arndt et al., 2015). Together, influences of vegetation fires on Arctic atmospheric composition were larger than on climatological average caused by a combination of anomalous meteorological conditions and intensive fires in northern Canada.

4 Levoglucosan and Potassium Sulfate

Levoglucosan (or 1,6-anhydro-beta-glucopyranose; $C_6H_{10}O_5$) is a key organic tracer for vegetation fires (Simoneit et al., 1999). However, there is no consensus in SPMS literature about ion markers of levoglucosan. The averaged laboratory mass spectrum by Silva et al. (1999) shows ion peaks at m/z -45, -59 and -71, while others also used m/z -73 to identify levoglucosan in ambient mass spectra (Moffet et al., 2008; Corbin et al., 2012). Consequently, ALABAMA laboratory measurements were conducted to identify mass spectra characteristics of levoglucosan.

Levoglucosan is poorly absorbing at 266 nm laser wavelength as found in this laboratory study. Therefore, the better absorbing material KSO_4 was mixed with levoglucosan. Both substances were suspended in purified water and nebulized with an aerosol generation system. Diffusion dryers filled with silica gel removed water from the particles and the resulting particles were introduced into the ALABAMA. Analogous to levoglucosan mixed with KSO_4, KSO_4 was separately analyzed to differentiate ion peaks originating from levoglucosan and KSO_4.

The mean mass spectrum of KSO_4 is characterized by molecular ion peaks at m/z -135/137 (Fig. S5). It further shows potassium peaks at m/z +39/41 as well as several fragments that contain sulfur and/or oxygen (m/z -96/98, -80, -64, -48, -21, and -16). In parallel, the mean mass spectrum of levoglucosan is obtained by subtracting the mean spectrum of KSO_4 from levoglucosan mixed with KSO_4 (Fig. S6). As a result, levoglucosan is characterized by fragments at m/z -71, -59, -45, confirming laboratory measurements by Silva et al. (1999). Additional fragments at m/z -58, -41, and -25 have been also reported by Silva et al. (1999), albeit not dominant in their study. However, these mass spectral characteristics are not unambiguous owing to isobaric interferences with fragments of other oxygen-containing organic compounds (Table S1). It is thus difficult to clearly identify levoglucosan in ambient particle mass spectra.

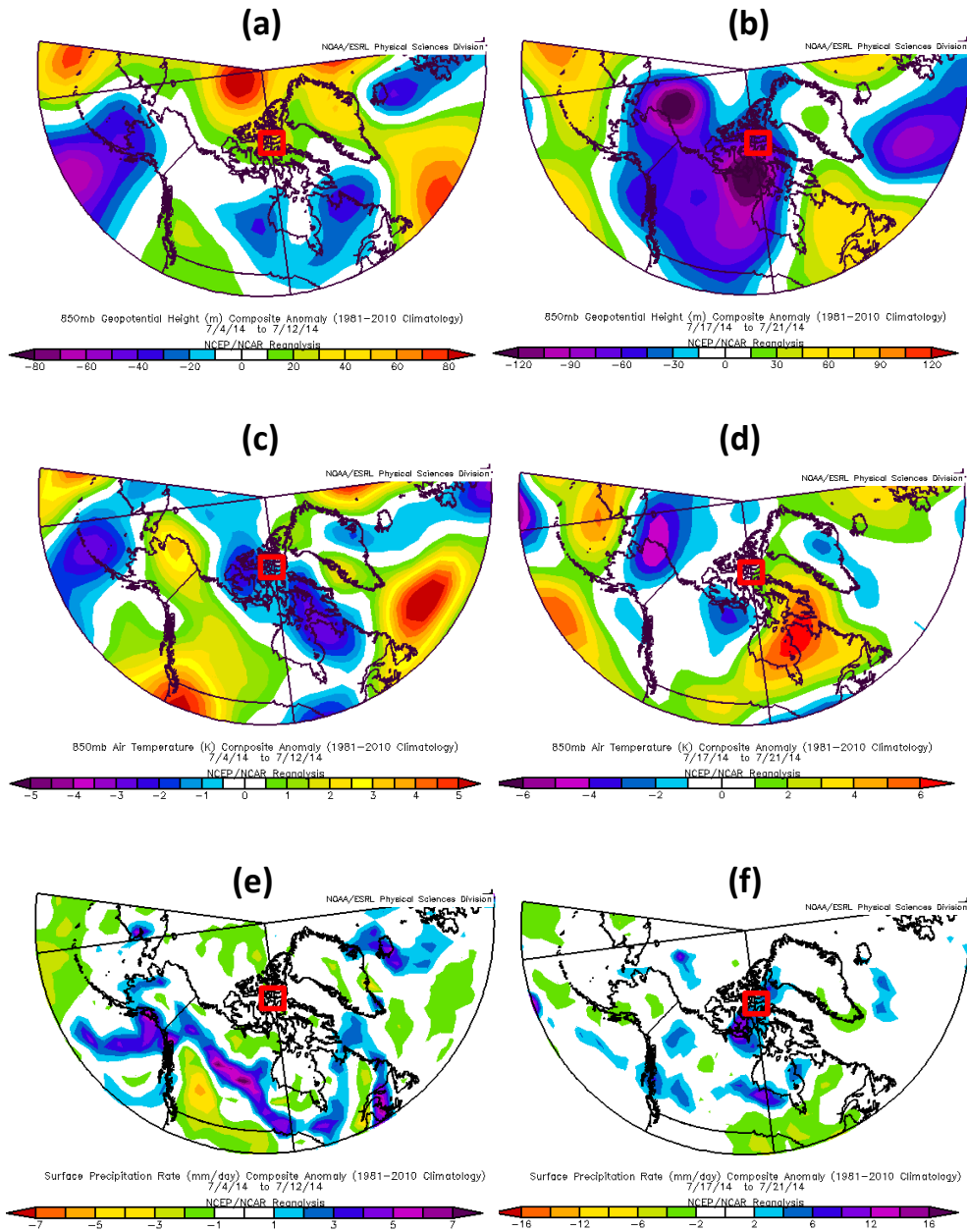[3]Source code was taken from ftp://sidads.colorado.edu/pub/DATASETS/seaice/polar-stereo/tools/mapxy.for.

Figure S4. Anomaly from climatological mean (1981 - 2010) of 850 hPa geopotential height (a-b), 850 hPa air temperature (c-d), and 850 hPa precipitation rate (e-f) during the Arctic air mass period (left panel) and the southern air mass period (right panel). The measurement region is marked with a red box.
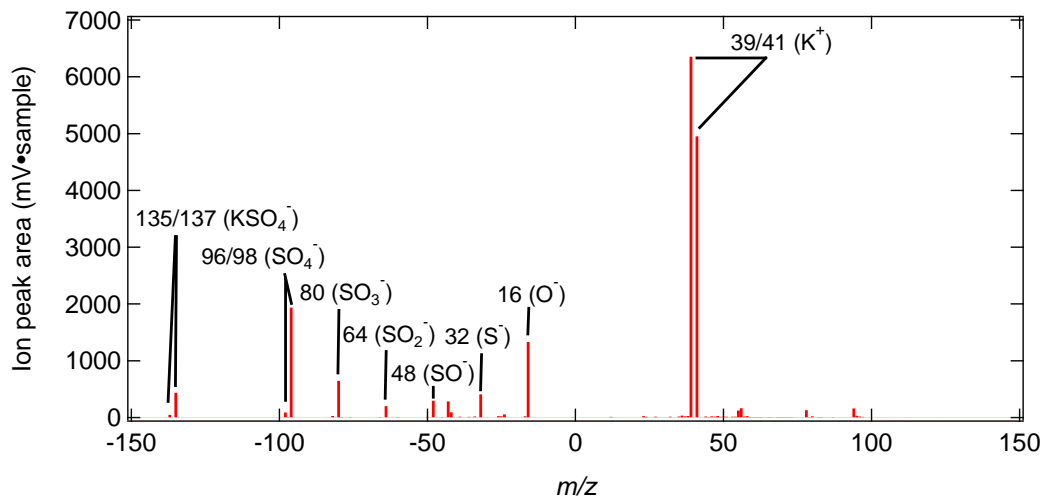
Figure S5. Potassium sulfate (KSO_4) mean bipolar spectrum of 69 single particle spectra analyzed by the ALABAMA. The isotopic ratio of potassium at m/z +41 and m/z +39 is too high, likely caused by saturation effects of the MCP.
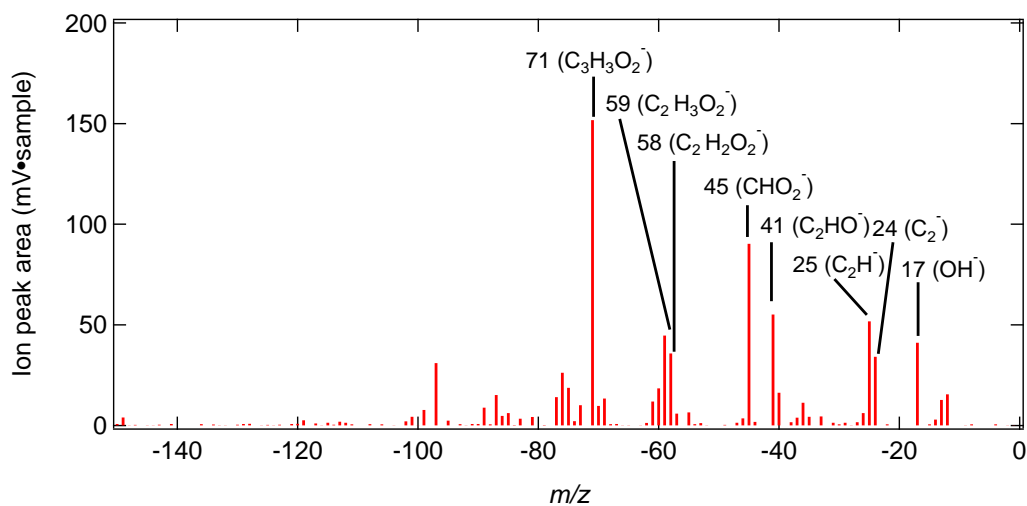
Figure S6. Mean anion spectrum of levoglucosan, obtained as the difference between the mean spectrum of levoglucosan with KSO_4 (average of 754 single particle spectra analyzed by the ALABAMA) and the pure KSO_4 mean spectrum (see Fig. S5).

Table S1. Organic compounds showing isobaric interferences with fragments of levoglucosan.

Compounds	Ion markers	References
Acetic acid	m/z -59	Lee et al. (2003); Brands et al. (2011)
Methylglyoxal	m/z -71,	Zauscher et al. (2013)*
	m/z -59	Zauscher et al. (2013)*
Acrylate	m/z -71	Zauscher et al. (2013)*
Glyoxylic acid	m/z -73	Lee et al. (2003); Zauscher et al. (2013)
Polycyclic aromatic hydrocarbons	m/z -25	Silva and Prather (2000)
Polycyclic aromatic hydrocarbons	m/z -41	Silva and Prather (2000)
-cont. alkohol functional groups	m/z -41	Silva and Prather (2000)
Formic acid	m/z -45	Lee et al. (2003)
Ethoxide	m/z -45	Lee et al. (2003)
n-propoxide	m/z -59	Lee et al. (2003)
Propanoic acid	m/z -73	Lee et al. (2003)

*Zauscher et al. (2013, Supplement) further reported that most oxygen-containing organic standards show small ion peaks at m/z -45 and m/z -59.

5 Internal mixing of particle types

The internal mixing state of the ALABAMA particle types is given in Table S2. Additionally, the expanded mean anion spectrum of those sea spray particles that are internally mixed with DCA compounds are shown in Fig. S7. The remaining particles in Fig. 5 (gray filling) are further sub-classified with marker species: ammonium, methanesulfonic acid, and sulfate (see Fig. S8). Figure S9 depicts the bipolar mean spectrum of particles that could not classified with the marker species, so-called "Others".

Table S2. Particle types and their internal mixing with other substances derived from the mean spectra in Fig. 6. Additional ion signals of sulfate (m/z -97/99 (HSO_4^-), -96 (SO_4^-)) and potassium (m/z +39/41 (K^+)) were present in every mean spectrum and have therefore not been listed here. References from SPMS laboratory and field studies are indicated by numbers that are defined below. These references are used for the assignment of the additional ion signals to the corresponding substances.

Particle type denotation	Ion markers	Additional ion signals in mean spectrum	Corresponding substances
Na/Cl/ Nitrate -containing	m/z +23 (Na^+), +46 (Na_2^+), +62 (Na_2O^+), +63 (Na_2OH^+) +81/83 (Na_2Cl^+) m/z -35/37 (Cl^-), -46 (NO_2^-), -62 (NO_3^-), -93/95 $(NaCl_2^-)$	m/z +24/25/26 (Mg^+), +40 (Ca^+), +56 (CaO^+) m/z -26 (CN^-), -42 (CNO^-), -45 (CHO_2^-), -59 $(C_2H_3O_2^-)$, -71 $(C_3H_3O_2^-)$, -73 $(C_3H_5O_2^-)$ -89 $(C_2HO_4^-)$	magnesium[1,2] calcium[1] nitrogen-cont. OM[1,2,3] oxygen-cont. OM[3,4,5] oxalic acid[9]
EC -containing	m/z +12, +24,..., +84 (C_{1-7}^+) m/z -12, -24,..., -96 (C_{1-8}^-)	m/z -26 (CN^-), -42 (CNO^-), -45 (CHO_2^-), -59 $(C_2H_3O_2^-)$, -73 $(C_3H_5O_2^-)$, -89 $(C_2HO_4^-)$, -95 $(CH_3O_3S^-)$, -46 (NO_2^-), -62 (NO_3^-)	nitrogen-cont. OM[6] oxygen-cont. OM[8,10] oxalic acid[9] MSA[9] nitrate[9]
nss-nitrate -containing	m/z -46 (NO_2^-), -62 (NO_3^-)	m/z -26 (CN^-), -42 (CNO^-), -45 (CHO_2^-), -59 $(C_2H_3O_2^-)$, -73 $(C_3H_5O_2^-)$, -89 $(C_2HO_4^-)$	nitrogen-cont. OM[6] oxygen-cont. OM[8,10] oxalic acid[9]
TMA -containing	m/z +59 $((CH_3)_3N^+)$, +58 $(C_3H_8N^+)$	m/z +18 (NH_4^+), +12, ..., +36 (C_{1-3}^+), +27 $(C_2H_3^+/CHN^+)$, +37 (C_3H^+), +43 $(C_3H_7^+/CH_3CO^+/CHNO^+)$ m/z -95 $(CH_3O_3S^-)$	ammonium[9] carbon cluster ions[9] hydrocarbons[7] oxidized organics[7] MSA[9]
DCA -containing	m/z -89 $(C_2HO_4^-)$, -103 $(C_3H_3O_4^-)$, -117 $(C_4H_5O_4^-)$	m/z +27 $(C_2H_3^+/CHN^+)$, m/z -26 (CN^-), -42 (CNO^-), -45 (CHO_2^-), -59 $(C_2H_3O_2^-)$, -73 $(C_3H_5O_2^-)$	hydrocarbons[7] nitrogen-cont. OM[6] oxygen-cont. OM[8,10]
sub-K -containing	m/z +39/41 (K^+)	m/z +18 (NH_4^+), +12, ..., +36 (C_{1-3}^+), +27 $(C_2H_3^+/CHN^+)$, +37 (C_3H^+), +43 $(C_3H_7^+/CH_3CO^+/CHNO^+)$ m/z -95 $(CH_3O_3S^-)$	ammonium[9] carbon cluster ions[9] hydrocarbons[7] oxidized organics[7] MSA[9]

Given reference numbers are defined as follows: [1]Prather et al. (2013),[2]Guasco et al. (2014),[3]Pratt et al. (2009),[4]Schmidt et al. (2017),[5]Trimborn et al. (2002),[6]Silva et al. (1999),[7]Schmidt (2015), [8]Zauscher et al. (2013),[9]see Table 1, [10]Lee et al. (2003).
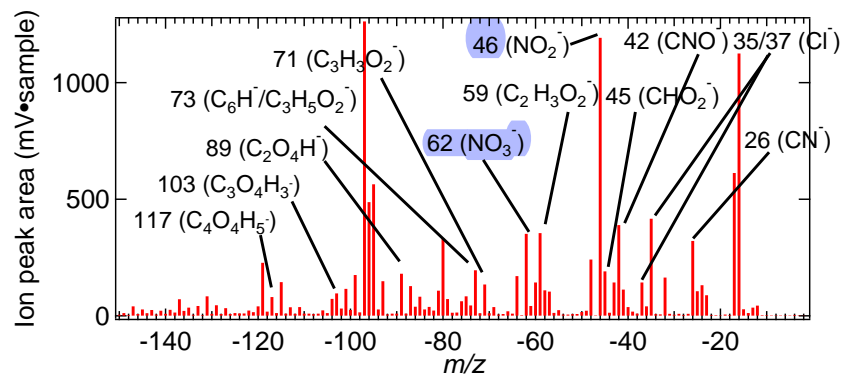
Figure S7. Expanded mean anion spectrum of sea spray particles containing DCA, presenting 60% of all sea spray particles in Fig. 6a.
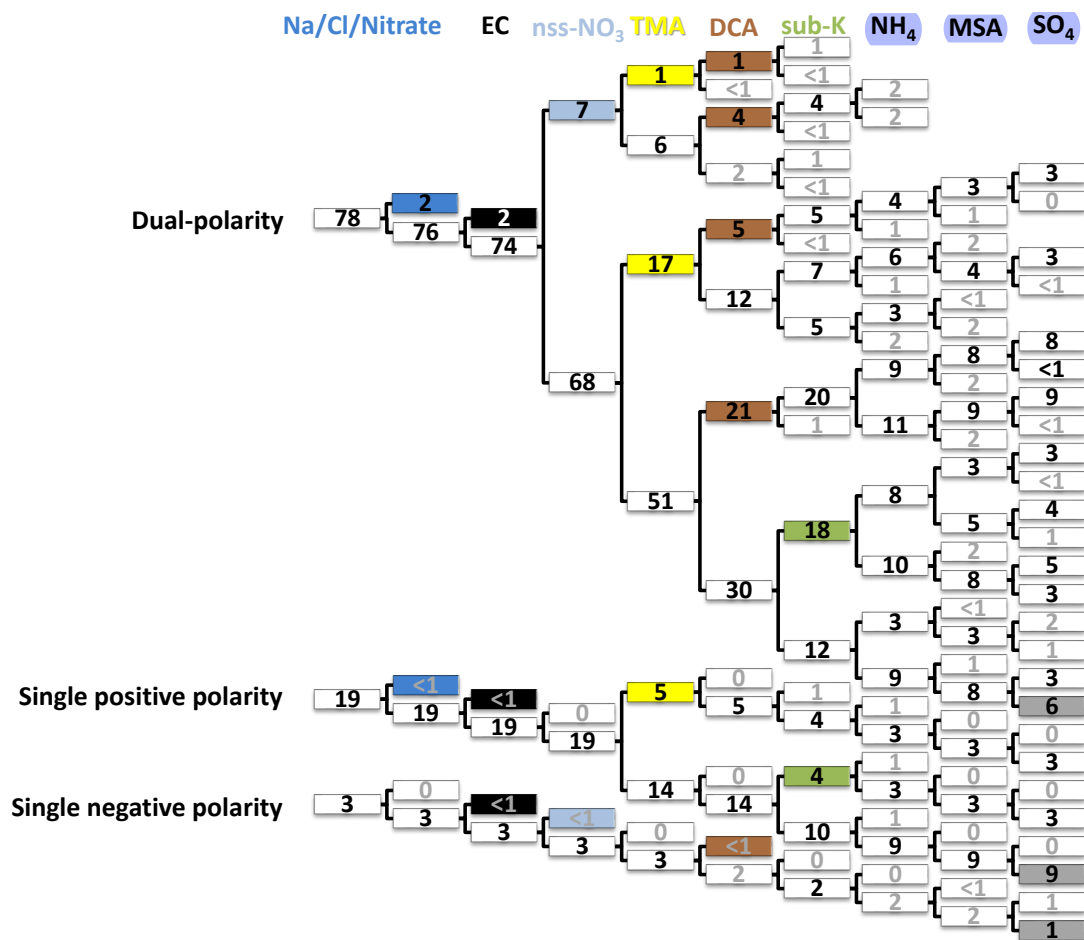
Figure S8. Classification of 10137 single particle spectra based on the ion marker method and illustrated with the decision tree. Upper/lower branches refer to the presence/absence of substances in the particle mass spectra. Numbers are given as relative abundances in % normalized to 10137 particles. The initial classification provides three groups of particle mass spectra with dual-, single positive, and single negative polarity. Particle types, indicated by colors, contain: Na/Cl/Nitrate (dark blue), EC (black), non-sea-spray-(nss)-NO$_3$ (light blue), trimethylamine (TMA) (yellow), dicarboxylic acids (DCA) (brown), and potassium (sub-K) (green). The remaining particles are further sub-classified by the abundance of ammonium (NH$_4$), methanesulfonic acid (MSA), and sulfate (SO$_4$). 16 % of all mass spectra could not be classified with the marker species, summarized as "Others" and marked with a gray filling.
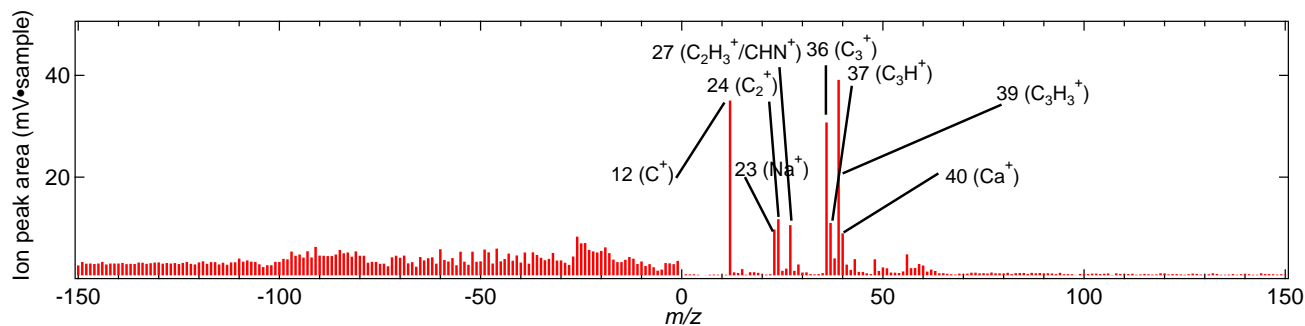
Figure S9. Bipolar mean spectrum of the 1618 particles (16 % of all mass spectra analyzed by the ALABAMA) that could not classified with the marker species (see gray filling in Fig. S8). These particles are therefore summarized as "Others".
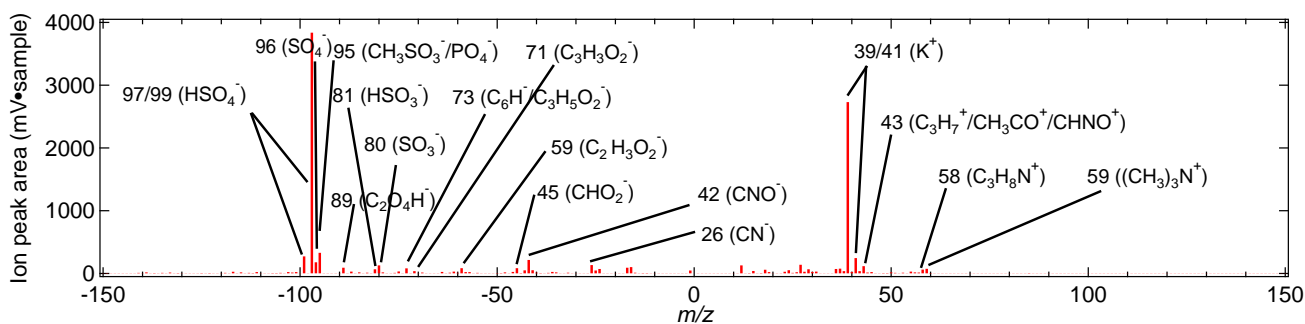
Figure S10. Bipolar mean spectrum of particles that show internal mixing of DCA, TMA, and MSA (14 % of all DCA-containing particles, 4 % of all mass spectra analyzed by the ALABAMA).

6 Additional figures

Figures S11 - S15 are associated with the discussion in Sections 3.2.2-3.2.3 and 3.3.2 in the main document. Size distributions of the ALABAMA particle types are given in Fig. S11.
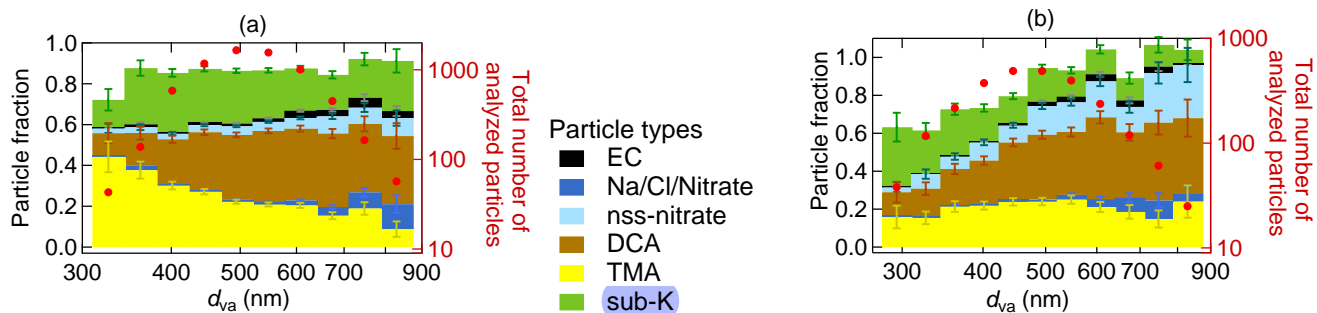
Figure S11. Size-resolved aerosol composition of the ALABAMA particle types during the Arctic (a) and southern (b) air mass periods. Both figures represent the cumulative particle fraction of: EC-containing (black), nss-nitrate-containing (light blue), DCA-containing (brown), Na/Cl/Nitrate-containing (dark blue), TMA-containing (yellow), and sub-K-containing (green) particles as well as the total number of analyzed particles per bin (red). Uncertainty analysis is given in the Supplement Sect. 7.
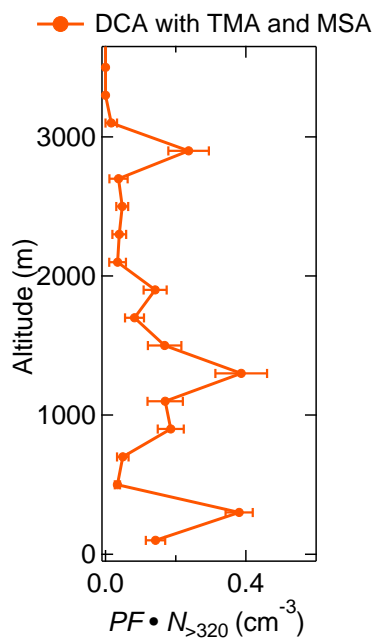
Figure S12. Vertically resolved aerosol composition measured by the ALABAMA during the Arctic air mass period. The panel represents the ALABAMA scaled number concentration ($PF \cdot N_{>320}$) of particles that show internal mixing of DCA, TMA, and MSA. Uncertainty analyses are given in the Supplement Sect. 7.
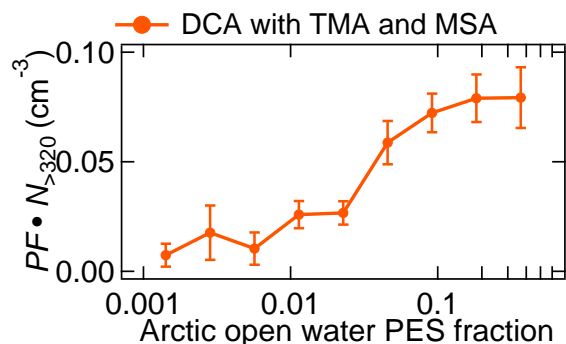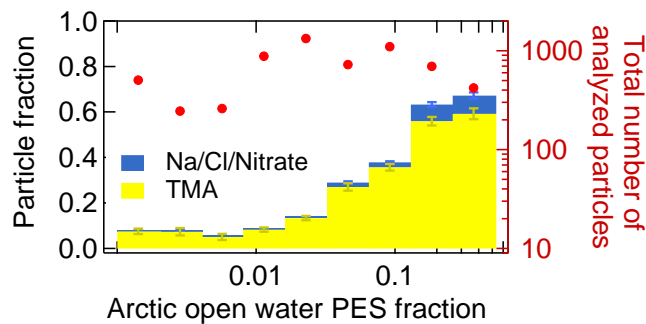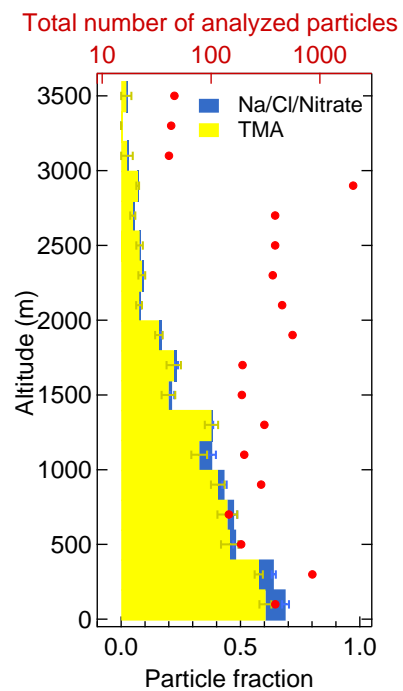
Figure S13. Aerosol composition measured by the ALABAMA as a function of FLEXPART derived PES fraction over Arctic open water areas during the Arctic air mass period. The panel represents the ALABAMA scaled number concentration ($PF \cdot N_{>320}$) of particles that show internal mixing of DCA, TMA, and MSA. Uncertainty analyses are given in the Supplement Sect. 7.
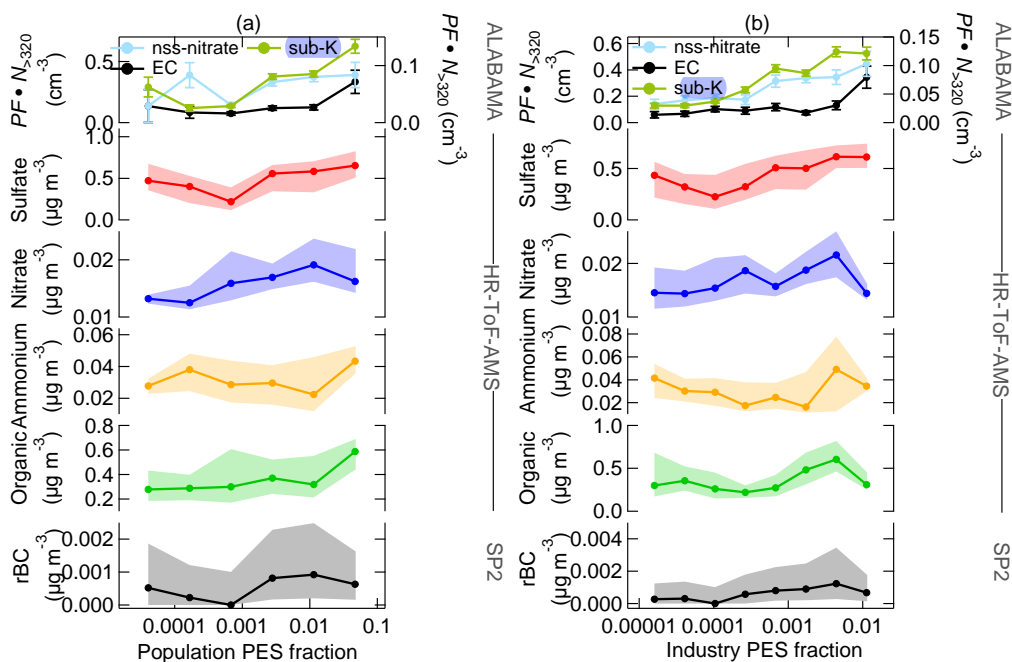
Figure S14. Aerosol composition measured by the ALABAMA and by the HR-ToF-AMS (indicated on the right side) as a function of FLEXPART derived PES fraction over (a) populated areas and (b) industrial areas during the Arctic air mass period. Top panel represents the ALABAMA scaled number concentration ($PF \cdot N_{>320}$) with right axis referring to EC (black)- and nss-nitrate (light blue)-containing particles and left axis referring to sub-K-containing (green) particles. Lower panels represent each median (solid line with marker) and interquartile ranges (shaded area) of the HR-ToF-AMS mass concentrations of sulfate (red), nitrate (blue), ammonium (orange), and organic matter (light green) as well as rBC measured by the SP2 (black). Uncertainty analyses are given in the Supplement Sect. 7.
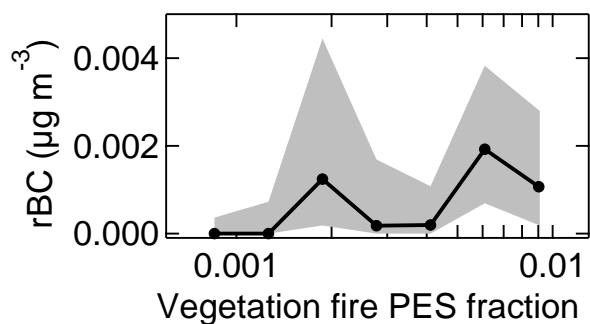
Figure S15. Refractory black carbon (rBC) measured by the SP2 as a function of FLEXPART derived PES fraction over vegetation fires during the southern air mass period. The figure represents median (solid line with marker) and interquartile ranges (shaded area). Uncertainty analyses are given in the Supplement Sect. 7.

Figures S16-S24 provide the cumulative fraction of the ALABAMA aerosol composition, associated with figures of the scaled number concentration in the main document.

Figure S16. Aerosol composition measured by the ALABAMA as a function of FLEXPART derived PES fraction over Arctic open water areas during the Arctic air mass period. The figure represents the cumulative particle fraction of TMA-containing (yellow) and Na/Cl/Nitrate-containing (blue) particles as well as the total number of analyzed particles per bin (red). Uncertainty analyses are given in the Supplement Sect. 7.

Figure S17. Vertically resolved aerosol composition measured by the ALABAMA during the Arctic air mass period. The figure represents the cumulative particle fraction of TMA-containing (yellow) and Na/Cl/Nitrate-containing (blue) particles as well as the total number of analyzed particles per bin (red). Uncertainty analyses are given in the Supplement Sect. 7.
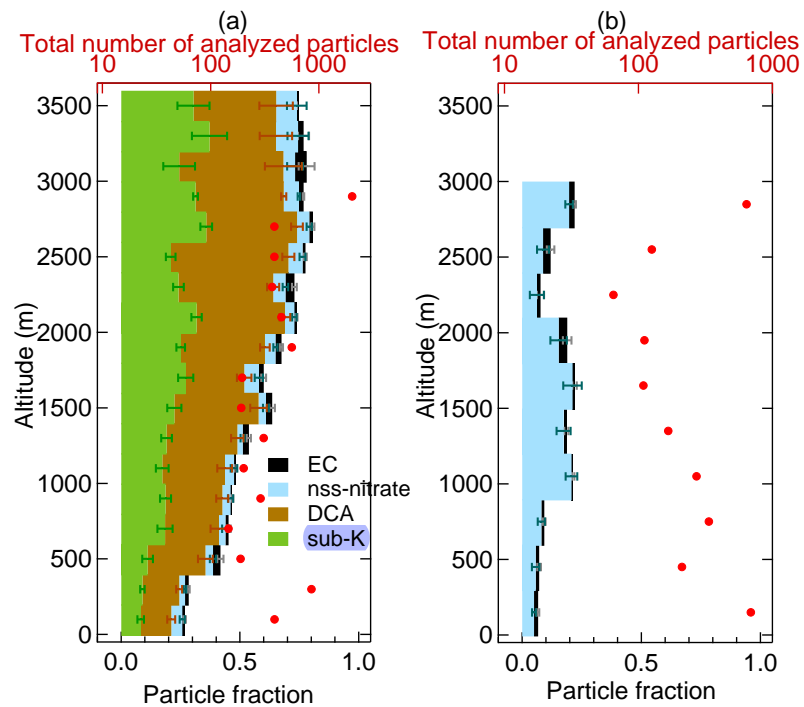
Figure S18. Vertically resolved aerosol composition measured by the ALABAMA during (a) the Arctic air and (b) the southern air mass periods. Figures represent the cumulative particle fraction of DCA- (brown), nss-nitrate- (blue), EC- (black), and sub-K-containing (green) particles as well as the total number of analyzed particles per bin (red). Uncertainty analyses are given in the Supplement Sect. 7.
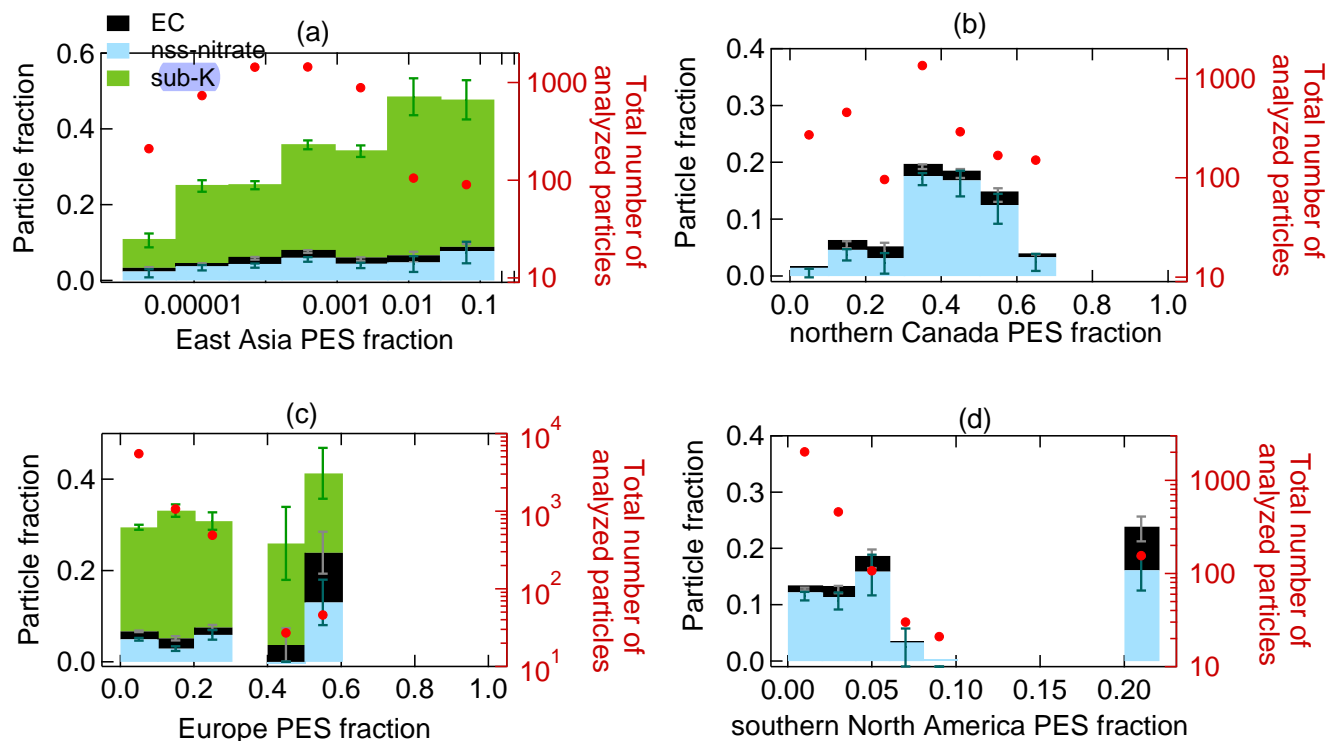
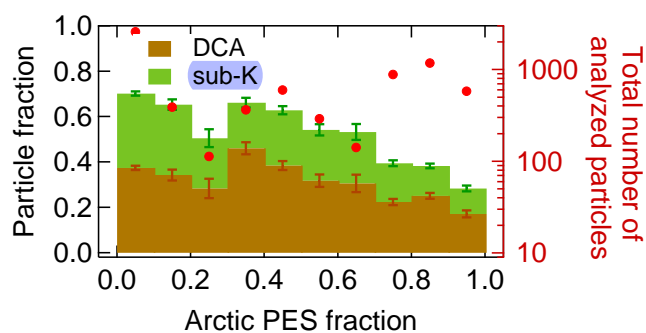**Figure S19.** Aerosol composition measured by the ALABAMA as a function of FLEXPART derived PES fraction over the East Asia (a), northern Canada (b), Europe (c), and southern North America (d) during the Arctic (a,c) and the southern air mass (b,d) periods. Figures represent each the cumulative particle fraction of EC- (black), nss-nitrate- (light blue), and sub-K-containing (green) particles as well as the total number of analyzed particles per bin (red). Uncertainty analyses are given in the Supplement Sect. 7.
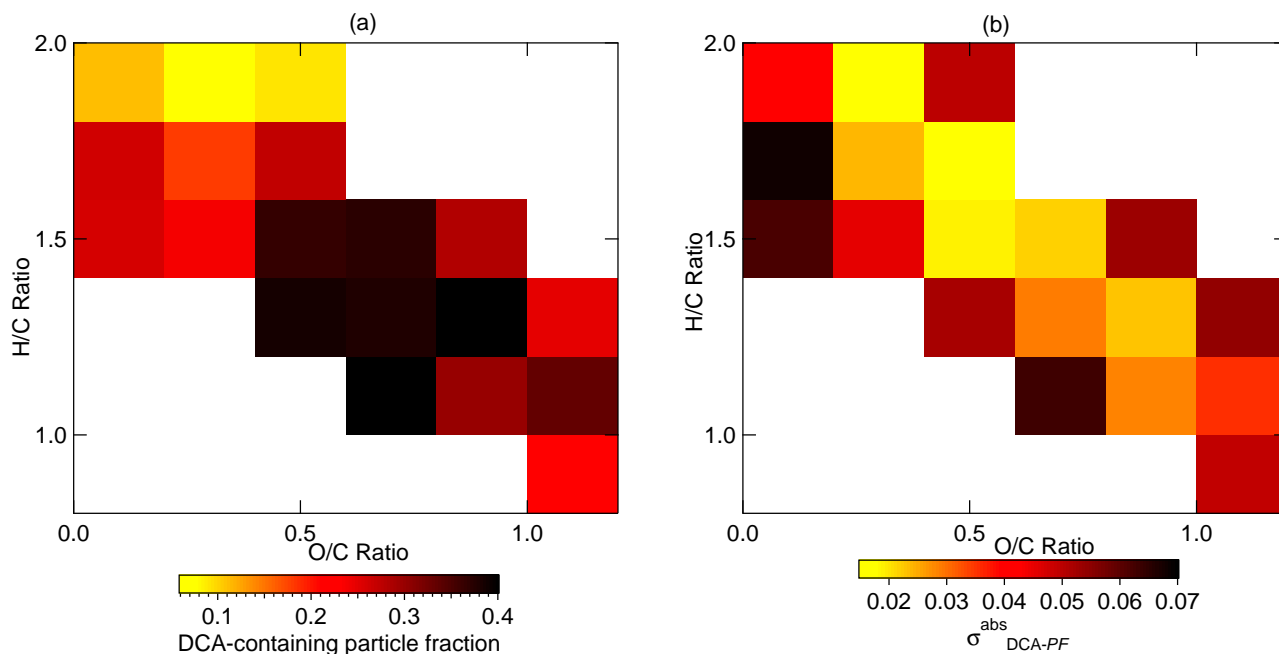
Figure S20. Comparison between the HR-ToF-AMS estimated oxygen-to-carbon (O/C) and hydrogen-to-carbon (H/C) ratios colored by (a) the particle fraction of DCA-containing measured by the ALABAMA and (b) the absolute uncertainty of the particle fraction. Uncertainty analyses are given in Sect. 7.

Figure S21. Aerosol composition measured by the ALABAMA as a function of FLEXPART derived PES fraction over Arctic regions during the Arctic air mass period. The figure represents the fraction of DCA- (brown) and sub-K-containing (green) particles as well as the total number of analyzed particles per bin (red). Uncertainty analysis is given in the Supplement Sect. 7.
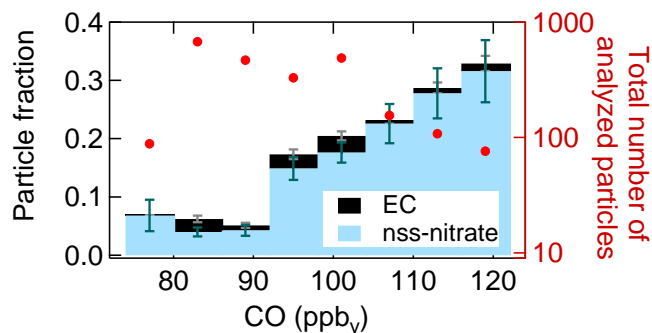
Figure S22. Aerosol composition measured by the ALABAMA as a function of CO mixing ratios during the southern air mass period. Figure represents the cumulative particle fraction of nss-nitrate-containing (blue) and EC-containing (black) particles as well as the total number of analyzed particles per bin (red). Uncertainty analyses are given in the Supplement Sect. 7.
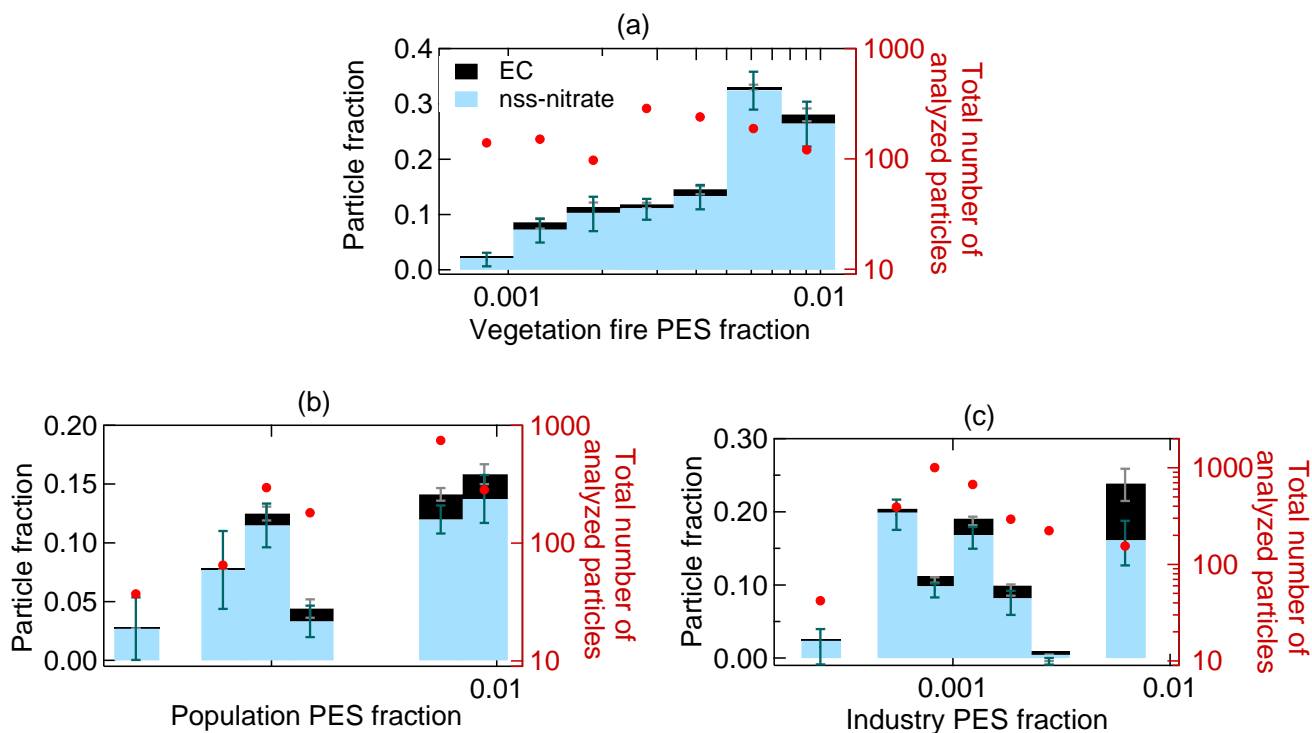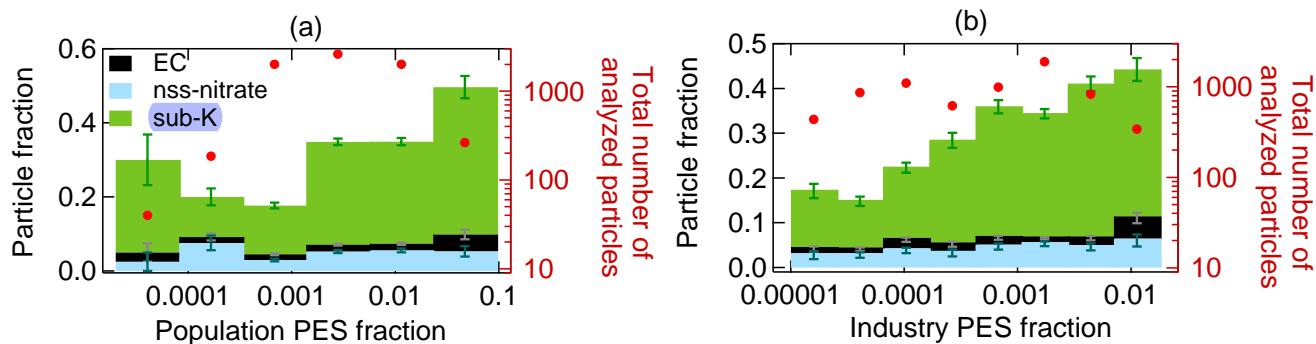

Figure S23. Aerosol composition measured by the ALABAMA as a function of FLEXPART derived PES fraction over (a) vegetation fires, (b) populated areas, and (c) industrial areas during the southern air mass period. Figures represent each the cumulative particle fraction of nss-nitrate-containing (blue) and EC-containing (black) particles as well as the total number of analyzed particles per bin (red). Uncertainty analyses are given in the Supplement Sect. 7.

Figure S24. Aerosol composition measured by the ALABAMA as a function of FLEXPART derived PES fraction over (a) populated areas and (b) industrial areas during the Arctic air mass period. Figures represent each the cumulative particle fraction of nss-nitrate-containing (blue), EC-containing (black), and sub-K-containing (green) particles as well as the total number of analyzed particles per bin (red). Uncertainty analyses are given in the Supplement Sect. 7.

Figures S25-S32 provide the comparison between the number concentration of particles larger than 320 nm ($N_{>320}$) measured by the UHSAS and various parameters.
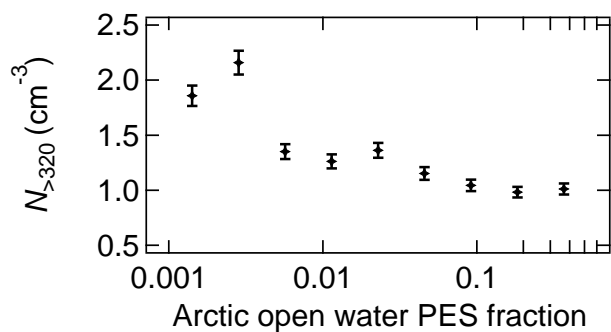

Figure S25. Averaged UHSAS number concentration in a size range between 320 and 870 nm ($N_{>320}$) as a function of FLEXPART derived PES fraction over Arctic open water areas during the Arctic air mass period. Uncertainty analysis is given in Sect. 7.
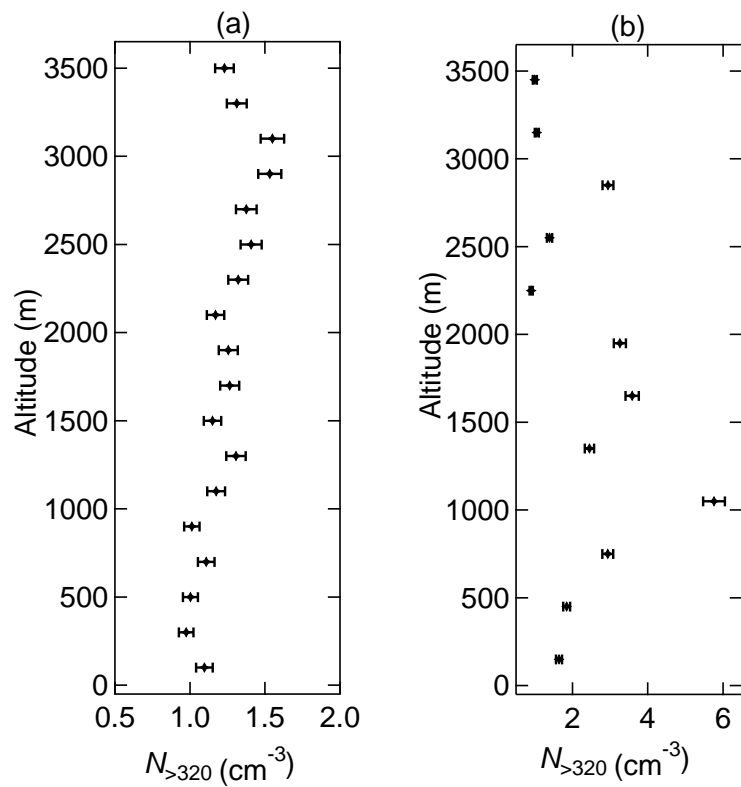
Figure S26. Vertically resolved averaged UHSAS number concentration in a size range between 320 and 870 nm ($N_{>320}$) during the Arctic (a) and the southern (b) air mass periods. Uncertainty analysis is given in Sect. 7.
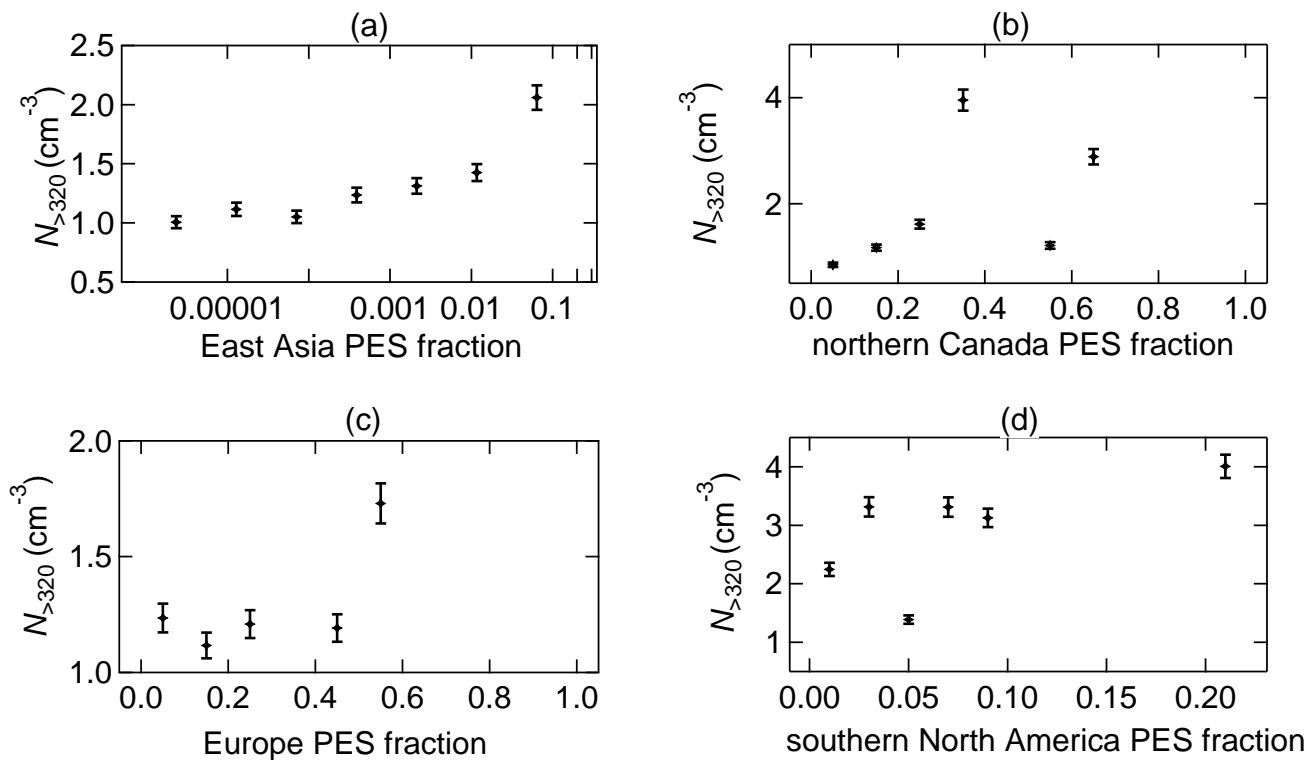
Figure S27. Averaged UHSAS number concentration in a size range between 320 and 870 nm ($N_{>320}$) as a function of FLEXPART derived PES fraction over the East Asia (a), northern Canada (b), Europe (c), and southern North America (d) during the Arctic (a, c) and the southern (b, d) air mass periods. Uncertainty analysis is given in Sect. 7.
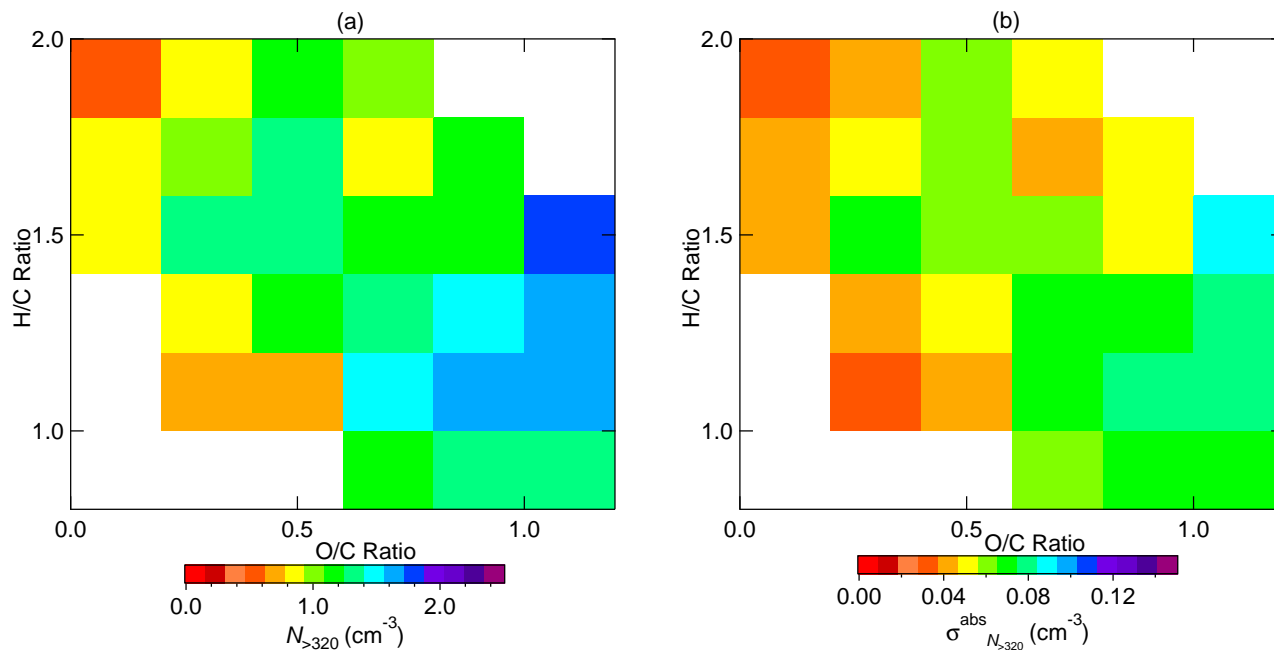
Figure S28. Comparison between the HR-ToF-AMS estimated oxygen-to-carbon (O/C) and hydrogen-to-carbon (H/C) ratios colored by (a) the averaged UHSAS number concentration in a size range between 320 and 870 nm ($N_{>320}$) and (b) the absolute uncertainty of $N_{>320}$ ($\sigma^{abs}_{N_{>320}}$). Uncertainty analysis is given in Sect. 7.
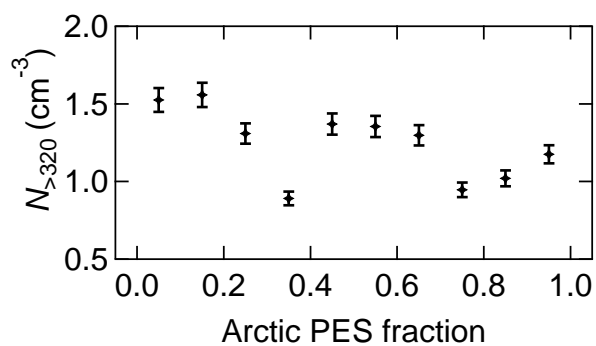

Figure S29. Averaged UHSAS number concentration in a size range between 320 and 870 nm ($N_{>320}$) as a function of FLEXPART derived PES fraction over the Arctic during the Arctic air mass period. Uncertainty analysis is given in Sect. 7.
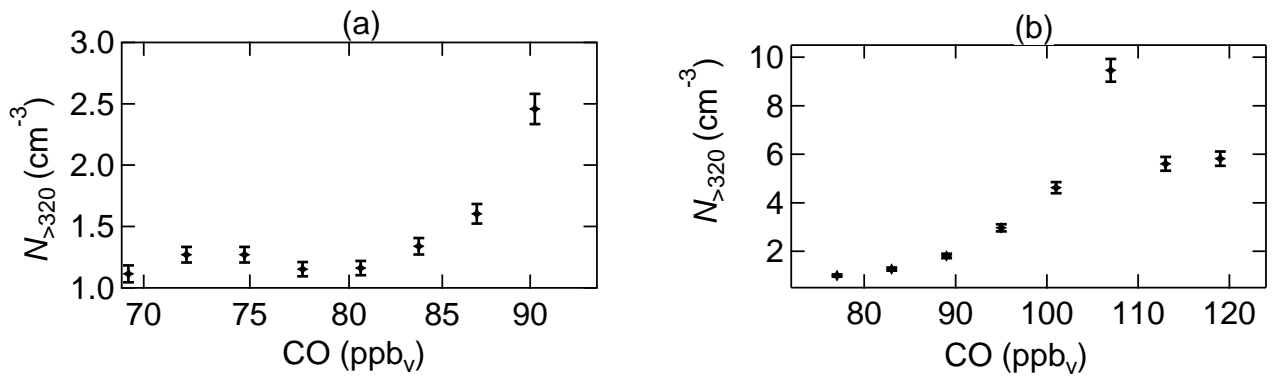
Figure S30. Averaged UHSAS number concentration in a size range between 320 and 870 nm ($N_{>320}$) as a function of CO mixing ratios during the Arctic (a) and the southern (b) air mass periods. Uncertainty analysis is given in Sect. 7.

Figure S31. Averaged UHSAS number concentration in a size range between 320 and 870 nm ($N_{>320}$) as a function of FLEXPART derived PES fraction over vegetation fires during the southern air mass period. Uncertainty analysis is given in Sect. 7.
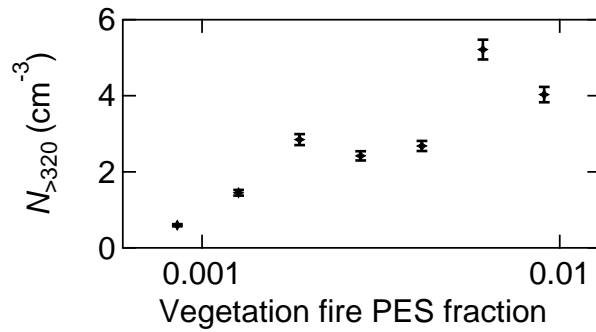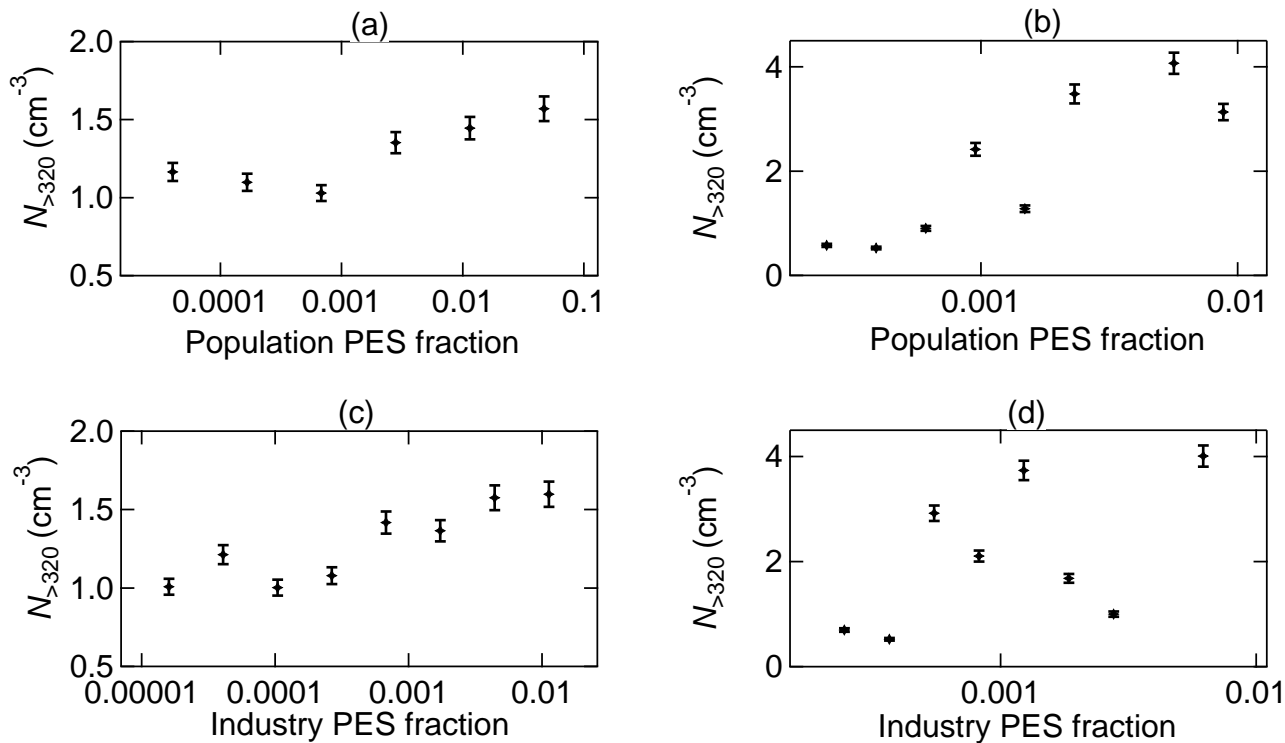
Figure S32. Averaged UHSAS number concentration in a size range between 320 and 870 nm ($N_{>320}$) as a function of FLEXPART derived PES fraction over populated areas (a-b) and industrial areas (c-d) during the Arctic (a, c) and the southern (b, d) air mass periods. Uncertainty analysis is given in Sect. 7.

7 Uncertainty analyses

7.1 UHSAS number concentration ($N_{>320}$)

The absolute uncertainty of the averaged UHSAS number concentration for each bin ($\sigma_{N_{>320}}^{\text{abs}}$) is calculated based on Poisson statistics and Gaussian propagation of uncertainties:

$$\sigma_{N_{>320}}^{\text{abs}} = N_{>320} \sqrt{\left(\sigma_{\text{UHSAS}}^{\text{rel}}\right)^2 + \left(\sigma_{\text{UHSAS}}^{\text{rel}_1}\right)^2}, \tag{3}$$

with the $\sigma_{\text{UHSAS}}^{\text{rel}}$ that is defined as follows:

$$\sigma_{\text{UHSAS}}^{\text{rel}} = \frac{1}{\sqrt{C_{>320}}}, \tag{4}$$

with the counts of particles greater than 320 nm in diameter ($C_{>320}$). The $\sigma_{\text{UHSAS}}^{\text{rel}_1}$ is 5 % derived from the UHSAS collection efficiency of 95 % (see Table S3).

7.2 ALABAMA particle fraction (PF)

The absolute uncertainty of the ALABAMA particle fraction for each bin (σ_{PF}^{abs}) is calculated using binomial statistics:

$$\sigma_{PF}^{\text{abs}} = \frac{\sqrt{N_{\text{hits}} \cdot PF \cdot (1 - PF)}}{N_{\text{hits}}}, \tag{5}$$

with the number of particles that are successfully ionized by the ablation laser and create a mass spectrum (N_{hits}) and the PF.

7.3 ALABAMA scaled number concentration ($PF \cdot N_{>320}$)

The absolute uncertainty of the ALABAMA scaled number concentration for each bin ($\sigma_{PF \cdot N_{>320}}^{\text{abs}}$) is calculated using Gaussian propagation of uncertainties:

$$\sigma_{PF \cdot N_{>320}}^{\text{abs}} = \sqrt{\left(PF \cdot \sigma_{N_{>320}}^{\text{abs}}\right)^2 + \left(N_{>320} \cdot \sigma_{PF}^{\text{abs}}\right)^2}. \tag{6}$$

7.4 Further information on complementary data

Table S3 presents further information on the instruments deployed in this study.

Table S3. Data and associated instrumentation used in this study along with additional information.

Instrument	Data used in this study [unit]	Particle size range[a]	Time resolution	T: total uncertainty R: reproducibility A: accuracy CE: collection efficiency DL: detection limits	Ref.	Operator
UHSAS	$N_{>320}$ [cm^{-3}] (STP)[b]	320 nm - 870 nm	1 s	CE: 95 %	c	AWI
HR-ToF-AMS	ammonium, sulfate, nitrate, OM, MSA [µg m^{-3}] (stdP)[e]	75 - 900 nm	20 - 30 s	DL: 0.004, 0.009, 0.008, 0.08, 0.005 µg m^{-3} T: 33 - 37 %	d	UofT
SP2	rBC [µg m^{-3}] (STP)[b]	85 - 700 nm	1 s	R: 10 %	f	AWI
ALABAMA	Na/Cl/Nitrate, EC, nss-nitrate, TMA, DCA [cm^{-3}] (STP)[h]	320-870 nm	non-equidistant time steps max. 8 Hz	see Sect. S7	g	MPI-C
CO analyzer	CO [ppbv]		1 s	T: 4.7 ppbv	i	IPA

[a]The upper particle size cut-off is approximately 1 µm owing to the particle transmission efficiency of the main aerosol inlet (Leaitch et al., 2016), although some instruments might have a higher upper cut-off.

[b]Data by the UHSAS and SP2 are presented at STP 273.15 K and 1013.25 hPa (Schulz et al., 2019)

[c]Cai et al. (2008); Schulz et al. (2019)

[d]DeCarlo et al. (2006); Bahreini et al. (2008); Willis et al. (2016, 2017)

[e]Data by the HR-ToF-AMS are presented at standard pressure (stdP) 1013.25 hPa, since no temperature measurements inside the inlet line are available.

[f]Schwarz et al. (2006); Gao et al. (2007); Laborde et al. (2012); Dahlkötter et al. (2014); Schulz et al. (2019)

[g]Brands et al. (2011); Roth et al. (2016); Köllner et al. (2017)

[h]Data by the ALABAMA are scaled to number concentrations using the UHSAS data that are presented at STP 273.15 K and 1013.25 hPa (Schulz et al., 2019)

[i]Scharffe et al. (2012); Aero-Laser GmbH (2013); Wandel (2015); Bozem et al. (2019)

Figure S33. FLEXPART 15-days integrated (a) partial column 0 - 400 m and (b) partial column 1 - 15 km potential emission sensitivity (PES; for measurements on 5 July from 19:00 until 19:10 UTC) as an example of transport from sources in East Asia (particularly Japan) to the measurement region.

8   Examples of transport pathways

Figures S33-S36 provide examples of transport pathways from East Asia, southern North America, Europe, and northern Canada to Arctic regions, respectively.
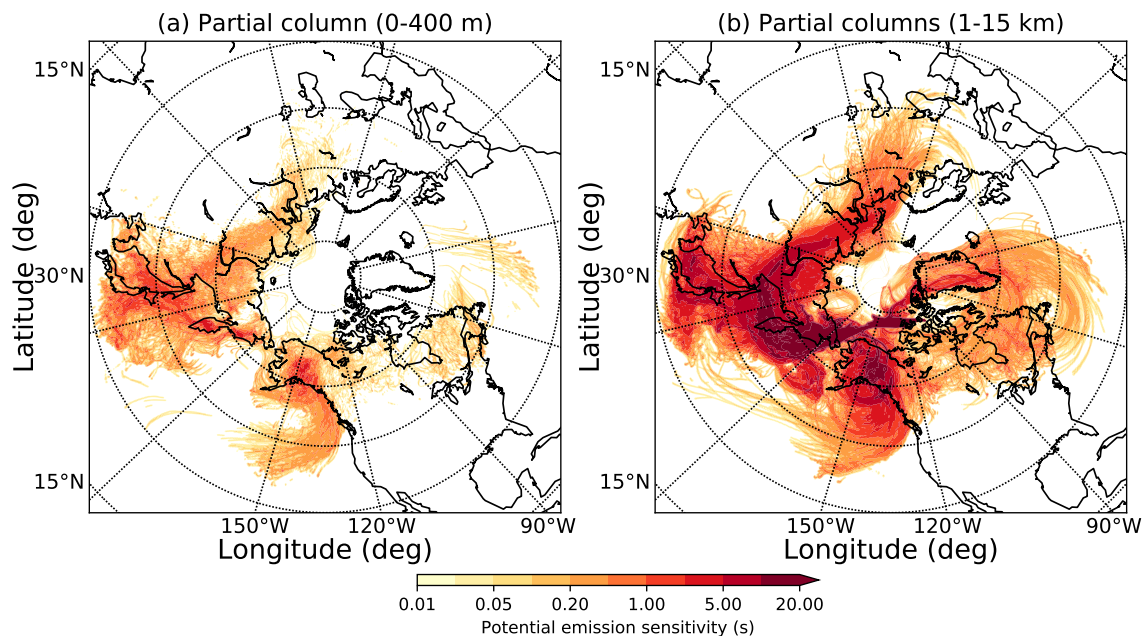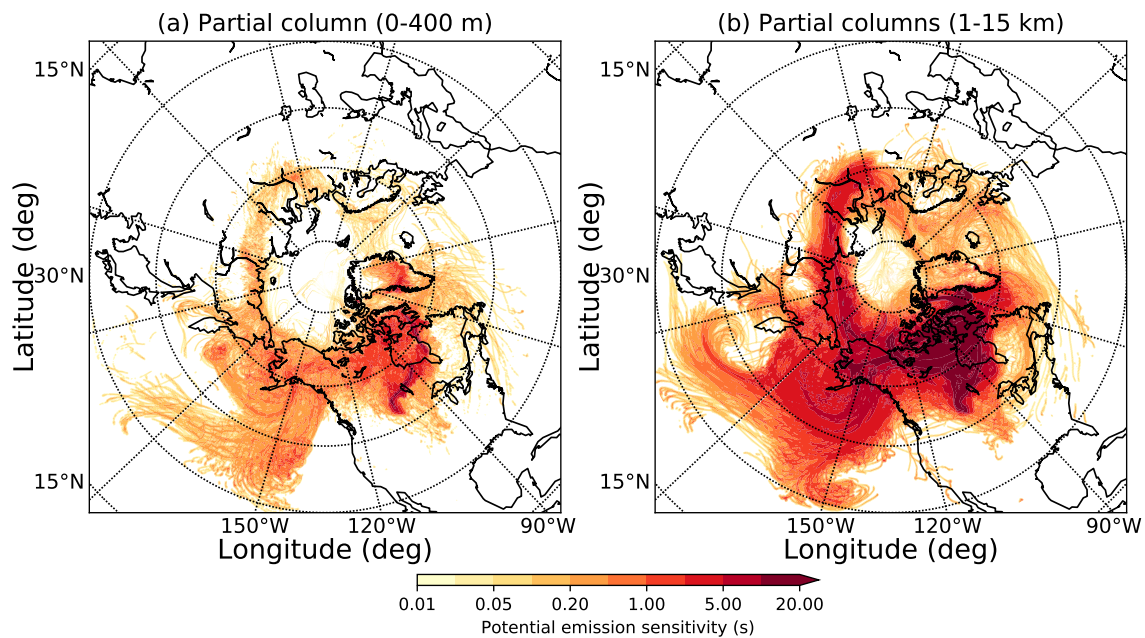
Figure S34. FLEXPART 15-days integrated (a) partial column 0 - 400 m and (b) partial column 1 - 15 km potential emission sensitivity (PES; for measurements on 21 July from 18:30 until 18:40 UTC) as an example of transport from oil field emissions in Alberta (Canada) to the measurement region.

Figure S35. FLEXPART 15-days integrated (a) partial column 1 - 15 km and (b) partial column 0 - 400 m potential emission sensitivity (PES; for measurements on 12 July from 18:40 until 18:50 UTC) as an example of transport from European sources to the measurement region. Note that air mass transport into the Arctic took place mainly above 400 m.
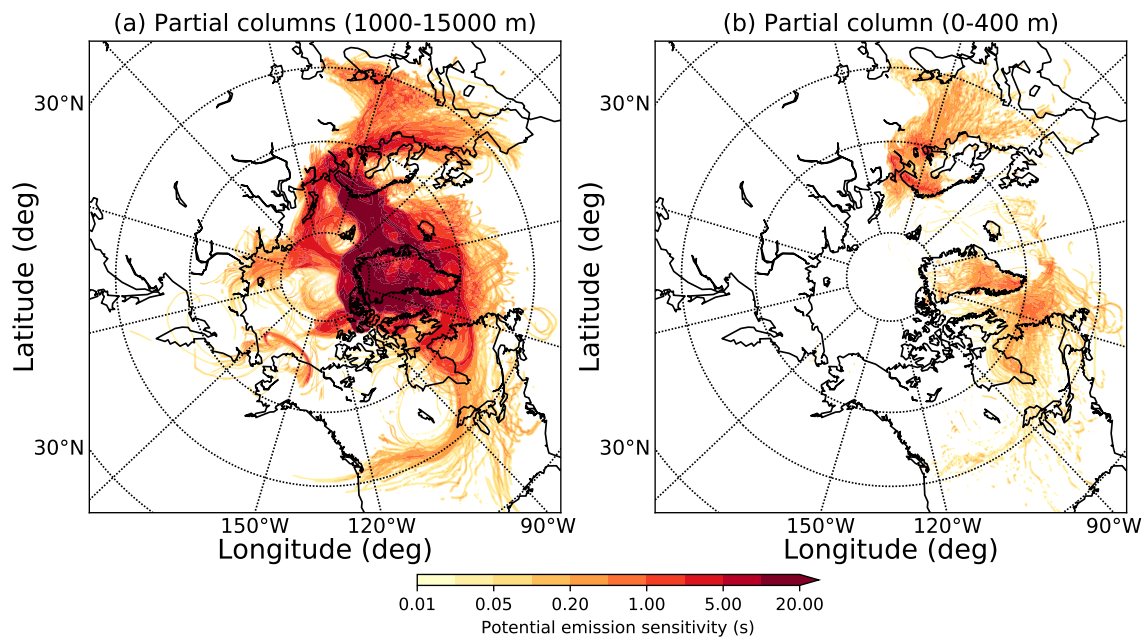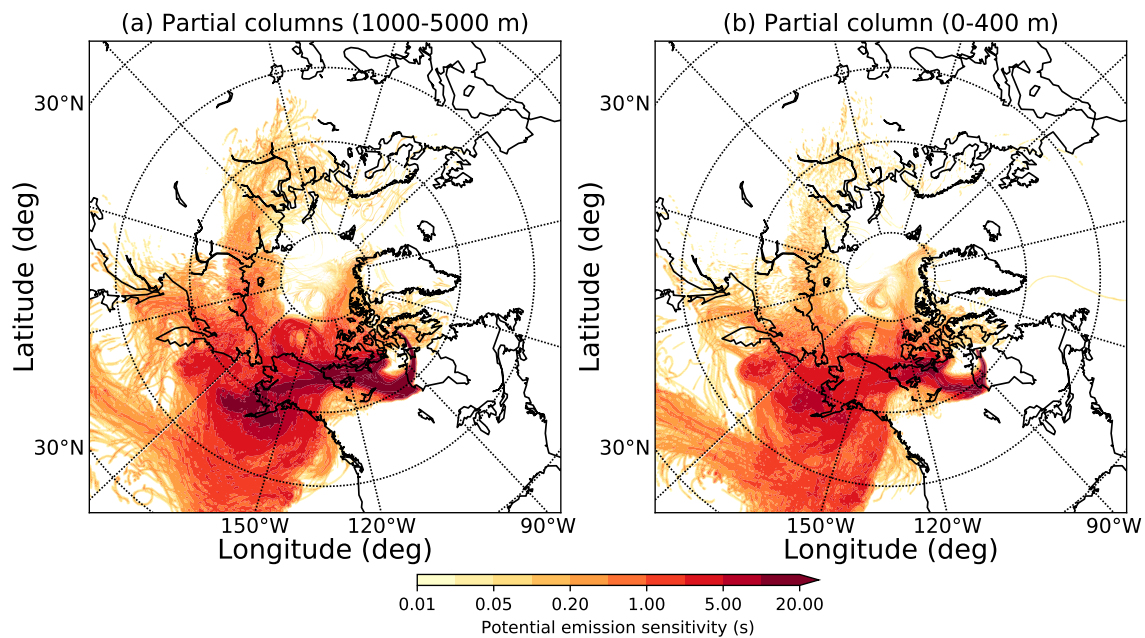
Figure S36. FLEXPART 15-days integrated (a) partial column 1 - 5 km and (b) partial column 0 - 400 m potential emission sensitivity (PES; for measurements on 19 July from 15:30 until 15:40 UTC) as an example of transport of emissions from vegetation fires in northern Canada (compare to Fig. 4a) to the measurement region.

9 Pre-processing of source sector contributions

By comparing PES fractions of different source sectors during the NETCARE 2014 measurements, two types of plumes are obvious: plumes with definite contributions from one source sector separated from other sectors (Figs. S37a-b) and plumes with mixed contributions from different source sectors (mixed plumes; Fig. S37c). However, a combination of both plume types is given in Figs. S37d-f. In such cases, mixed plumes were excluded from the further analysis, in order to provide a distinct source attribution. This had only been done if data statistics were still sufficient after selection. In detail, certain thresholds were set for selection (indicated with black boxes in Figs. S37d-f), differentiating mixed plumes from plumes of distinct source attribution. As a result for the southern air mass period, contributions from vegetation fires are separated from anthropogenic sources (Figs. S37d-e) and contributions from populated areas are separated from vegetation fires and industrial sources (Figs. S37d and f, respectively).
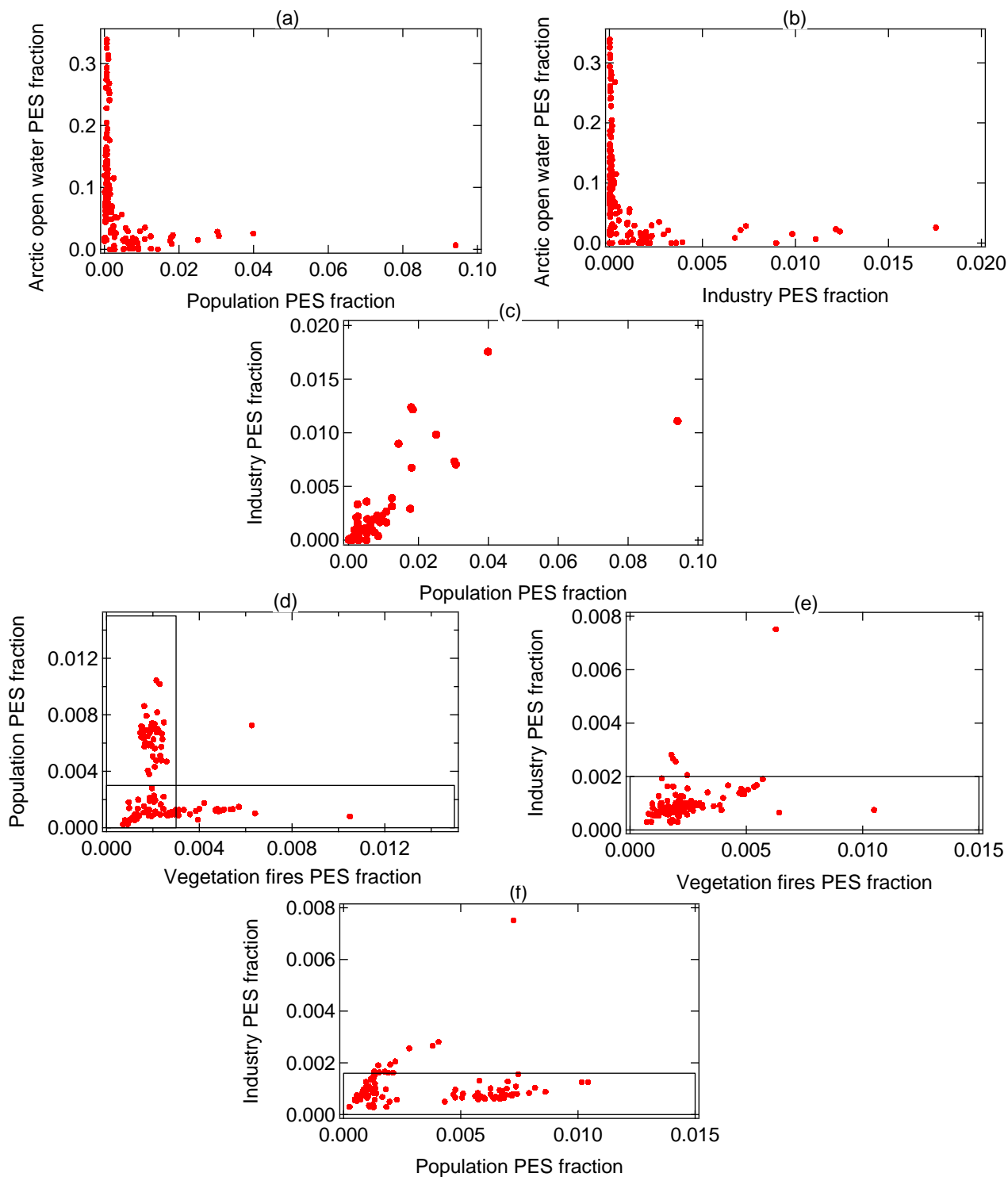
Figure S37. Comparison between different source sectors during the Arctic (a-c) and southern (d-f) air mass periods. Black boxes represent thresholds to differentiate between different sectors.

References

Aero-Laser GmbH: Ultra-Fast Carbon-Monoxide Analyser AL5002-Manual-Version 1.24, Aero-Laser GmbH, 2013.

Andreae, M. O. and Merlet, P.: Emission of trace gases and aerosols from biomass burning, Global Biogeochem. Cy., 15, 955–966, https://doi.org/10.1029/2000GB001382, 2001.

Arndt, D. S., Blunden, J., Willett, K. W., Aaron-Morrison, A. P., Ackerman, S. A., Adamu, J. I., Albanil, A., Alfaro, E. J., Allan, R., Alley, R. B., Alvarez, L., Alves, L. M., Amador, J. A., Andreassen, L. M., Antonov, J., Applequist, S., Arendt, A., Arevalo, J., Arguez, A., Banzon, V., Barichivich, J., Baringer, M. O., Barreira, S., Baxter, S., Bazo, J., Becker, A., Behrenfeld, M. J., Bell, G. D., Benedetti, A., Bernhard, G., Berrisford, P., Berry, D. I., Bettolli, M. L., Bhatt, U. S., Bidegain, M., Bindoff, N., Bissolli, P., Blake, E. S., Blenman, R. C., Bond, N. A., Bosilovich, M., Box, J. E., Boudet, D., Boyer, T., Braathen, G. O., Bromwich, D. H., Brown, L. C., Brown, R., Bulygina, O. N., Burgess, D., Calderon, B., Camargo, S. J., Campbell, J. D., Cappelen, J., Carrasco, G., Carter, B., Chambers, D. P., Chandler, E., Chevallier, F., Christiansen, H. H., Christy, J. R., Chung, D., Ciais, P., Clem, K. R., Coelho, C. A. S., Cogley, J. G., Coldewey-Egbers, M., Colwell, S., Cooper, O. R., Copland, L., Cronin, M. F., Crouch, J., Cunningham, S. A., Davis, S. M., De Jeu, R. A. M., Degenstein, D., Demircan, M., Derksen, C., Destin, D., Diamond, H. J., Dlugokencky, J., Dohan, K., Dolman, A. J., Domingues, C. M., Donat, M. G., Dong, S., Dorigo, W. A., Drozdov, D. S., Duguay, C. R., Dunn, R. J. H., Duran-Quesada, A. M., Dutton, G. S., Ebrahim, A., Elkins, J. W., Epstein, H. E., Espinoza, J. C., Evans, T. E., Famiglietti, J. S., Fateh, S., Fauchereau, N. C., Feely, R. A., Fenimore, C., Fettweis, X., Fioletov, V. E., Flemming, J., Fogarty, C. T., Fogt, R. L., Folland, C. K., Foster, M., Francis, S. D., Franz, B. A., Freeland, H., Frith, S. M., Froidevaux, L., Frost, G. V., Ganter, C., Garzoli, S., Gerland, S., Gitau, W., Gobron, N., Goldenberg, S. B., Goni, G., Gonzalez, I. T., Good, S. A., Goto, A., Griffin, K. S., Grist, J., Grooss, J. U., Guard, C., Gupta, S. K., Hagos, S., Haimberger, L., Hall, B. D., Halpert, M. S., Hamlington, B. D., Hanna, E., Hanssen-Bauer, I., Harris, I., Heidinger, A. K., Heikkila, A., Heim, R. R., Hendricks, S., Hernandez, M., Hidalgo, H. G., Hilburn, K., Ho, S. P., Hobbs, W. R., Hu, Z. Z., Huelsing, H., Hurst, D. F., Inness, A., Ishii, M., Jeffers, B., Jeffries, M. O., Jevrejeva, S., Jin, X. Z., John, V., Johns, W. E., Johnsen, B., Johnson, B., Johnson, G. C., Jones, P. D., Josey, S. A., Joyette, S., Jumaux, G., Kabidi, K., Kaiser, J. W., Kang, K. K., Kanzow, T. O., Kao, H. Y., Kazemi, A., Keller, L. M., Kendon, M., Kennedy, J., Kerr, K., Kheyrollah Pour, H., Kholodov, A. L., Khoshkam, M., Kidd, R., Kieke, D., Kim, H., Kim, S. J., Kimberlain, T. B., Klotzbach, P., Knaff, J. A., Kobayashi, S., Kohler, J., Korshunova, N. N., Koskela, T., Kramarova, N., Kratz, D. P., Kruger, A., Kruk, M. C., Kumar, A., Kwok, R., Lagerloef, G. S. E., Lakkala, K., Lander, M. A., Landsea, C. W., Lankhorst, M., Lantz, K., Lazzara, M. A., Leuliette, E., L'Heureux, M., Lieser, J. L., Lin, I. I., Liu, H., Liu, Y., Locarnini, R., Loeb, N. G., Long, C. S., Lorrey, A. M., Loyola, D., Lui, Y. Y., Lumpkin, R., Luo, J. J., Luojus, K., Lyman, J. M., Macara, G. R., Maddux, B. C., Malkova, G. V., Manney, G., Marcellin-Honore, V., Marchenko, S. S., Marengo, J. A., Marra, J. J., Martinez-Guingla, R., Massom, R. A., Mata, M. M., Mathis, J. T., Mazloff, M., McBride, C., McCarthy, G., McGree, S., McLean, N., McVicar, T. R., Mears, C. A., Meier, W., Meinen, C. S., Mekonnen, A., Melzer, T., Menendez, M., Mengistu Tsidu, G., Meredith, M. P., Merrifield, M. A., Mitchum, G. T., Monteiro, P., Montzka, S. A., Morice, C., Mote, T., Mudryk, L., Muhle, J., Mullan, A. B., Muller, R., Nash, E. R., Naveira Garabato, A. C., Nerem, R. S., Newman, L., Newman, P. A., Nicolaus, M., Nieto, J. J., Noetzli, J., O'Neel, S., Oberman, N. G., Ogallo, L. A., Oki, T., Oludhe, C. S., Osborn, T. J., Overland, J., Oyunjargal, L., Pabon, D., Parinussa, R. M., Park, E. H., Parker, D., Parsons, R., Pasch, R. J., Pascual-Ramirez, R., Pelto, M. S., Peng, L., Perovich, D., Persson, P. O. G., Peterson, T. C., Petropavlovskikh, I., Peuch, V. H., Pezza, A. B., Phillips, D., Photiadou, C., Pinty, B., Pitts, M. C., Porter, A. O., Proshutinsky, A., Quegan, S., Quintana, J., Rahimzadeh, F., Rajeevan, M., Ramos, A., Raynor, D., Razuvaev, V. N., Reagan, J., Reid, P., Reimer, C., Remy, S., Rennie, J., Renwick, J. A., Revadekar, J. V., Richter-Menge, J. A., Robinson, D. A., Rodell, M., Romanovsky, V. E., Ronchail, J., Rosenlof, K. H., Roth, C., Sabine, C. L., Sallee, J. B., Sanchez-Lugo, A., Santee, M. L., Sawaengphokhai, P., Sayouri, A., Scambos, T. A., Schemm, J., Schmid, C., Schmidtko, S., Schreck, C. J., Send, U., Sensoy, S., Setzer, A., Sharp, M., Shaw, A., Shi, L., Shiklomanov, N. I., Shu, S., Shupe, M. D., Siegel, D. A., Sima, F., Simmons, A. J., Smeed, D. A., Smeets, C., Smith, C., Smith, S. L., Smith, T. M., Spence, J. M., Srivastava, A. K., Stackhouse Jr, P. W., Stammerjohn, S., Steinbrecht, W., Stella, J. L., Stephenson, K., Stephenson, T. S., Strahan, S., Strel: Bulletin of the American Meteorological Society, chap. State of the Climate in 2014, State of the Climate, https://repository.library.noaa.gov/view/noaa/17469, journal Article, 2015.

Bahreini, R., Dunlea, E. J., Matthew, B. M., Simons, C., Docherty, K. S., DeCarlo, P. F., Jimenez, J. L., Brock, C. A., and Middlebrook, A. M.: Design and Operation of a Pressure-Controlled Inlet for Airborne Sampling with an Aerodynamic Aerosol Lens, Aerosol Sci. Technol., 42, 465–471, https://doi.org/10.1080/02786820802178514, 2008.

Bozem, H., Hoor, P., Kunkel, D., Köllner, F., Schneider, J., Herber, A., Schulz, H., Leaitch, W. R., Aliabadi, A. A., Willis, M. D., Burkart, J., and Abbatt, J. P. D.: Characterization of Transport Regimes and the Polar Dome during Arctic Spring and Summer using in-situ Aircraft Measurements, Atmos. Chem. Phys. Discuss., 2019, 1–36, https://doi.org/10.5194/acp-2019-70, 2019.

Brands, M., Kamphus, M., Böttger, T., Schneider, J., Drewnick, F., Roth, A., Curtius, J., Voigt, C., Borbon, A., Beekmann, M., Bourdon, A., Perrin, T., and Borrmann, S.: Characterization of a Newly Developed Aircraft-Based Laser Ablation Aerosol Mass Spectrometer (ALABAMA) and First Field Deployment in Urban Pollution Plumes over Paris During MEGAPOLI 2009, Aerosol Sci. Technol., 45, 46–64, https://doi.org/10.1080/02786826.2010.517813, 2011.

Cai, Y., Montague, D. C., Mooiweer-Bryan, W., and Deshler, T.: Performance characteristics of the ultra high sensitivity aerosol spectrometer for particles between 55 and 800 nm: Laboratory and field studies, J. Aerosol Sci., 39, 759 – 769, https://doi.org/10.1016/j.jaerosci.2008.04.007, 2008.

Cavalieri, D. J., Parkinson, C. L., Gloersen, P., and Zwally, H. J.: Sea Ice Concentrations from Nimbus-7 SMMR and DMSP SSM/I-SSMIS Passive Microwave Data, Version 1, NSIDC-0051, Boulder, Colorado USA. NASA National Snow and Ice Data Center Distributed Active Archive Center, https://doi.org/https://doi.org/10.5067/8GQ8LZQVL0VL, last access: 08.06.2018, 1996, updated yearly.

Clemen, H.-C., Schneider, J., Klimach, T., Helleis, F., Köllner, F., Hünig, A., Rubach, F., Mertes, S., Wex, H., Stratmann, F., Welti, A., Kohl, R., Frank, F., and Borrmann, S.: Optimizing the detection, ablation, and ion extraction efficiency of a single-particle laser ablation mass spectrometer for application in environments with low aerosol particle concentrations, Atmospheric Measurement Techniques, 13, 5923–5953, https://doi.org/10.5194/amt-13-5923-2020, https://amt.copernicus.org/articles/13/5923/2020/, 2020.

Corbin, J., Rehbein, P., Evans, G., and Abbatt, J.: Combustion particles as ice nuclei in an urban environment: Evidence from single-particle mass spectrometry., Atmos. Environ., 51, 286–292, https://doi.org/10.1016/j.atmosenv.2012.01.007, 2012.

Dahlkötter, F., Gysel, M., Sauer, D., Minikin, A., Baumann, R., Seifert, P., Ansmann, A., Fromm, M., Voigt, C., and Weinzierl, B.: The Pagami Creek smoke plume after long-range transport to the upper troposphere over Europe - aerosol properties and black carbon mixing state, Atmos. Chem. Phys., 14, 6111–6137, https://doi.org/10.5194/acp-14-6111-2014, 2014.

DeCarlo, P. F., Kimmel, J. R., Trimborn, A., Northway, M. J., Jayne, J. T., Aiken, A. C., Gonin, M., Fuhrer, K., Horvath, T., Docherty, K. S., Worsnop, D. R., and Jimenez, J. L.: Field-Deployable, High-Resolution, Time-of-Flight Aerosol Mass Spectrometer, Anal. Chem., 78, 8281–8289, https://doi.org/10.1021/ac061249n, 2006.

Elvidge, C. D., Zhizhin, M., Hsu, F.-C., and Baugh, K. E.: VIIRS Nightfire: Satellite Pyrometry at Night, Remote Sensing, 5, 4423–4449, https://doi.org/10.3390/rs5094423, 2013.

Elvidge, C. D., Zhizhin, M., Baugh, K., Hsu, F.-C., and Ghosh, T.: Methods for Global Survey of Natural Gas Flaring from Visible Infrared Imaging Radiometer Suite Data, Energies, 9, https://doi.org/10.3390/en9010014, 2016.

Fuelberg, H. E., Harrigan, D. L., and Sessions, W.: A meteorological overview of the ARCTAS 2008 mission, Atmos. Chem. Phys., 10, 817–842, https://doi.org/10.5194/acp-10-817-2010, 2010.

Gao, R. S., Schwarz, J. P., Kelly, K. K., Fahey, D. W., Watts, L. A., Thompson, T. L., Spackman, J. R., Slowik, J. G., Cross, E. S., Han, J.-H., Davidovits, P., Onasch, T. B., and Worsnop, D. R.: A Novel Method for Estimating Light-Scattering Properties of Soot Aerosols Using a Modified Single-Particle Soot Photometer, Aerosol Sci. Technol., 41, 125–135, https://doi.org/10.1080/02786820601118398, 2007.

Giglio, L., Randerson, J. T., and van der Werf, G. R.: Analysis of daily, monthly, and annual burned area using the fourth-generation global fire emissions database (GFED4), J. Geophys. Res.-Biogeo., 118, 317–328, https://doi.org/10.1002/jgrg.20042, 2013.

Guasco, T. L., Cuadra-Rodriguez, L. A., Pedler, B. E., Ault, A. P., Collins, D. B., Zhao, D., Kim, M. J., Ruppel, M. J., Wilson, S. C., Pomeroy, R. S., Grassian, V. H., Azam, F., Bertram, T. H., and Prather, K. A.: Transition Metal Associations with Primary Biological Particles in Sea Spray Aerosol Generated in a Wave Channel, Environ. Sci. Technol., 48, 1324–1333, https://doi.org/10.1021/es403203d, 2014.

Kalnay, E., Kanamitsu, M., Kistler, R., Collins, W., Deaven, D., Gandin, L., Iredell, M., Saha, S., White, G., Woollen, J., Zhu, Y., Chelliah, M., Ebisuzaki, W., Higgins, W., Janowiak, J., Mo, K. C., Ropelewski, C., Wang, J., Leetmaa, A., Reynolds, R., Jenne, R., and Joseph, D.: The NCEP/NCAR 40-Year Reanalysis Project, B. Am. Meteorol. Soc., 77, 437–472, https://doi.org/10.1175/1520-0477(1996)077<0437:TNYRP>2.0.CO;2, 1996.

Köllner, F., Schneider, J., Willis, M. D., Klimach, T., Helleis, F., Bozem, H., Kunkel, D., Hoor, P., Burkart, J., Leaitch, W. R., Aliabadi, A. A., Abbatt, J. P. D., Herber, A. B., and Borrmann, S.: Particulate trimethylamine in the summertime Canadian high Arctic lower troposphere, Atmos. Chem. Phys., 17, 13 747–13 766, https://doi.org/10.5194/acp-17-13747-2017, 2017.

Kondo, Y., Matsui, H., Moteki, N., Sahu, L., Takegawa, N., Kajino, M., Zhao, Y., Cubison, M. J., Jimenez, J. L., Vay, S., Diskin, G. S., Anderson, B., Wisthaler, A., Mikoviny, T., Fuelberg, H. E., Blake, D. R., Huey, G., Weinheimer, A. J., Knapp, D. J., and Brune, W. H.: Emissions of black carbon, organic, and inorganic aerosols from biomass burning in North America and Asia in 2008, J. Geophys. Res.-Atmos., 116, https://doi.org/10.1029/2010JD015152, 2011.

Laborde, M., Mertes, P., Zieger, P., Dommen, J., Baltensperger, U., and Gysel, M.: Sensitivity of the Single Particle Soot Photometer to different black carbon types, Atmos. Meas. Tech., 5, 1031–1043, https://doi.org/10.5194/amt-5-1031-2012, 2012.

Lavoué, D., Liousse, C., Cachier, H., Stocks, B. J., and Goldammer, J. G.: Modeling of carbonaceous particles emitted by boreal and temperate wildfires at northern latitudes, J. Geophys. Res.-Atmos, 105, 26 871–26 890, https://doi.org/10.1029/2000JD900180, 2000.

Leaitch, W. R., Korolev, A., Aliabadi, A. A., Burkart, J., Willis, M. D., Abbatt, J. P. D., Bozem, H., Hoor, P., Köllner, F., Schneider, J., Herber, A., Konrad, C., and Brauner, R.: Effects of 20–100 nm particles on liquid clouds in the clean summertime Arctic, Atmos. Chem. Phys., 16, 11 107–11 124, https://doi.org/10.5194/acp-16-11107-2016, 2016.

Lee, S.-H., Murphy, D. M., Thomson, D. S., and Middlebrook, A. M.: Nitrate and oxidized organic ions in single particle mass spectra during the 1999 Atlanta Supersite Project, J. Geophys. Res.-Atmos, 108, https://doi.org/10.1029/2001JD001455, 8471, 2003.

Leung, F.-Y. T., Logan, J. A., Park, R., Hyer, E., Kasischke, E., Streets, D., and Yurganov, L.: Impacts of enhanced biomass burning in the boreal forests in 1998 on tropospheric chemistry and the sensitivity of model results to the injection height of emissions, J. Geophys. Res.-Atmos, 112, https://doi.org/10.1029/2006JD008132, 2007.

Liu, Y., Hu, C., Zhan, W., Sun, C., Murch, B., and Ma, L.: Identifying industrial heat sources using time-series of the VIIRS Nightfire product with an object-oriented approach, Remote Sens. Environ., 204, 347 – 365, https://doi.org/10.1016/j.rse.2017.10.019, 2018.

MaxMind: https://www.maxmind.com/en/free-world-cities-database, last access: 10.06.2018, 2018.

Moffet, R. C., de Foy, B., Molina, L. T., Molina, M. J., and Prather, K. A.: Measurement of ambient aerosols in northern Mexico City by single particle mass spectrometry, Atmos. Chem. Phys., 8, 4499–4516, https://doi.org/10.5194/acp-8-4499-2008, 2008.

NASA: https://doi.org/10.5067/FIRMS/VIIRS/VNP14IMGT.NRT.001., https://firms.modaps.eosdis.nasa.gov, last access: 29.09.2018, 2018.

NOAA: https://www.ngdc.noaa.gov/eog/viirs/download_viirs_fire.html, last access: 01.10.2018, 2018a.

NOAA: https://data.ngdc.noaa.gov/instruments/remote-sensing/passive/spectrometers-radiometers/imaging/viirs/vnf/v21/flares/, last access: February 2018, 2018b.

Prather, K. A., Bertram, T. H., Grassian, V. H., Deane, G. B., Stokes, M. D., DeMott, P. J., Aluwihare, L. I., Palenik, B. P., Azam, F., Seinfeld, J. H., Moffet, R. C., Molina, M. J., Cappa, C. D., Geiger, F. M., Roberts, G. C., Russell, L. M., Ault, A. P., Baltrusaitis, J., Collins, D. B., Corrigan, C. E., Cuadra-Rodriguez, L. A., Ebben, C. J., Forestieri, S. D., Guasco, T. L., Hersey, S. P., Kim, M. J., Lambert, W. F., Modini, R. L., Mui, W., Pedler, B. E., Ruppel, M. J., Ryder, O. S., Schoepp, N. G., Sullivan, R. C., and Zhao, D.: Bringing the ocean into the laboratory to probe the chemical complexity of sea spray aerosol, P. Natl. Acad. Sci., 110, 7550–7555, https://doi.org/10.1073/pnas.1300262110, 2013.

Pratt, K. A., DeMott, P. J., French, J. R., Wang, Z., Westphal, D. L., Heymsfield, A. J., Twohy, C. H., Prenni, A. J., and Prather, K. A.: In situ detection of biological particles in cloud ice-crystals, Nature Geoscience, 2, 398–401, https://doi.org/10.1038/ngeo521, 2009.

Roth, A., Schneider, J., Klimach, T., Mertes, S., van Pinxteren, D., Herrmann, H., and Borrmann, S.: Aerosol properties, source identification, and cloud processing in orographic clouds measured by single particle mass spectrometry on a central European mountain site during HCCT-2010, Atmos. Chem. Phys., 16, 505–524, https://doi.org/10.5194/acp-16-505-2016, 2016.

Scharffe, D., Slemr, F., Brenninkmeijer, C. A. M., and Zahn, A.: Carbon monoxide measurements onboard the CARIBIC passenger aircraft using UV resonance fluorescence, Atmos. Meas. Tech., 5, 1753–1760, https://doi.org/10.5194/amt-5-1753-2012, 2012.

Schmidt, S.: Analyse der chemischen Zusammensetzung von Eis- und Wolkenresiduen mittels Einzelpartikel-Massenspektrometrie und Charakterisierung von Aerosolpartikeln aus anthropogenen und natürlichen Quellen, Ph.D. thesis, Johannes Gutenberg-Universität Mainz, 2015.

Schmidt, S., Schneider, J., Klimach, T., Mertes, S., Schenk, L. P., Kupiszewski, P., Curtius, J., and Borrmann, S.: Online single particle analysis of ice particle residuals from mountain-top mixed-phase clouds using laboratory derived particle type assignment, Atmos. Chem. Phys., 17, 575–594, https://doi.org/10.5194/acp-17-575-2017, 2017.

Schroeder, W. and Giglio, L.: NASA VIIRS Land Science Investigator Processing System (SIPS) Visible Infrared Imaging Radiometer Suite (VIIRS) 375 m & 750 m Active Fire Products: Product User's Guide Version 1.4, Tech. rep., Department of Geographical Sciences, University of Maryland, 2018.

Schroeder, W., Oliva, P., Giglio, L., and Csiszar, I. A.: The New VIIRS 375m active fire detection data product: Algorithm description and initial assessment, Remote Sens. Environ., 143, 85 – 96, https://doi.org/10.1016/j.rse.2013.12.008, 2014.

Schulz, H., Zanatta, M., Bozem, H., Leaitch, W. R., Herber, A. B., Burkart, J., Willis, M. D., Kunkel, D., Hoor, P. M., Abbatt, J. P. D., and Gerdes, R.: High Arctic aircraft measurements characterising black carbon vertical variability in spring and summer, Atmos. Chem. Phys., 2019, 2361–2384, https://doi.org/10.5194/acp-19-2361-2019, 2019.

Schwarz, J. P., Gao, R. S., Fahey, D. W., Thomson, D. S., Watts, L. A., Wilson, J. C., Reeves, J. M., Darbeheshti, M., Baumgardner, D. G., Kok, G. L., Chung, S. H., Schulz, M., Hendricks, J., Lauer, A., Kärcher, B., Slowik, J. G., Rosenlof, K. H., Thompson, T. L., Langford, A. O., Loewenstein, M., and Aikin, K. C.: Single-particle measurements of midlatitude black carbon and light-scattering aerosols from the boundary layer to the lower stratosphere, J. Geophys. Res.-Atmos., 111, https://doi.org/10.1029/2006JD007076, 2006.

Silva, P. J. and Prather, K. A.: Interpretation of Mass Spectra from Organic Compounds in Aerosol Time-of-Flight Mass Spectrometry, Anal. Chem., 72, 3553–3562, https://doi.org/10.1021/ac9910132, 2000.

Silva, P. J., Liu, D.-Y., Noble, C. A., and Prather, K. A.: Size and Chemical Characterization of Individual Particles Resulting from Biomass Burning of Local Southern California Species, Environ. Sci. Technol., 33, 3068–3076, https://doi.org/10.1021/es980544p, 1999.

Simoneit, B., Schauer, J., Nolte, C., Oros, D., Elias, V., Fraser, M., Rogge, W., and Cass, G.: Levoglucosan, a tracer for cellulose in biomass burning and atmospheric particles, Atmos. Environ., 33, 173–182, https://doi.org/10.1016/S1352-2310(98)00145-9, 1999.

Snyder, J. P.: Map projections used by the U.S. Geological Survey, Tech. rep., Washington, D.C., http://pubs.er.usgs.gov/publication/b1532, report, 1982.

Stohl, A.: Characteristics of atmospheric transport into the Arctic troposphere, J. Geophys. Res.-Atmos., 111, https://doi.org/10.1029/2005JD006888, 2006.

Tjernström, M., Birch, C. E., Brooks, I. M., Shupe, M. D., Persson, P. O. G., Sedlar, J., Mauritsen, T., Leck, C., Paatero, J., Szczodrak, M., and Wheeler, C. R.: Meteorological conditions in the central Arctic summer during the Arctic Summer Cloud Ocean Study (ASCOS), Atmos. Chem. Phys., 12, 6863–6889, https://doi.org/10.5194/acp-12-6863-2012, 2012.

Trimborn, A., Hinz, K.-P., and Spengler, B.: Online analysis of atmospheric particles with a transportable laser mass spectrometer during LACE 98, J. Geophys. Res.-Atmos., 107, https://doi.org/10.1029/2001JD000590, 2002.

Turquety, S., Logan, J. A., Jacob, D. J., Hudman, R. C., Leung, F. Y., Heald, C. L., Yantosca, R. M., Wu, S., Emmons, L. K., Edwards, D. P., and Sachse, G. W.: Inventory of boreal fire emissions for North America in 2004: Importance of peat burning and pyroconvective injection, J. Geophys. Res.-Atmos., 112, https://doi.org/10.1029/2006JD007281, 2007.

Val Martin, M., Kahn, R. A., and Tosca, M. G.: A Global Analysis of Wildfire Smoke Injection Heights Derived from Space-Based Multi-Angle Imaging, Remote Sensing, 10, https://doi.org/10.3390/rs10101609, 2018.

Wandel, M.: CO-Messung in der Arktis im Rahmen der NETCARE-Kampa-gne, Master's thesis, Johannes Gutenberg-Universität Mainz, 2015.

Willis, M. D., Burkart, J., Thomas, J. L., Köllner, F., Schneider, J., Bozem, H., Hoor, P. M., Aliabadi, A. A., Schulz, H., Herber, A. B., Leaitch, W. R., and Abbatt, J. P. D.: Growth of nucleation mode particles in the summertime Arctic: a case study, Atmos. Chem. Phys., 16, 7663–7679, https://doi.org/10.5194/acp-16-7663-2016, 2016.

Willis, M. D., Köllner, F., Burkart, J., Bozem, H., Thomas, J. L., Schneider, J., Aliabadi, A. A., Hoor, P. M., Schulz, H., Herber, A. B., Leaitch, W. R., and Abbatt, J. P. D.: Evidence for marine biogenic influence on summertime Arctic aerosol, Geophys. Res. Lett., 44, 6460–6470, https://doi.org/10.1002/2017GL073359, 2017.

Zauscher, M. D., Wang, Y., Moore, M. J. K., Gaston, C. J., and Prather, K. A.: Air Quality Impact and Physicochemical Aging of Biomass Burning Aerosols during the 2007 San Diego Wildfires, Environ. Sci. Technol., 47, 7633–7643, https://doi.org/10.1021/es4004137, 2013.